TOWARDS ACCURATE SEISMIC IMAGING USING PHASE SHIFT PLUS INTERPOLATION FOR VISCO-ACOUSTIC MEDIA

BY

MOHAMMED YAHIYA NAVEED

A Thesis Presented to the
DEANSHIP OF GRADUATE STUDIES

KING FAHD UNIVERSITY OF PETROLEUM & MINERALS
DHAHRAN, SAUDI ARABIA

In Partial Fulfillment of the
Requirements for the Degree of

MASTER OF SCIENCE
In

ELECTRICAL ENGINEERING

DECEMBER, 2014

KING FAHD UNIVERSITY OF PETROLEUM & MINERALS
DHAHRAN 31261, SAUDI ARABIA

DEANSHIP OF GRADUATE STUDIES

This thesis, written by **MOHAMMED YAHIYA NAVEED** under the direction of his thesis adviser and approved by his thesis committee, has been presented to and accepted by the Dean of Graduate Studies, in partial fulfillment of the requirements for the degree of **MASTER OF SCIENCE IN ELECTRICAL ENGINEERING DEPARTMENT**.

Thesis Committee

Dr. Wail A. Mousa (Adviser)

Dr.Abdullatif A. Al-Shuhail (Member)

azzedine zerguine

Dr.Azzedine M. Zerguine (Member)

Dr.Ali A. Al-Shaikhi
Department Chairman

Dr. Salam A. Zummo
Dean of Graduate Studies

11/1/15

Date

ACKNOWLEDGMENTS

First of all, I would like to thank Allah (S.W.T) for guiding me towards right path and for showering his blessings upon me. I would like to thank KFUPM for giving me this opportunity to complete my master's degree in such a challenging environment. I would like to thank my thesis advisor Dr. Wail A. Mousa for encouraging me to take seismic signal processing as my reseach area and for guiding me throughout the research. It was his enthusiasm and guidance which made me accomplish my thesis objectives. The experience has been interesting and rewarding one.

I would also like to thank my thesis committee members, Dr. Abdullatif Al-Shuhail for his guidance, valuable suggestions and providing me the computational resources that were required for my simulations and for reviewing my work time to time. Also, I would like to thank Dr. Azzedine Zerguine for providing me his support, as well as his efforts in proof reading the drafts. I would specifically like to thank Center for Communication and Information Technology Research (CCITR)- Research Institute (RI) for providing me scholarship during my master's degree. I would also like to thank Dr. Gary F. Margrave from University of Calgary, Canada, for providing me valuable suggestions when it was required. I *would like to thank my parents and family members for their unconditional support throughout the research, and building confidence in me during difficult times. In addition to this, I would like to thank my friends and seismic group in EE department, KFUPM, for helping me with the installations and software related works.*

TABLE OF CONTENTS

LIST OF TABLES

LIST OF FIGURES

THESIS ABSTRACT

NAME:	Mohammed Yahiya Naveed
TITLE OF STUDY:	Towards Accurate Seismic Imaging using Phase Shift plus Interpolation for Visco-acoustic Media
MAJOR FIELD:	Electrical Engineering Department
DATE OF DEGREE:	DECEMBER 2014

Seismic waves get attenuated and dispersed as they propagate in the earth. This attenuation of waves is mostly due to spherical divergence and friction of rock particles. In order to obtain an image of the subsurface with good resolution such factors should be considered. In this research, prestack depth imaging is performed using the Phase Shift plus Interpolation (PSPI) technique after modifying it to accommodate attenuation. The compensation is performed by deriving the wavefield extrapolators in the frequency-wavenumber $(f-k)$ *domain. The extrapolators are first derived to obtain an image without any compensation in the* $(f-k)$ *domain, i.e., acoustic PSPI. Next, the extrapolators are modified to compensate for attenuation losses, (i.e., visco-acoustic PSPI). Both phase velocity and absorption Q-model are used in wavefield extrapolation to obtain seismic images with com-*

pensating operators. Operator compensation requires a trivial cosine transform applied on the non-compensating operators in order to compensate for the effect of absorption and dispersion, thereby, increasing the spatial resolution of the subsurface image obtained. In addition, the assessment of seismic images is addressed in this thesis. The assessment of such important images is mostly done subjectively in practice. Here, a method is developed to evaluate the quality of seismic images objectively by taking into consideration the noise and spatial resolution (the amount of blur). Here we consider non-reference based image quality assessment methods because in most practical cases, a reference image is not available.

CHAPTER 1

INTRODUCTION

1.1 Introduction

Natural resources such as oil, gas and coal are extremely important in our day-to-day life. Such resources are hidden in deep land or marine sub-surface structures. Moreover, the use of natural resources like oil and gas is increasing day-by-day and the resources are getting dried up. So not just exploration but accurate exploration is needed in order to find oil and gas reservoirs. The oil exploration process, in particular, finds possible drilling locations, where the actual drilling of an oil well is used to test the geological hypothesis of oil and gas [1, 2]. In order to produce oil we need to first determine the sub-surface i.e. obtain a clear and accurate image of the sub-surface. This can be performed by the method known as reflection seismology . Most of the geophysical technique relies on the generation of artificial seismic waves and the recording of their reflections from different geological layers. However such acquired seismic data does not reveal an accurate image of the sub-surface unless we use an appropriate seismic data processing techniques.

The captured seismic data contain reflections from different earth layers. By analyzing such layers, geologists, after obtaining the final image of the sub-surface, can predict the presence of hydrocarbons. Due to the complex geological conditions, different kinds of reflections are generated. The acquired data has low resolution due to the presence of noise, which in turn make the processing of seismic data more difficult. Therefore, acquiring the high resolution image (data) of the earth sub-surface is the main goal of the field of seismic data processing, such that we can obtain the accurate description of the concerned sub-surface.

The eventual objective of seismic exploration is to identify the hydrocarbons that are buried deep down under below the earths sub-surface through imaging such that there is better productivity with minimum effort [3]. Among the various important and necessary seismic data processing steps is the so called Seismic Imaging. It determines the structure of the interior of the earth from the data obtained at the surface. Due to wave propagation within the sub-surface layers, the data is geometrically affected. There exists many seismic imaging techniques that has been proposed in the literature. Most of the have been used in at an industrial scale [4, 5, 6, 7, 8, 9]. The majority of them rely on the assumption that the sub-surface structures model is acoustic, by which the amplitudes of the propagating waves does not get attenuated with time and depth.

However, the seismic waves, in reality, do get attenuated due to spherical divergence and friction of the rock particles in the form of heat [10, 11]. This consequently causes seismic images to be inaccurate and smoothed in many cases. Many attempts have been performed to compensate for energy losses (amplitude attenuation) at various seismic data processing stages. At the same time, there exists a few attempts to consider the losses by assuming a more realistic model of the sub-surface such as the visco-acoustic model, where the so-called quality factor (Q) [12, 11] is taken into consideration, while performing seismic imaging.

1.2 Thesis Contribution

Phase Shift plus Interpolation (PSPI) is known for its accuracy of determining the sub-surface structures, even under complex geological locations and, hence, has attracted the attention of many seismic explorers during the last two decades [6]. In this thesis, the PSPI will be advanced to include the visco-acoustic medium. To develop the proposed advancement of PSPI to the case of visco-acoustic medium, bench mark synthetic data sets provided by Society of Exploration Geophysicists/European Association of Geo-scientists and Engineers (SEG/EAGE) [13] and Marmousi data set [14, 15] are going to be used, respectively, for poststack and prestack imaging. Better quality seismic images can be obtained when assuming the visco-acoustic model, as will be seen later in this thesis, particularly, when zooming into difficult geological structures.

Apart from imaging, there is the assessment of the quality of seismic imaging techniques. The common practice is to assess the quality of such important images on subjective basis, where a human factor determines whether the imaging technique has performed better than another one on the same seismic data set. This matter have been addressed in the field of image processing [16, 17]. Most of the assessment techniques rely on the existence of a reference image, and the assessment methods are commonly known as reference-based quality assessment [16, 17, 18]. In the case of seismic images, unlike digital images, there exists no reference. Recently, there exist non-reference quality assessment methods. They basically vary from a technique to another in terms of computational complexity as well as accuracy. A recent efficient and accurate non-reference based technique has been proposed by [19]. This techniques simply relys on 1) The spatial entropy and 2) The spectral entropy. Also, there exist other techniques which compute the quality metric based on curvelet features [20]. In this thesis, an attempt is made to analyze the results of applying such methods to assess the quality of seismic migrated images. Many comparisons will be shown between the assessment of seismic images for poststack images.

1.3 Thesis Organization

The thesis is structured as follows. Chapter 2 provides the introduction and the background of seismic imaging. The various techniques available from the literature are discussed and the use of a specific technique called Phase Shift plus Interpolation (PSPI) on poststack and prestack seismic data in acoustic medium is shown. In chapter 3, PSPI is applied to perform prestack imaging for a visco-acoustic medium and later with compensation for absorption. Later on, in chapter 4, an attempt is made to assess the quality of a seismic image based on a recent general purpose non-reference quality assessment techniques. Finally, conclusions and future work are given in chapter 5.

CHAPTER 2

SEISMIC IMAGING

2.1 Introduction

The word migration has arrived in seismic imaging because the oil migrates up dip due to its lesser density when compared to water [3]. Migration is quite similar or can be compared to photographic imaging. In photographic imaging, the image is acquired by capturing the reflected source of light from the object by the lens. Here, we have two things to notice: (a) the light travels in the straight line and (b) it travels with a constant speed, and when the light is reflected from the source, it is captured on the film or any digital device. However, in case of seismic imaging, light is replace by sound as the source, further the speed of sound cannot be assumed to be constant and it cannot be assumed to be traveling in a straight line. Moreover, the most important parameter in photographic imaging is the lens and in seismic imaging the lens is equivalent to the earth model. In seismic imaging, we must somehow try to estimate the earth model, which acts as a lens for imaging. The simplest form of earth model is the three dimensional model, which consists of velocity fields that describe the sub-surface speed of compressional sound waves. The complex form of the earth model is the one in which it consists of two additional waves called shear waves. An earth model may also include other properties such as density, elasticity and other rock properties [1, 14, 21].

Seismic imaging or migration is considered to be the data processing technique where we can create the image of the earths sub-surface by processing the seismic data obtained from the seismic reflection survey [8, 11]. It involves geometric representation of received signals that shows how the layer boundary or other structures look like, when they are encountered by seismic waves. Seismic migration [14] was first used in 1920s and till today there have been many variations. A major difference in migration algorithms arises from the way the velocity field is utilized. Migration can be implemented based on different techniques. Migration is likely to be blamed for all sorts of inconsistency in amplitudes and lack of structural details, even though this may be due to the data acquisition or from the earlier processing steps. Therefore, it is very important to know what kind of migration process should be used.

Time migration is a process which collapses diffractions and moves dipping events toward the true position of reflector but leaves the migrated image with a time axis, which must be depth converted at a later stage, especially when the geology is complex. Time migration, assumes that the diffraction shape is hyperbolic and ignores ray bending at velocity boundaries. Time migration, as the name suggests, is applied to seismic data in time coordinate. However, it makes assumption of mild velocity variations and breaks down in complex subsurface structures like below salt structures [13, 22].

Depth migration is a process which assumes that the arbitrary velocity structure of the earth is known and will compute the correct diffraction shape for the velocity model. The velocity model is built through a long and iterative process, hence, making this process more resource-intensive. The advantage of this type of migration is it can be used in areas where there are lateral velocity variations. The data are then migrated according to the diffraction shape and the output is defined with a depth axis. If the velocity model for the depth migration is incorrect then the migration will be incorrect and the error may be difficult to detect if the migration is performed on poststack data [14]. Prestack depth migration will provide an error estimate of the migrated result. Depth migration typically takes 10 times longer to run than time migration and is very sensitive to velocity errors and may require many iterations which further increases run time [8]. Poststack depth migration is often performed for reasons of economy but prestack depth migration is almost always required, since it is almost impossible to define an accurate velocity model using purely poststack processing.

Depth migration may be considered to be an “appraisal or development”

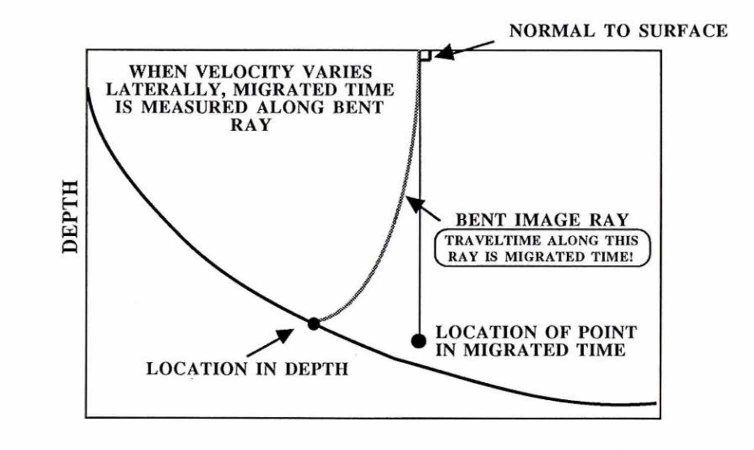

Figure 2.1: Time vs. Depth migration of a point (modified after [1]).

technology whereas time migration may be considered an “exploration” technology. A time-migration can also be easily compared to the input stack section since they have the same vertical axis. Time migration is very fast and is robust to errors in the velocity model. Further, errors in the shallow velocity model do not affect imaging of deeper structures.

Some of the commonly used migration algorithms are Kirchhoff’s depth migration [23], Wave-equation migration [8, 9, 24, 25], Reverse Time Migration (RTM) [26], Stolt migration [9], Gazdag migration [6], and finite difference migration [27].

2.2 Migration Principle

Huygens principle is the basis of migration [3]. This can be explained by the harbor example shown in the Figure 2.2. Assume that a calm breeze is coming from the ocean and an observer is at the beach where a barrier that exists at a certain distance from the beach and has a gap (hole) for water to pass through. Then, one will observe that the gap on the barrier acts as a secondary source and has generated semi-circular wavefronts that are propagating towards the beach. Now, assume that we did not know about the barrier, we lay our receiver cables along the beach and record in time the approaching waves.

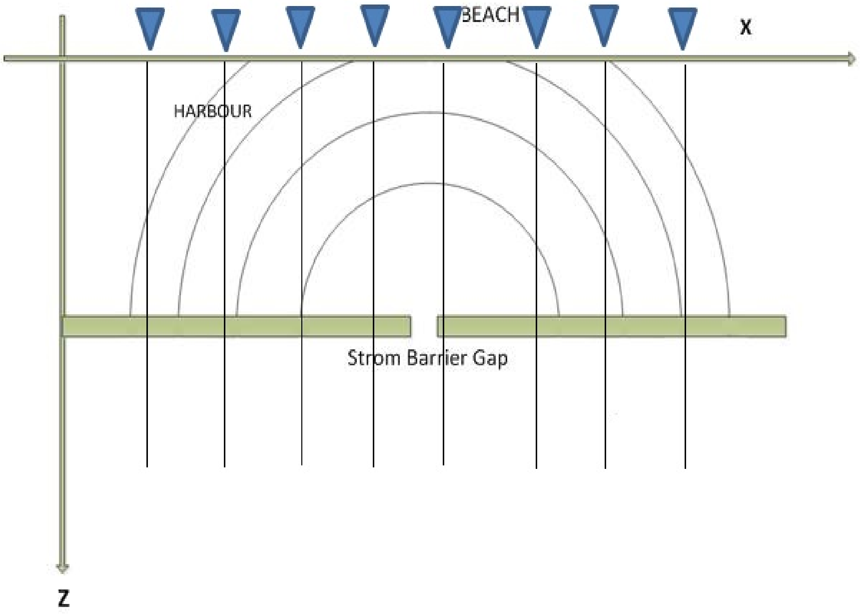

Figure 2.2: Huygens Principle (modified after [1]).

We apply the same principle into reflection seismology by imagining that each point in the geological interface acts as secondary source in response to incident wavefield. This is called the exploding reflector model [14]. Consider a point scattering in a medium as shown in Figure 2.2. The minimum travel time is given by:

$$t_o = \frac{2z}{v}, \tag{2.1}$$

where z the depth of scattering and v is the velocity of wave propagation. Now, we assume that the velocity is constant and the source and receiver are at the same location (zero-offset).The travel time as function of distance x can be given by [28]:

$$t\left(x\right)=\frac{2\sqrt{x^2+z^2}}{v}. \tag{2.2}$$

By squaring and substitution, we obtain:

$$\frac{t(x)^2}{t_0^2}-\frac{4x^2}{v^2t_0^2}=1. \tag{2.3}$$

This shows that the travel time curve for a scattered arrival has hyperbolic form with the apex directly pointing towards the secondary source as shown in Figure 2.3.

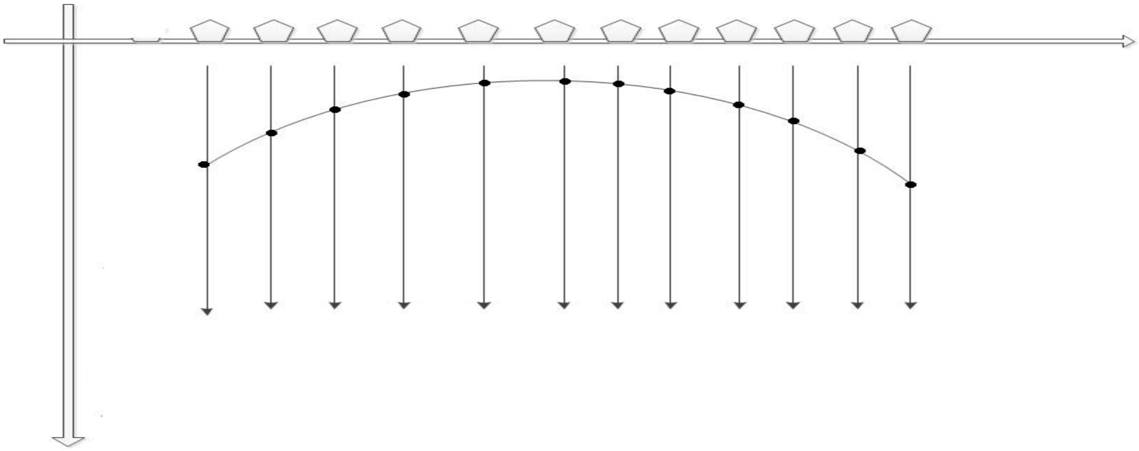

Figure 2.3: Secondary sources from the Huygens principle form hyperbolas [1].

Now if one considers a series of such scatter points in the barriers which generates diffraction hyperbolas. Following Huygens Principle, these hyperbolas sum coherently only at the time of reflection, while their later contribution's cancel out. However, if the reflector vanishes at some point there will be a diffracted arrival from the endpoint which will show up in the zero-offset data. This creates an artifact in the structure, which might be falsely interpreted as a structure. Hence, such sections requires migration in order to remove such artifacts.

Another important aim of migration is to map the apparent dip that is seen on the zero - offset to the true dip. The true dip angle is always grater that the apparent angle [29]. Consider a reflector at an angle of θ the earth as shown in Figure 2.4. The zero offset travel time for a wavefield propagating from distance x down to the reflector and back up again is given by $t = 2r/v$, where r is the wavefield path length and is equal to $xsin\ \theta$. Now, to compare the apparent dip and the true dip we have to travel time to depth via Eq.(2.1). In the un-migrated depth section $z = xsin\ \theta$, from Figure 2.4 one can obtain slope of the event, which is equal to the tangent of the apparent dip angle say β.

Therefore,

$$\tan\beta = \sin\theta. \tag{2.4}$$

This shows that the apparent dip angle is always less than true angle. Hence, we can say that migration moves up dip the reflectors. In addition,

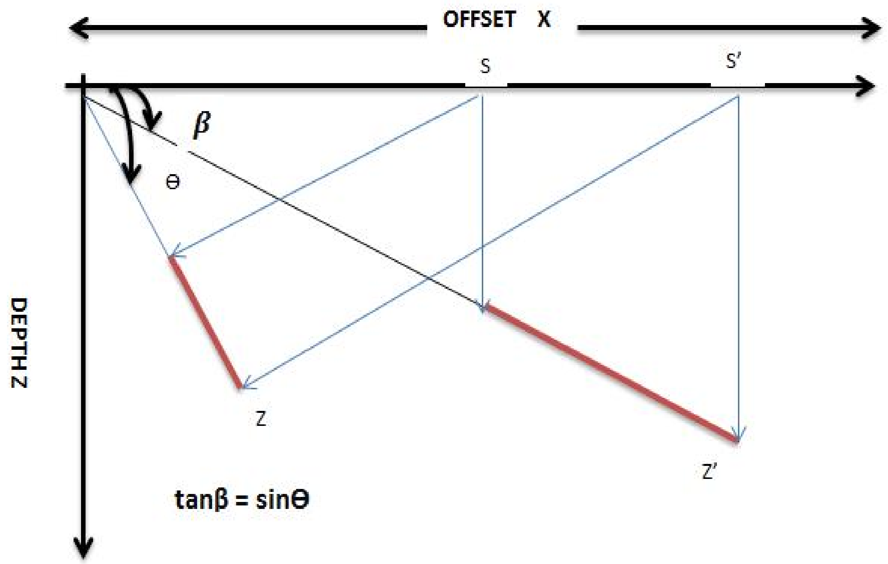

Figure 2.4: The apparent dip with a dip angle β when migrated moves up-dip [1].

the length of the reflector in the geological section is shorter than in the time section. Thus migration also shortens reflector. In short migration focuses energy by collapsing diffraction as well as it correctly shortens, steepens and moves reflectors up-dip. These are the main objectives of seismic imaging [21].

2.3 Seismic Imaging Techniques

There are many migration techniques that are available from the literature. In the early stages of reflection seismology, migration was performed by hand and it was called compass migration [1]. It was used by the interpreters before the computerized versions were available. Later on a new method was introduced by Karcher called Hagedoorn migration which was valid only for constant velocities. It was simply relying on spreading the energy along the semicircles and let waveform reconstruction compose the reflector position, it however provides a valuable insight to the migration process [3]. Kirchhoff migration (summation operator) is considered to be the best but its implementation part varies from a very simple algorithm to one that is complex. This scheme sums the energy along the diffraction. The Fourier transform $(F - K)$ migration was introduced in the later stages which was introduced by Stolt in 1978 [9]. This method is ideal when it comes to constant velocities and will migrate accurately to 90 degrees. Finite difference method was introduced in order to find the data on (n+1)th layer based on nth layer. Methods based on phase shift were developed by Gazdag by using 2-D Fourier transform. This method is appropriate for the depth migration. Phase shift migration [6] is unconditionally stable which applies phase shift in Fourier domain to the extrapolated wave field [4, 6, 30, 31]. The main drawback of this method is that, it requires a constants velocity medium or a medium which is just a function of depth. Phase Shift plus interpolation (PSPI) is one of the forms of phase-shift method which allows lateral velocity changes

[32]. There are few techniques available in the literature that works by switching their domains back and fourth by fixing one dimension in one particular domain. Figure 2.5 shows the flow chart of various imaging techniques.

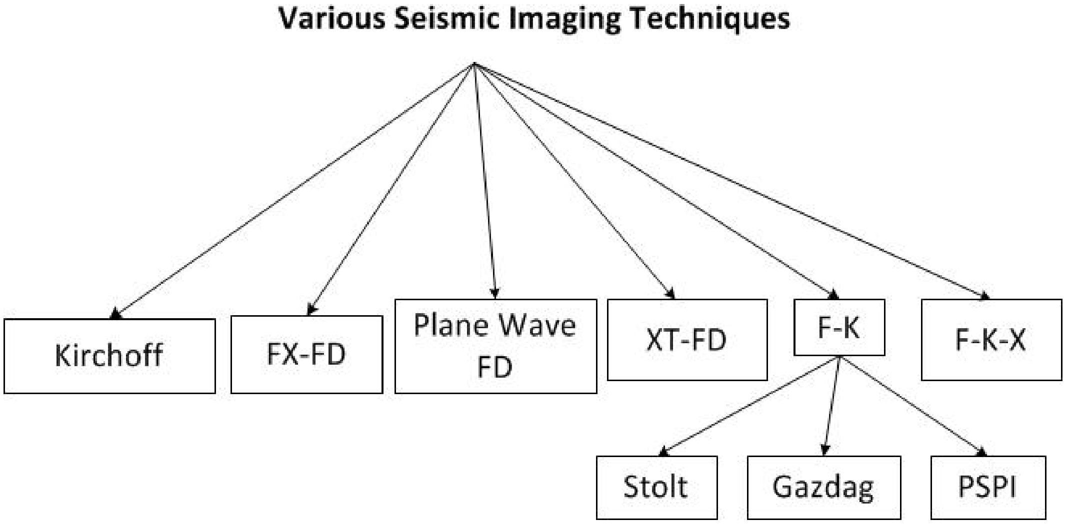

Figure 2.5: Various Seismic Imaging Techniques.

Here, we start with the acoustic data which is given as $p(x, z, t)$ in a medium with a constant material density and velocity v. The following represents the partial differential equation (PDE) that governs the propagation of $p(x, z, t)$ [6]:

$$\frac{\partial^2 p}{\partial x^2} + \frac{\partial^2 p}{\partial z^2} = \frac{1}{v^2} \frac{\partial^2 p}{\partial t^2}, \tag{2.5}$$

where x and z are the horizontal axis and vertical axis respectively and t is the time. The wavefield $p(x, z, t)$ can be expressed in the frequency domain as follows:

$$p\left(x, z, t\right) = \frac{1}{4\pi} \int \int\limits_{-\infty}^{+\infty} P\left(k_x, z, \omega\right) exp\left[-i\left(\omega t - k_x x\right)\right] dk_x d\omega, \tag{2.6}$$

where ω is frequency and k_x is wavenumber.

By substituting Eq.(2.6) in Eq.(2.5) we obtain:

$$\frac{\partial^2 P}{\partial z^2} = \left(\frac{\omega^2}{v^2} - k_x^2\right) P, \tag{2.7}$$

which holds true for all k_x and ω.

If v is constant, the solution to the above equation is given by:

$$P\left(k_x, z = \Delta z, \omega\right) = P\left(k_x, z = 0, \omega\right) e^{ik_z \Delta z}, \tag{2.8}$$

where

$$k_z = \pm\sqrt{\frac{\omega^2}{v^2} - k_x^2}. \tag{2.9}$$

This holds good for $v(z)$ as long as Δ z is small enough.

Eq.(2.8) shows that the wavefield at depth Δz can be computed by phase shifting the data in the Fourier domain. Therefore, by substitution we obtain:

$$P\left(k_x \Delta z, t = 0\right) = \frac{1}{4\pi} \int\limits_{-\infty}^{+\infty} \{ \int\limits_{-\infty}^{\infty} [P\left(k_x, 0, \omega\right) e^{ik_z \Delta z}] e^{ik_x x} dk_x \} d\omega, \tag{2.10}$$

where $e^{ik_z \Delta z}$ in Eq. (2.8) is the phase difference between wavefield at depth Δz, and the surface. The inner integration in Eq.(2.10) corresponds to the inverse Fourier transform over x. The outer integral over ω corresponds to get the migrated depth section $P\left(k_x, \Delta z, t = 0\right)$, which is a single line in (x, z) section. Thus, the depth migrated section can be obtained by repeating this until the desired depth.

2.3.1 Phase Shift plus Interpolation (PSPI) Technique

In case of complex geological structures, where lateral velocities have considerable variations, the phase shift method of migration does not work well. Hence, a new method is introduced to incorporate the lateral velocity variations, called Phase Shift plus Interpolation (PSPI). In PSPI, we use a number of reference velocities to extrapolate the wavefield to next depth. The accuracy of the obtained result depends upon the number of reference velocities used at each depth [33, 34]. The basic idea of PSPI, is to select several reference velocities at each depth to account for the lateral velocity variations in each extrapolation step and obtain multi-reference wavefield in the frequency-wavenumber domain. Based on the relationship between local velocities and the reference velocities, we obtain a final image by interpolating the reference wavefield.

The important features of PSPI are:

- This method allows lateral velocity changes.
- This method computes a number of sub-layers at different velocities for the next depth level.
- Each new layer is inverse Fourier transformed into (ω, x) domain sub layer.
- The output layer is interpolated from the different velocity sub-layers using the appropriate lateral velocity.
- The new layer is transformed back to the (ω, k_x) domain for the next down-

ward step.

The PSPI method is described more clearly by Gazdag [6].

2.3.2 PSPI Algorithm

PSPI assumes that the wavefield at point x_k is equivalent to reference wavefield as long as the velocity in this point $v(k_x)$equals to reference velocity v_i.

The implementation of PSPI involves three steps:

- Initial phase shift is applied to the wavefield.
- Phase shift is applied to set of reference wavefield using reference velocities.
- After we obtain these reference wavefield, we approximate $P\left(x, z, w\right)$ by linearly interpolating over reference wave fields if $v(k_x)$ is close to v_i.

The flow chart for the PSPI is shown in Figure 2.6 To maintain a high accuracy for small dip, laterally varying time-shift is applied in space frequency domain.

$$P\left(k_x, z, \omega\right) = P\left(x, z, \omega\right) e^{i \frac{\omega}{v(x)} \Delta z}. \tag{2.11}$$

This means that this extra time shift will be compensated later in $(k_x{-}\omega)$ domain, i.e., the phase shift term now changes to $e^{\left(ik_z \Delta z - i \frac{\omega}{v(x)} \Delta z\right)}$ instead of $e^{ik_z \Delta z}$ when extrapolating to the next depth.

Two conditions degrade the performance of migration algorithm:

- Insufficient sampling of the data along the shot axis.
- Lateral velocity variations.

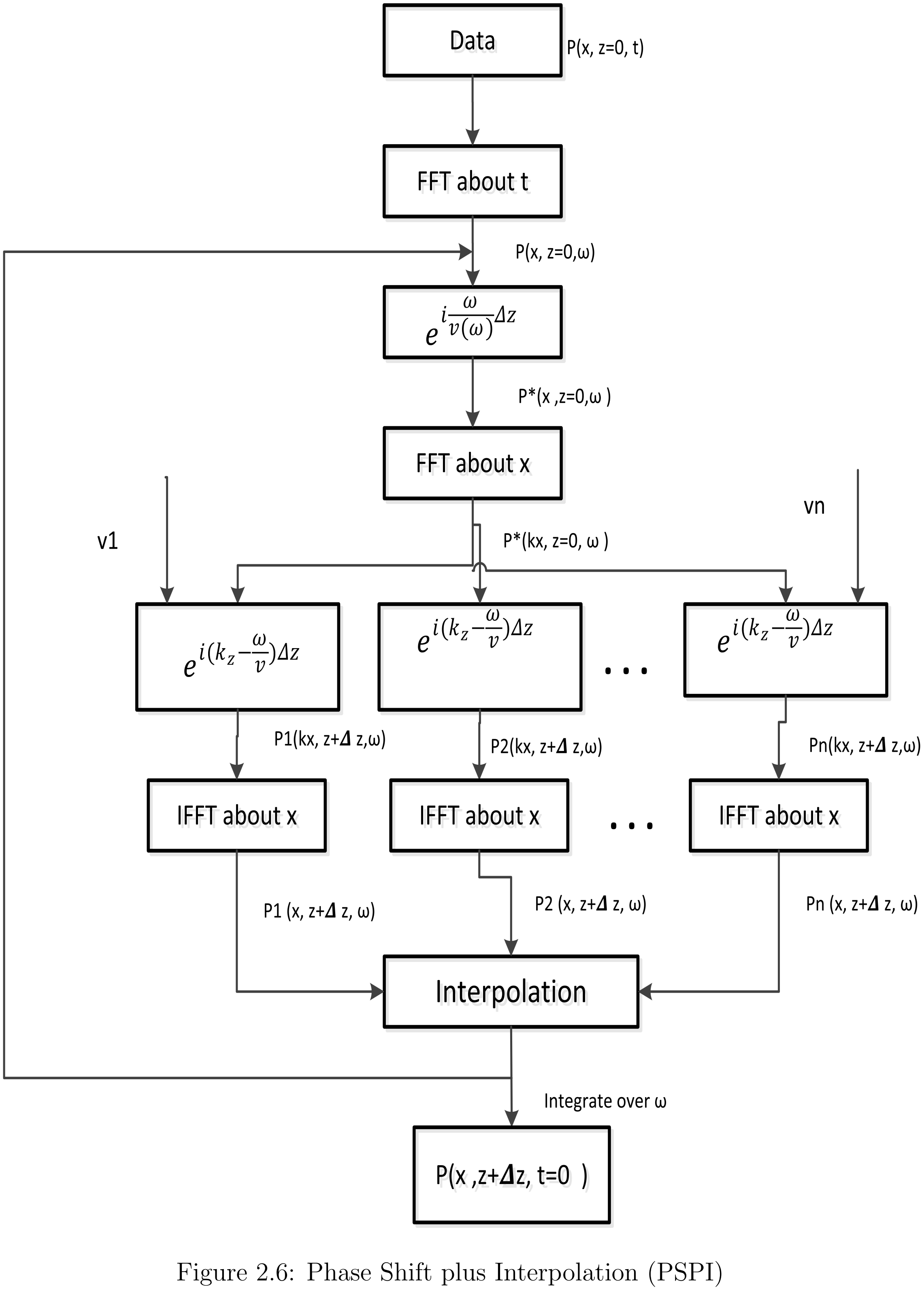

Figure 2.6: Phase Shift plus Interpolation (PSPI)

The Computational Complexity for acoustic PSPI

The computational cost for imaging using PSPI using N_{FFT} FFT points and n_{ref} velocities at each depth slice is given by [6, 35].

For complex multiplications,

$$PSPI - COST_X = 2N_{FFT} \times n_{ref} + (n_{ref} + 2) \times \frac{N_{FFT}}{2}\log_2 N_{FFT}, \tag{2.12}$$

For complex additions,

$$PSPI - COST_+ = (n_{ref} + 2) \times N_{FFT}\log_2 N_{FFT}. \tag{2.13}$$

In both cases, each complex multiplication requires six flops whereas, each complex addition requires two flops as given in [36].

Selection of Reference Velocities

Selection of reference velocities is one of the important criteria in implementing PSPI technique. For efficient computation of depth imaging, there should be a minimum number of reference velocities. Also, for the accurate computation of the wavefield extrapolation the reference velocities should be close to the velocity model [33, 34, 37]. There are many methods that are available for selection of reference velocities like geometric progression method [37], statistical method [34], peak search method [34], etc. Here, we are going to discuss the two basic methods they are:

Geometric Progression Method

This method was introduced by Gazdag and Sguazzero [6]. In this method, the ratio of maximum and minimum velocity is found at some depth (let's say R). A factor called ρ the common ratio for which the consecutive reference velocities form a geometric progression is found. The number of reference velocities m is determined by the smallest integer as follows:

$$\rho^{m-1} \geq R. \tag{2.14}$$

Therefore, we obtain:

$$m = \begin{cases} \frac{\ln \mathrm{R}}{\ln \rho} + 1, if \frac{\ln \mathrm{R}}{\ln \rho} \text{is an integer} \\ \left\lfloor \frac{\ln \mathrm{R}}{\ln \rho} + 1 \right\rfloor + 1, if \left\lfloor \frac{\ln \mathrm{R}}{\ln \rho} + 1 \right\rfloor \text{is not an integer,} \end{cases} \tag{2.15}$$

where $\lfloor . \rfloor$ denotes the integer part of the real number. Then the consecutive reference velocities are chosen as $v_1, v_2, v_3, \ldots v_{m-1} v_m, \text{where} v_1 = v_{\min}$ and $v_1, v_2, v_3, \ldots v_{m-1} v_m, \text{where} v_1 = v_{\min}$.

Based on this we have,

$$v_{\max} \leq v_m < \rho v_{\max}. \tag{2.16}$$

Statistical Method

This method was introduced by Bagaini [37]. Here, we take the minimum and maximum velocities from the velocity model and denote them as $v_{\max}$ and $v_{\min}$, respectively. We divide the velocity range $[v_{\max}, v_{\min}]$ into L subintervals $[c_0 c_1), [c_1, c_2) \ldots [c_{L-2}, c_{L-1}), [c_{L-1}, c_L]$ based on:

$$c_i = v_{\min} + \frac{i\left(v_{\max} - v_{\min}\right)}{L}. \tag{2.17}$$

Suppose in the velocity model we have n_x lateral velocities $v(x_l, z)$, $(l = 1, 2, \ldots n_x)$, at some depth. These velocities will fall into one of the above L subintervals. Let n_i denote the number of velocities that fall into this interval $[\mathrm{c_0 c_1}), [\mathrm{c_1, c_2}) \ldots [\mathrm{c_{L-2}, c_{L-1}})$ and $\mathrm{n_{L-1}}$ is the number of reference velocities falling into the interval $[\mathrm{c_{L-1}, c_L}]$.

Let P_i denote probability density at each bin and the sum of probability is equal to 1. $\mathrm{P_i} = \frac{\mathrm{n_i}}{\mathrm{n_x}}, \mathrm{i} = 0, 1, 2, \ldots, \mathrm{L} - 1.$. Note that $0 \leq \mathrm{P_i} \leq 1$ and $\sum\limits_{\mathrm{i}=0}^{\mathrm{L}-1} \mathrm{P_i} = 1$. Then we construct a number:

$$\mathrm{B} = \exp\left[\sum_{\mathrm{P_i} \neq 0} \ln \mathrm{P_i}^{-\mathrm{Pi}}\right] = \prod_{\mathrm{P_i} \neq 0} \mathrm{P_i}^{-\mathrm{P_i}} \tag{2.18}$$

.

Using the Hardy, Littlewood and Poylas inequality it can be shown that :

$$1 \leq B \leq L. \tag{2.19}$$

Finally the number of reference velocities can be chosen as

$$m = B + \lfloor 0.5 \rfloor + 1, \tag{2.20}$$

Where $\lfloor . \rfloor$ denotes the integer part of the real number. Therefore, using the above inequality we have:

$$2 \leq \mathrm{m} \leq \mathrm{L} + 1. \tag{2.21}$$

Now to determine the reference velocities we use $Y_0 = 0$ and $Y_j = \sum_{i=0}^{j-1} P_i, j = 1, 2, 3, \ldots L$. We then set $v_0 = v_{\min}$ if there exist any j such that $Y_j < \frac{i}{m-1} \leq Y_{j+1}$, then the reference velocities can be determined as follows:

$$v_i = c_j + \frac{\frac{i}{m-1} - Y_j}{Y_{j+1} - Y_j} \left(c_{j+1} - c_j \right), i = 1, 2, \ldots m - 1. \tag{2.22}$$

Then we have the m reference velocities

$v_0, v_1, v_2, \ldots v_{m-1}$.

2.4 Poststack imaging using PSPI

There are basically different types of migration based upon the domain in which the migration operates and the type of data on which it operates (Stacked or Unstacked).

Seismic Migration can be broadly classified into two types:

- Poststack Imaging.
- Prestack Imaging.

Poststack imaging as the name suggest is performed after stacking, i.e., on the stacked section. The data what we have from a stacked section is assumed to be either primary reflections or diffractions. This is performed so that the reflections and diffractions are plotted at their true locations [14, 38, 39]. Due to variable velocities and dipping horizons the data that is recorded for the surface positions is different from their sub-surface positions. So, migration is performed to move reflections to their true sub-surface locations. One of the practical aspects of migration is it requires true medium velocity. If we use a velocity model which is different from the medium velocity, then the migrated section can be misleading. Hence, it is very important to have a good estimate of the velocity model. In contrast with time migration methods, the depth migration methods can handle lateral velocity variations and, hence, requires a detailed velocity model in which all the lateral velocities are considered. But if the detailed velocity model was known we would have known the sub-surface geological model and, hence, there would have been no need of migration. In this respect, depth migration can be viewed as a mean of testing as initial geological hypothesis. Moreover, most of the good depth migrations are results of recursive process.

Here are few examples of migration: The red dots indicate the source and the receiver locations, the green dot represents the reflectors and the blue dots indicate the migrated result.

a) Migration of a point:

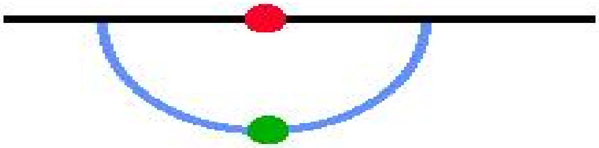

Figure 2.7: Migration of a point [1]

b) Migration of a diffraction:

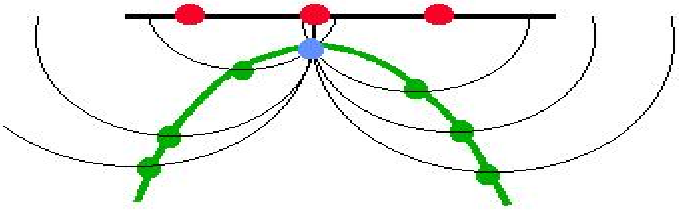

Figure 2.8: Migration of a diffraction [1]

c) Migration of a dipping event:

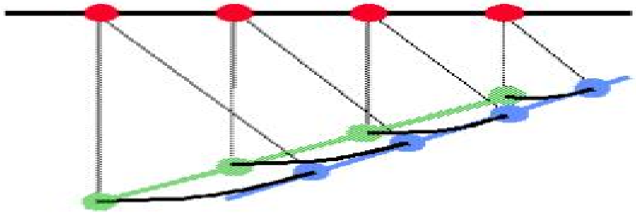

Figure 2.9: Migration of a dipping event [1]

2.4.1 The Model

For poststack migration, there is a standard data given by the Society of Exploration Geophysics and European Association of Geo-scientists and Engineers (SEG-EAGE) which is used in my simulation. The velocity model is a matrix of 1046x1024 with the maximum velocity of 4480.9 m/s and minimum velocity of 1500 m/s. This represents the offset of nearly 22 kms and the depth of nearly 4 kms. The zero offset section is also provided by the SEG which is a matrix of size 3001×1024, the dimensions here represents the offset of 22 kms and the travel time of the waves of 6 seconds with the sampling interval of 4 ms.

Figure 2.10 shows the velocity model and Figure 2.11 shows the zero-offset section of the standard benchmark SEG-EAGE dataset. We apply the PSPI algorithm shown in Figure 2.6 on the zero-offset section to obtain the final post stack image of the subsurface. It can be noticed that, the diffractions at the discontinuities have collapsed back to a point in the migrated section and the sub salt structure that is located at the bottom of the image is very sharply imaged. Figure 2.13 shows, the number of reference velocities used at each depth level while imaging.

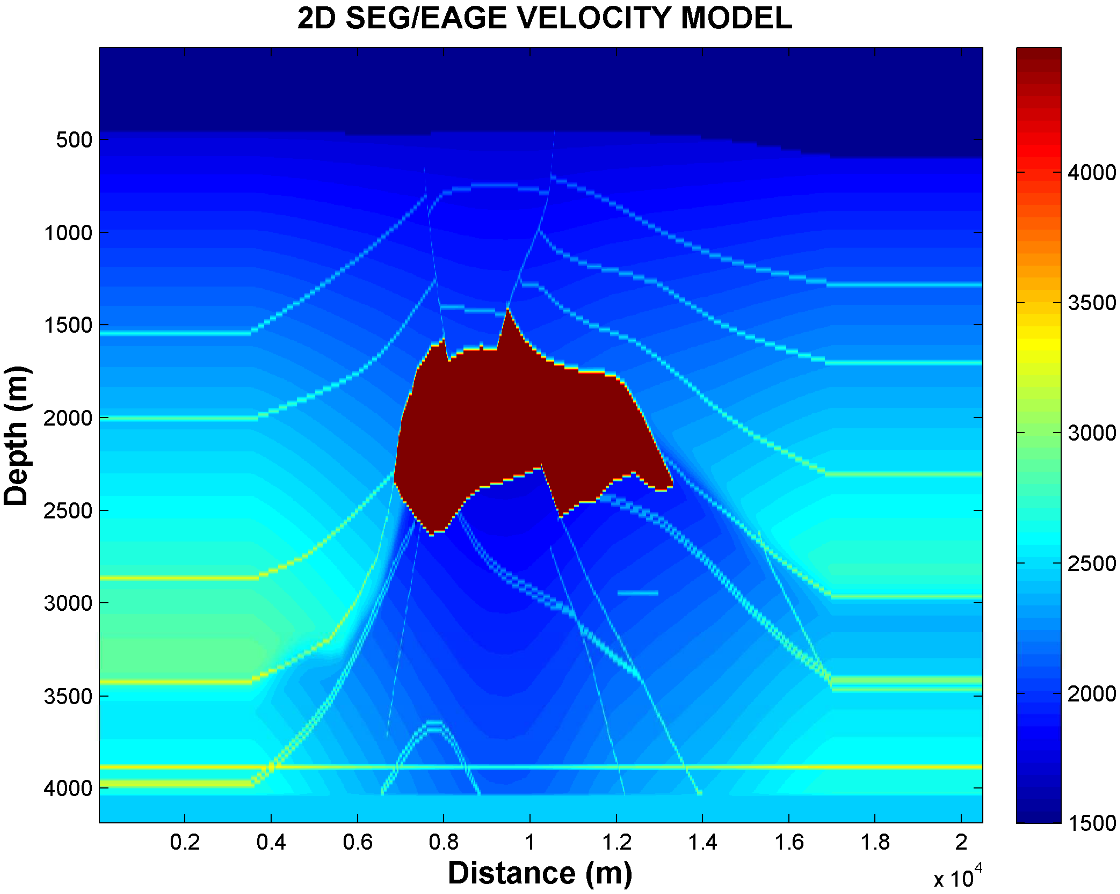

Figure 2.10: The SEG-EAGE velocity model.

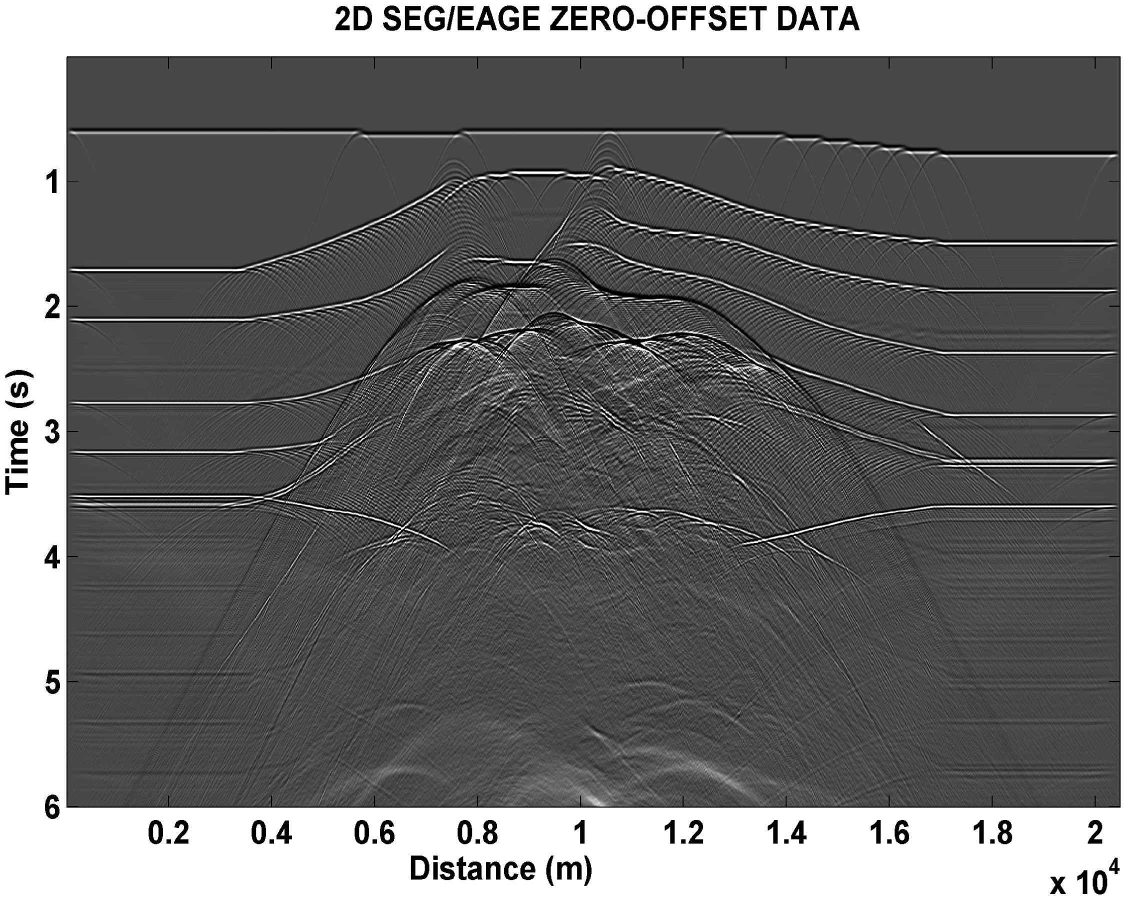

Figure 2.11: The SEG-EAGE zero-offset data.

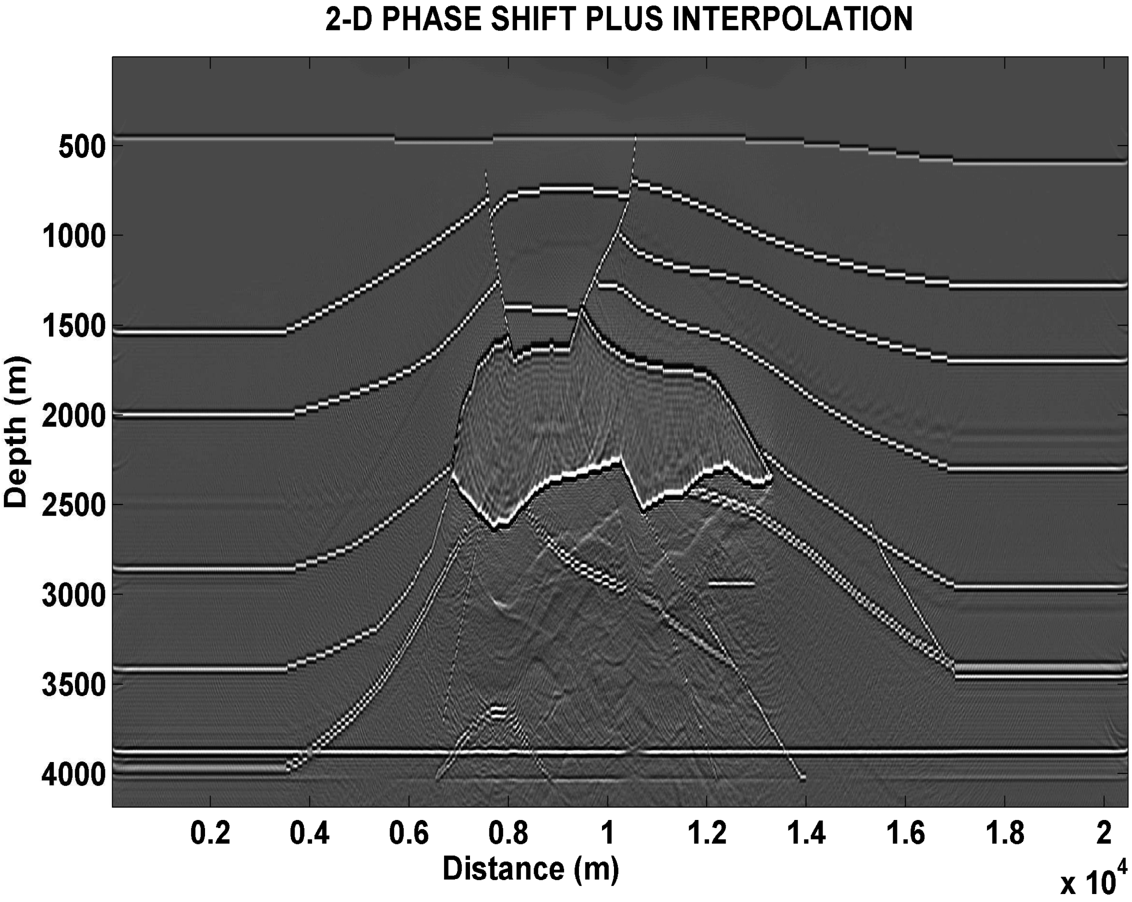

Figure 2.12: Migrated result using poststack PSPI.

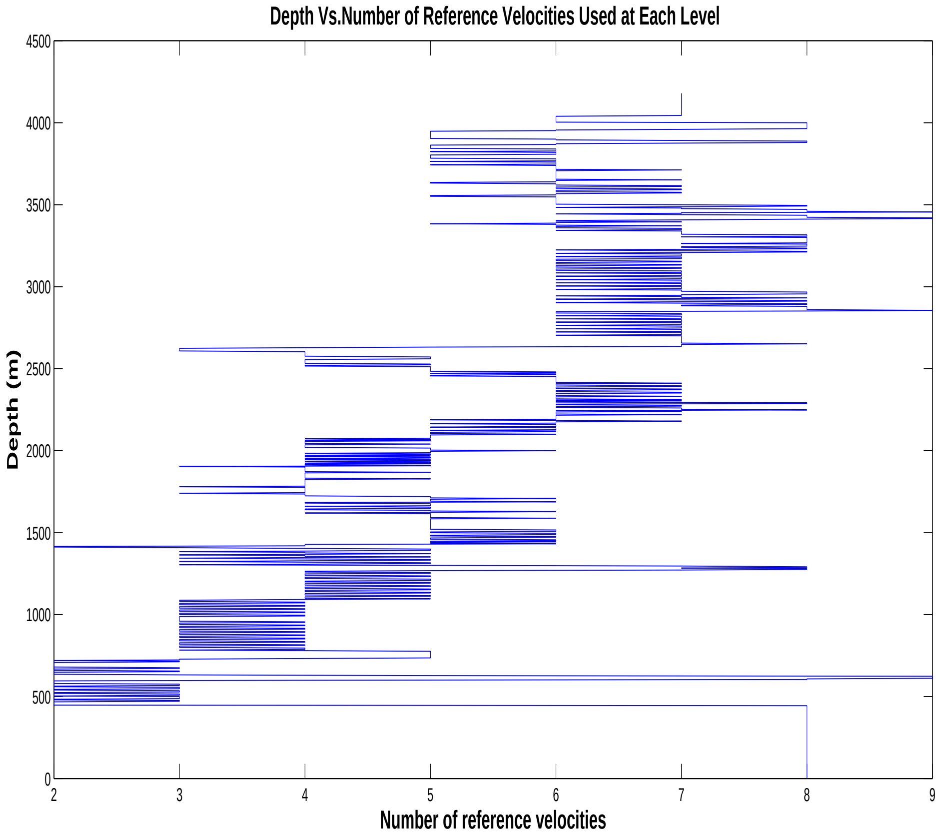

Figure 2.13: Number of reference velocities used at each depth.

2.5 Prestack imaging using PSPI

When the sub-surface structure is complex and there are lateral velocity variations then the reflection events are not hyperbolic and the stacking process does not work well. So, poststack migration does not give clear results. There has been number of ways to implement prestack migration on shot records as introduced by Schultz and Sherwood, Reshef and Kolsoff, Wapenaar and Bancroft and Ng. All these techniques use downward continuation scheme that involves there major operations in each iteration step either in depth or in time. The major issues that are to covered in these types of imaging schemes are:

The first one is the diffraction term which is used to collapse all the diffraction curves back to their diffraction points. This can be achieved by Kirchhoff summation or by finite difference. In our case, we use Phase shift plus interpolation method. The second thing is the thin lens term which is used in the depth migration for correcting the ray bending by applying the phase shift to the partially migrated data. This term is very sensitive to velocity. The third and last important thing is imaging condition that is used to extract the output point from the wavefield record at the time where source direct wave and the reflected wave are coincident.

In prestack imaging, the shot spread is shorter than the line length with the added benefit of multi fold coverage, the interpolation becomes increasingly reliable. Therefore, there are many advantages of phase-shift method such as the non-dispersive steep dip migration. This leads one to think that PSPI is more suitable for prestack imaging than poststack imaging in real time scenarios. Prestack imaging, as the name suggests, is performed on prestack data i.e. on common-shot gathers and can be performed in time or depth domain. It is an important tool in modeling salt diapers because of their complexity and this has immediate benefits if the resolution can pick up any hydrocarbons trapped by diapers. Prestack imaging is applied to avoid amplitude distortions due to smearing and non-hyperbolic move out. Hence, prestack time or depth imaging is a valuable tool in imaging seismic data. In the past, the main constraints on prestack imaging were the computation requirement the time and skill required to construct velocity model within a reasonable time. Advances in computing technology and formation of new imaging algorithms have eased these constraints. Prestack imaging for seismic reflection data is a popularly used tool for imaging complex geological structures such as salt domes, faults, thrust belts, and stratigraphic structures.

2.5.1 Prestack imaging using PSPI in acoustic medium

In acoustic medium, we assume that there are no losses as the wave propagates in the earth sub-surface. The amplitude of the wave doesn't die out as they propagate and the frequency content doesn't change. This can be sometimes referred to as an ideal case or the reference case. Like in poststack imaging, we had a zero-offset section, i.e., the stacked section for performing imaging but in this case we have common-shot records that has to be migrated first and then stacked in order to obtain the final image. The various steps that are performed in order to obtain the final image are:

- Generating the common-shot gathers in the acoustic medium.
- Applying the PSPI algorithm on various shot records generated from the previous step.Then apply an imaging condition on them as a part of PSPI algorithm itself.
- Later on we stack the results obtained by applying an imaging condition in order to produce the final image.

All this is done assuming no losses and without any change in frequency content as the seismic wave-propagates the earth sub-surface.

2.5.2 Generating common-shot gathers

In acoustic medium, we model the seismic energy which is a very valuable tool in seismology. It is useful in understanding wave propagation and seismic imaging. We use finite difference modeling scheme, in order to generate the common-shot records. There are few limitations with this technique but they provide us good results on the whole. The computational time is very high. After generating the shot records using finite difference scheme various bandwidth filters were applied to the seismogram's to determine their effect on the data. Increasing the sampling of the spatial grid enhances the results but requires a more intensive computation process. In addition, by applying an appropriate filter, erroneous data can be rejected by removing parts of the high frequency numerically dispersive signal.

Finite Difference (FD) Method

The basic problem in seismic is to determine the wave phenomena which is generated by triggering an impulse response in any arbitrary medium. This type of modeling is the basis to understand the seismic wave propagation and it can be used as an accessory for seismic imaging and inversion problems. Several numerical methods are available over the years such as finite difference, finite element and there is one more in the frequency domain. The seismic wavefields are computed digitally, hence, we need to sample the data into discrete intervals. As the number of samples increase the more is the computation time and a more accurate result can be obtained. Hence, choosing appropriate parameters to have balance between quality and computational time is very important.

The two-dimensional wave equation is given by:

$$\nabla^2 P = \frac{\partial^2 p}{\partial x^2} + \frac{\partial^2 p}{\partial z^2} = \frac{1}{v^2}\frac{\partial^2 p}{\partial t^2}, \tag{2.23}$$

where x and z are the horizontal axis and vertical axis respectively and t is the time. ∇^2 is the Laplacian operator of the spatial domain [40, 41, 42, 15]. This Laplacian operator can be approximated in a second order or the fourth order. The second order approximation to the Laplacian operator is given by:

$$\nabla^2 P_j^n = \frac{P^{n+1}{}_j - 2P_j^n + P_j^{n-1}}{\Delta x^2} + \frac{P^n{}_{j+1} - 2P_j^n + P_{j-1}^n}{\Delta z^2}. \tag{2.24}$$

This is done with the help of central difference operator, where n is the x coordinate and j is the z coordinate of the grid.

In order to reduce the computational time the horizontal and vertical distance should be same as the grid spacing, i.e., $\Delta x = \Delta z$. The fourth approximation is slower but the advantage is increased bandwidth. As each finite difference has some stability conditions, the following are the stability conditions for the FD modeling used:

$$\frac{V_{\max}\Delta t}{\Delta x} \leq \sqrt{\frac{1}{2}}, \tag{2.25}$$

$$\frac{V_{max}\Delta t}{\Delta x} \leq \sqrt{\frac{3}{8}}. \tag{2.26}$$

where all the parameters are in consistent units. The time derivative is calculated using a second order finite difference scheme:

$$\frac{\partial^2 P(t)}{\partial t^2} = \frac{P(t+\Delta t) - 2P(t) + P(t-\Delta t)}{\Delta t^2}. \tag{2.27}$$

The above equation shows that the wavefield at time $t + \Delta t$ is obtained from the wavefields at time t and $t - \Delta t$. This process is called time stepping and each wavefield is described as a snapshot. Therefore to generate the shot records we require two snapshots initially one at time 0 and other at time Δt.

All the three sides of the model are considered as absorbing boundaries except the top side where the source and the receivers are placed. This is explained in much details in ”Finite difference modeling of acoustic waves by CREWES” [27]. While generating the shot records, the sources are propagated as impulses and the resulting seismogram is filtered after creation by the desired source wavelet.

After generating the common-shot gather we perform the migration of each shot gather individually using the PSPI algorithm. Before we stack the images to obtain the final image we apply the imaging condition, i.e., it correlates the upcoming wavefield with the downgoing wavefield at each depth level.

2.5.3 Imaging conditions

A brief review of different constant velocity prestack depth migration approaches is presented here. The different investigated methods are prestack Kirchhoff depth migration, prestack depth migration with Claerbouts imaging conditions, which are deconvolution imaging condition and cross-correlation imaging condition and prestack depth migration with time excitation imaging condition [43]. In our case for imaging point we have used cross correlation and deconvolution imaging condition.

In this section, a brief review of the prestack depth migration approach using the cross correlation and deconvolution is presented. This review will give some insight about these methods and which ones preserve reflector amplitudes. The principle of reflector mapping was first introduced by Claerbout in 1971. The basic principle of reflector mapping is that, reflectors exist in the sub-surface when the first arrival of the downgoing wave is time coincident with the upgoing wave. This can give the correct phase but not the amplitude at the reflector. To obtain the correct amplitude at the reflector, Claerbout defines it as the ratio of the upgoing and downgoing wavefields at the sub-surface imaging location.

It correlates the upcoming wavefield with the downgoing wavefield at each depth level. Conventional seismic imaging is based on concept of single scattering. The waves propagate from the sources, interact with the reflector or the discontinuity and returns to the surface. This can be formulated as a process involving two steps [44]:

- A source wavefield traveling from source to the discontinuity.
- A receiver wavefield traveling from the discontinuity to the receiver at the surface.

These wavefields are four dimensional, i.e., the wave field is dependent on $P(x, y, z)$ and time. For imaging, we need to analyze if the wavefields match kinematically in time and then extract the reflectivity information using an imaging condition operating along the space and time axes. The two wavefields kinematically coincide at discontinuities. A conventional cross-correlation imaging condition based on the reconstructed wavefields can be formulated in the time or frequency domain as the zero lag of the cross-correlation between the source and receiver wavefields.

$$\Re\left(x\right) = \frac{P^{U}(x,\omega)P^{D*}(x,\omega)}{E(x,\omega)} d\omega. \tag{2.28}$$

Where, P^U represents upgoing field and P^{D*} is the complex conjugate of the downgoing wavefield. This operation exploits the fact that portions of the source and receiver wavefields match kinematically at sub-surface positions where discontinuities occur. In case of cross-correlation imaging condition the amplitudes achieves are not accurate and they invalidate further reflectivity inversion analysis. Thus deconvolution imaging condition overcomes this drawback by an illumination weighting function. This type of convolution imaging type can be mathematically formulated as:

$\mathrm{E}\left(\mathrm{x},\omega\right) = \mathrm{P}^{\mathrm{D}*}\left(\mathrm{x},\omega\right)\mathrm{P}^{\mathrm{U}}\left(\mathrm{x},\omega\right) + \varepsilon^2$ and $\varepsilon =$ mean of $\mathrm{P}\left(\mathrm{x},\omega\right)$ and$\mathrm{P}^{*}\left(\mathrm{x},\omega\right)$

This leads to a better image resolution. This implementation has the advantage of not stacking in the shot position dimension thus increasing resolution. The mean in the denominator adds stability to the function when there is a case of denominator going to zero.

2.5.4 The Model

For prestack migration, the Marmousi model is used which was first created in 1988 by the Institut Francais du Petrole (IFP) using very complicated geological model. This model consists of 158 horizontally layered horizons. A series of normal faults and resulting tilted blocks complicates the model towards its center, even though we have the correct velocity information it is very challenging for any migration method. The model sits under approximately 32 m of water and is nearly 10 km in length and 3 km in depth. The modeled data consists of 1251 receiver points which are 8.333 m separated from each other. The shot location refers to the location where the shot is created. This is performed at every 25 m spacing. Therefore, a total of 417 shot gathers are generated using this approach. A single length has a trace of 3 s and a sampling interval of 4 ms. The potential hydrocarbons are positioned around the three layers, the bottom-left triangle and the turtle back structure.

Shot records that are generated using finite difference in order to perform prestack migration in acoustic medium are shown in Figures 2.15-2.17. The result of acoustic prestack PSPI is shown in in Figure 2.18. From the Figure 2.18, it is observed that the result of acoustic prestack PSPI is sharp and crisp even with such complex data set.

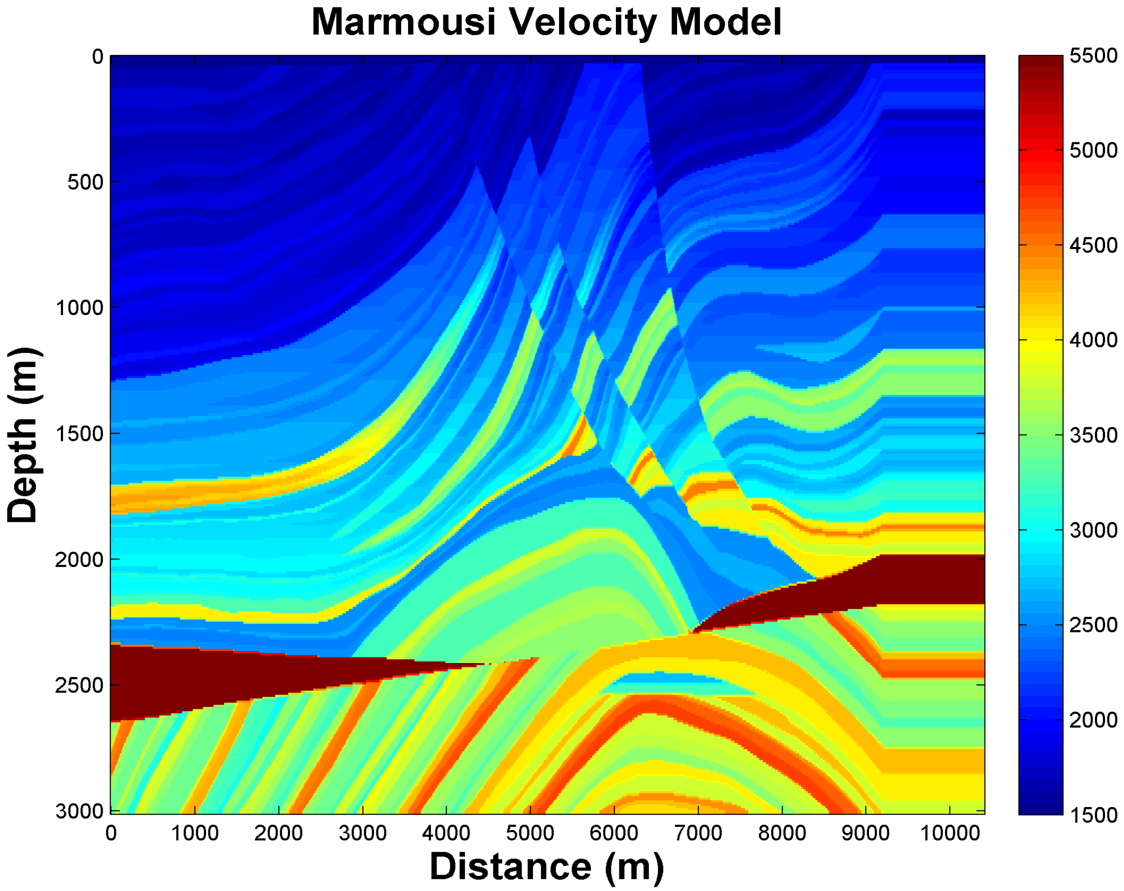

Figure 2.14: The Marmousi velocity model.

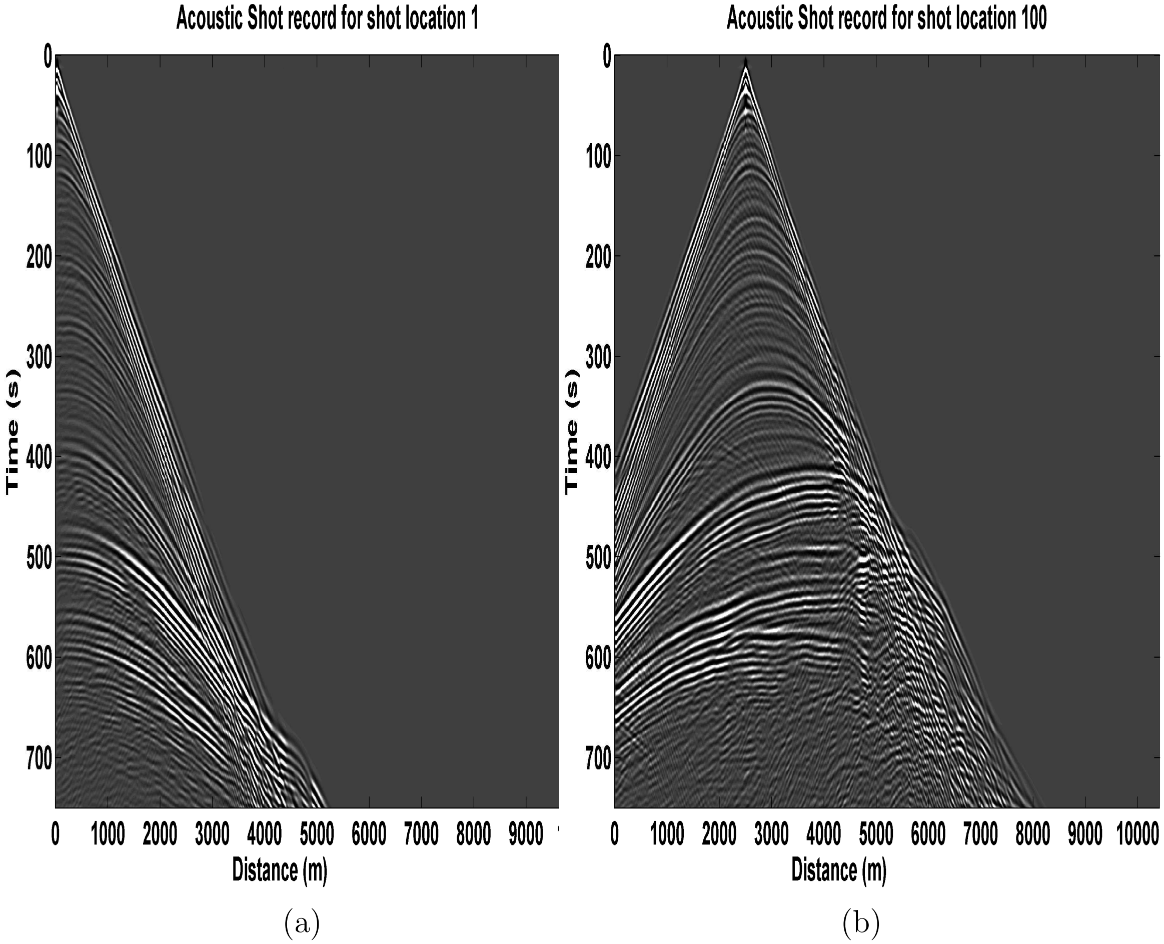

Figure 2.15: (a) The acoustic shot record generated at shot location 1. (b) The acoustic shot record generated at shot location 100.

2.6 Summary

In this chapter, the evolution of migration techniques are discussed along with the principle that migration follows. The various methods that are available to perform migration which are available in the literature are shown, where these techniques can either be used in time or frequency domain depending upon the type of problem. The poststack and prestack migration was performed in the acoustic medium using the PSPI method. In the next chapter, we will discuss

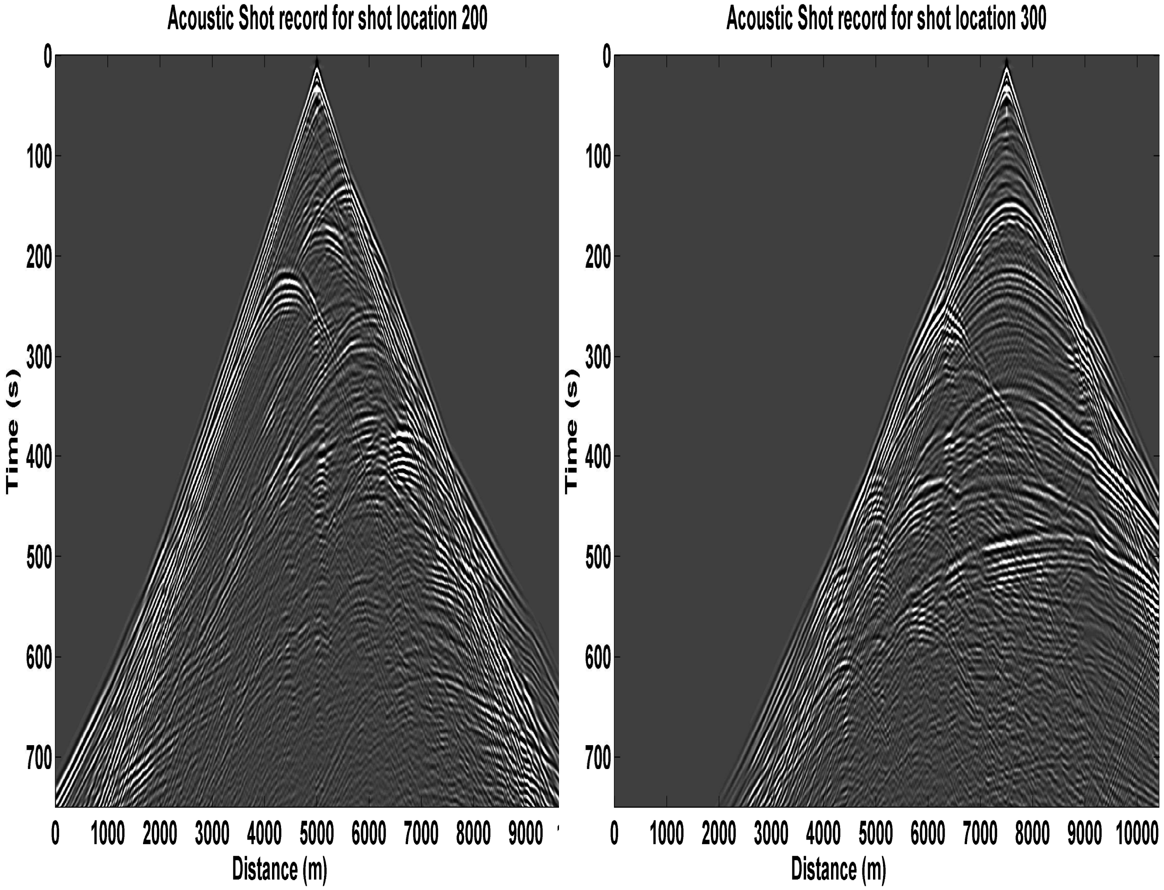

(a)

(b)

Figure 2.16: (a) The acoustic shot record generated at shot location 200. (b) The acoustic shot record generated at shot location 300.

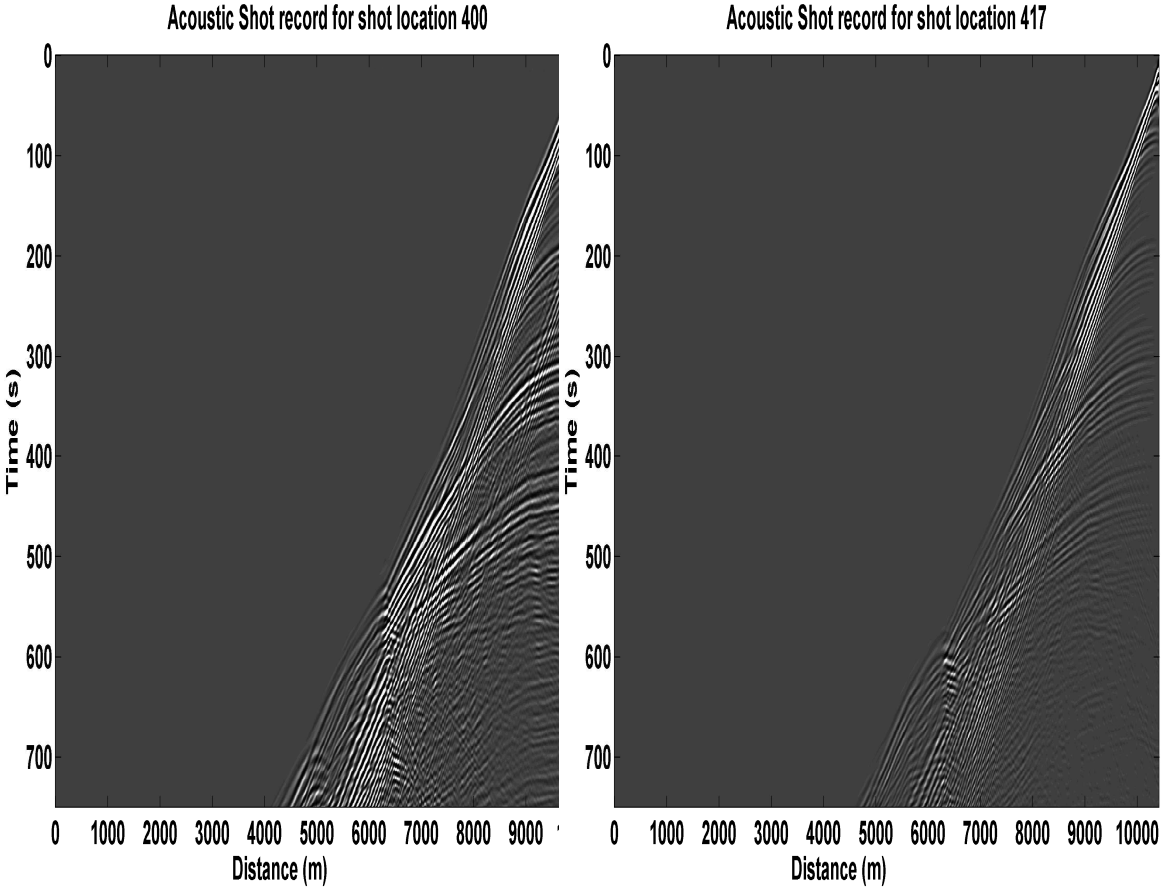

(a)

(b)

Figure 2.17: (a) The acoustic shot record generated at shot location 400. (b) The acoustic shot record generated at shot location 417.

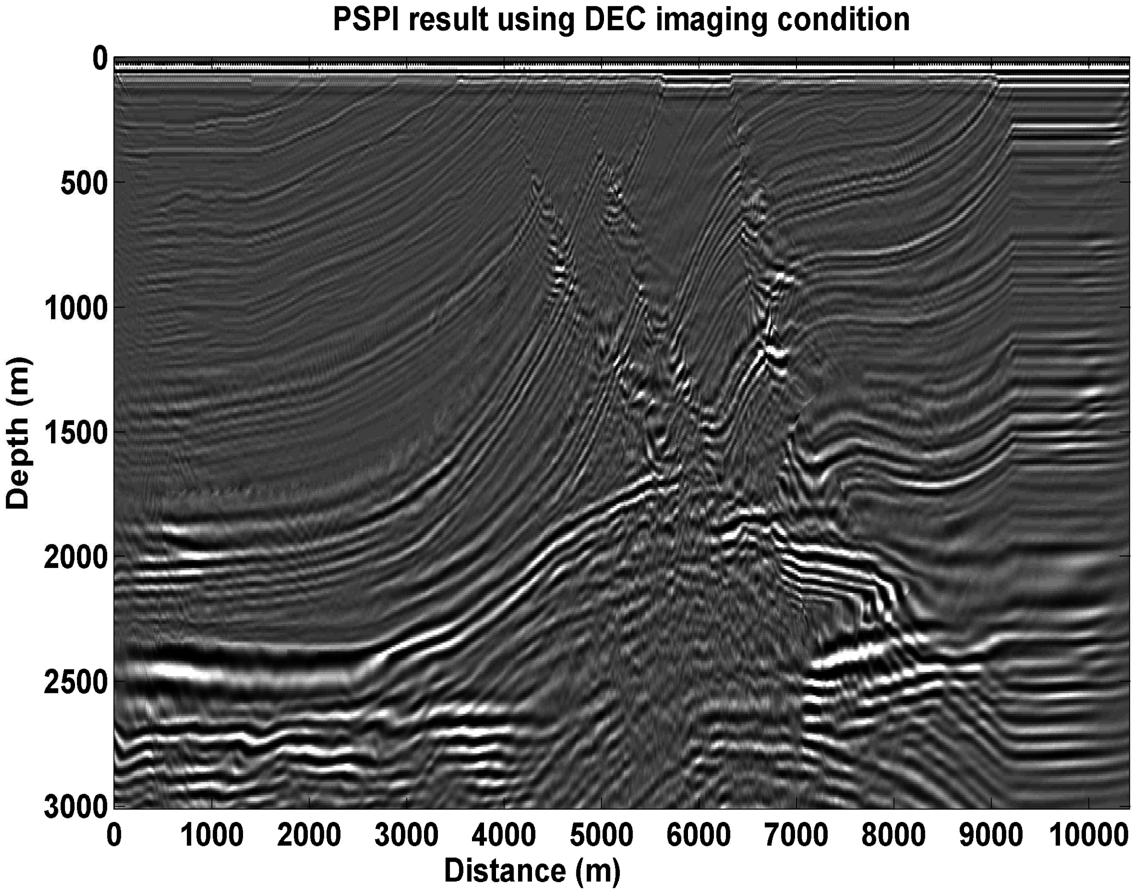

Figure 2.18: Acoustic prestack PSPI result for the standard Marmousi dataset.

how to incorporate the losses that takes place while the wave propagates in the sub-surface of the earth, i.e., we will focus towards visco-acoustic medium.

CHAPTER 3

PRESTACK MIGRATION USING PSPI IN VISCO-ACOUSTIC MEDIUM

3.1 Introduction

The seismic wave propagation in reality is much different from seismic wave propagation in ideal conditions. In ideal conditions, the medium is considered to be lossless and, hence, there is no dissipation of energy, no loss of amplitude and no change in frequency content in propagating waves [45]. However, when it comes to a real scenario, we have to consider the medium to be lossy and, thus, consider all the above mentioned factors that would affect the propagation of waves. The attenuation of seismic waves strongly depends upon the type of rocks we are going to encounter while propagating [46]. Therefore, it is important for exploration geophysicists to understand these effects and extract more detailed information, in order to obtain images of better resolution.There is, at the outset, no justification for neglecting the effect of absorption and dispersion and, hence, this effect is being incorporated into seismic modeling schemes [47].

The aim of this work is to show that the prestack depth imaging using Phase Shift plus Interpolation (PSPI), which compensates for absorption, is feasible, since PSPI is considered to be very accurate technique in $(f-k)$ domain for seismic imaging (see chapter 2). The implementation is performed on the benchmark 2-D standard Marmousi dataset. As all depth migration schemes, we assume velocity model as a priori information and we perform migration using PSPI [6]. In order to consider the absorption we introduce a small imaginary term with the velocity model which represents the absorption in the model [29]. This leads us to two parameters: one is the phase velocity and the other is the quality factor, which are related to real and imaginary parts of the velocity model, respectively. Now to compensate for this absorption we include a new coefficient in our PSPI algorithm, which will perform compensation for absorption [48, 46]. These coefficients are obtained from the velocity model and the quality factor (Q), which is defined as a parameter for absorption of the medium, as shown later in this chapter.

The seismic shot records that are generated using finite difference method in acoustic medium [49] is modified to include the absorption using the quality factor. This model is obtained by taking the square root of the velocity model, which represents absorption as suggested in [29].

3.2 Visco-acoustic PSPI with compensation for absorption

In a linear visco-acoustic medium, the pressure equation in the frequency domain can be expressed as [29]:

$$\left\{\partial_i^2 + \frac{\omega^2}{M\left(x,\omega\right)/\rho}\right\} + P\left(x,\omega\right) = 0, \tag{3.1}$$

where ∂_i^2 denotes partial derivatives in Cartesian coordinates, $M\left(x,\omega\right)$ denotes the bulk modulus, ρ is the density and $P\left(x,\omega\right)$ represents the pressure wavefield in x and ω domain.

From Eq.(3.1), we see that square of the velocity is represented as the ratio of $M\left(x,\omega\right)/\rho$. Therefore the Fourier transform of the above equation w.r.t x is given as :

$$\left\{\partial_i^2 + \frac{\omega^2}{v^2\left(\omega\right)} - k_x^2\right\} + P\left(k_x,z,\omega\right) = 0. \tag{3.2}$$

There are two independent solutions to this wave equation are:

$$P\left(k_x, z+\Delta z, \omega\right) = e^{\pm i\sqrt{\omega^2/v^2(\omega)-k_x^2}.\Delta z} P\left(k_x, z, \omega\right). \tag{3.3}$$

The positive sign in the extrapolators represents downward extrapolation of the downgoing wave and negative sign represents downward extrapolation of the upgoing wave. Note that i here represents $\sqrt{-1}$.

In order to compensate for the absorption of energy from source to the receiver location both the forward and the backward wave propagation should be compensated [29]. As explained earlier, it is common to account for absorption by making velocity complex.

In Eq.(3.3), the term $\frac{\omega}{v}$, can be defined as:

$$\frac{\omega}{v\left(\omega\right)} = k_\omega - i\alpha_\omega, \tag{3.4}$$

where k_ω and α_ω are wavenumber's corresponding to real and imaginary parts of the velocity. The imaginary term in the above equation is responsible for absorption in the propagating waves. This causes the shot records that are generated using Finite Difference (FD) to be smoother, i.e., incorporating the absorption in the propagation waves.

Now, when we divide this equation by frequency ω on both sides we obtain:

$$\frac{1}{v\left(\omega\right)} = \frac{1}{v} - i\frac{\alpha_\omega}{\omega}, \tag{3.5}$$

since the wavenumber k_ω is defined as the ratio of frequency over velocity, i.e., $\frac{\omega}{v}$.

Hamilton [29] provides a relationship between absorption and Q-values which is given as :

$$\frac{1}{Q} = \frac{2\alpha_\omega v}{\omega - \frac{\alpha_\omega^2 v^2}{\omega}}. \tag{3.6}$$

Eq.(3.6) is valid for low values of Q. Hence, the absorption coefficient is given as:

$$\alpha_\omega = \frac{\omega Q}{v}\left(\sqrt{1+\frac{1}{Q^2}} - 1\right). \tag{3.7}$$

Eq.(3.7) can be approximated, if the quality factor of greater than 10 [29].

$$\alpha_\omega = \frac{\omega}{2vQ}, \tag{3.8}$$

Therefore, substituting Eq.(3.8) in Eq.(3.5) we obtain:

$$\frac{1}{v(\omega)} = \frac{1}{v} - i\frac{1}{2vQ}. \tag{3.9}$$

Thus, this model gives high absorption in low-velocity regions and low absorption in high velocity regions maintaining Q values between 40 to 70. Such Q-values are commonly reported in literature in case of absorption [29].

3.2.1 Absorption effects and its compensation

The wavefield at each depth level is computed using the formula shown in Eq. (3.3). Now, this equation is modified to compensate for the effect of absorption by changing the extrapolator term in the equation.

Therefore by substituting Eq. (3.4) in Eq.(3.3) we obtain:

$$P\left(k_x, z+\Delta z, \omega\right) = e^{\pm i\sqrt{\left(k_\omega - i\alpha_\omega\right)^2 - k_x^2}.\Delta z} P\left(k_x, z, \omega\right). \tag{3.10}$$

Now, just for simplicity, if we considering the case of vertical propagation of waves. For a downgoing wave, as explained earlier, we consider the positive sign in the extrapolation term. Therefore, we have the following result:

$$P\left(0, z+\Delta z, \omega\right) = e^{ik_\omega \Delta z} e^{\alpha_\omega \Delta z} P\left(0, z, \omega\right), \tag{3.11}$$

- A real wave propagating downwards will have k_ω >0 and attenuation would be achieved when α_ω <0.
- However, we wish to use an extrapolator that compensates for the loss of energy that the wave has experienced during its propagation from source down to the reflecting surface.
- Therefore, we keep $e^{i[k_\omega + i\alpha_\omega]\Delta z}$ as the extrapolator for the downgoing wave.

For an upgoing wave, we consider the negative sign in the extrapolator term and for the vertically propagating waves the wavefield at the next depth level can be obtained as follows:

$$P\left(0, z+\Delta z, \omega\right)=e^{-ik_{\omega}\Delta z}e^{-\alpha_{\omega}\Delta z}P\left(0, z, \omega\right). \tag{3.12}$$

This wave is propagating upwards, losing amplitude on its way. Since α_{ω} <0, the downward extrapolation in the above equation will be boost the amplitude and, thereby, compensate for the lost amplitude on the way up from reflector to point back to the source. Thus $e^{i[k_{\omega}-i\alpha_{\omega}]\Delta z}$ is the correct extrapolator for the upgoing wave. The flow chart for visco-acoustic PSPI is shown in Figure (3.4), which is used to perform prestack imaging. This visco-acoustic PSPI algorithm is applied on every shot record. After applying the seismic imaging condition, we obtain a final image of correlated wavefields [15].

The Computational Complexity for visco-acoustic PSPI

As in the case of acoustic PSPI, we have calculated the cost of imaging in visco-acoustic medium. The computational cost for imaging using visco-acoustic PSPI using N_{FFT} FFT points and n_{ref} velocities at each depth slice is given as follows: For complex multiplications,

$$PSPI-COST_{X}=2N_{FFT}\times n_{ref}+\left(n_{ref}+2\right)\times\frac{N_{FFT}}{2}\log_{2}N_{FFT}, \tag{3.13}$$

For real-complex multiplications,

$$PSPI - COST_X = N_{FFT} \times n_{ref}. \tag{3.14}$$

The additional $N_{FFT} \times n_{ref}$ term in computing multiplication cost corresponds to the extra term in the extrapolator term which is responsible for compensation. This is a real-complex multiplication and requires two flops as given by [36]. For complex additions,

$$PSPI - COST_+ = (n_{ref} + 2) \times N_{FFT} \log_2 N_{FFT}. \tag{3.15}$$

The number of complex additions remains the same. In both cases, each complex multiplication requires six flops whereas each complex addition requires two flops as given in [36].

3.3 Generating common shot gather in visco-acoustic medium

In acoustic medium, we generate shot records based on a finite difference (FD) technique [49]. When it comes to visco-acoustic medium, we can generate seismic shot records based on acoustic shot records, by applying a Q-filter on every shot record that is obtained for the acoustic medium. This will give us shot records with absorption and dispersion. The Q-filter matrix is generated with the help of a spike wavelet that is varying with respect to absorption as in the Q-model. This forms a matrix which has values varying from 1 to 0 in the diagonal w.r.t Q-model and the other parts are almost zeros.

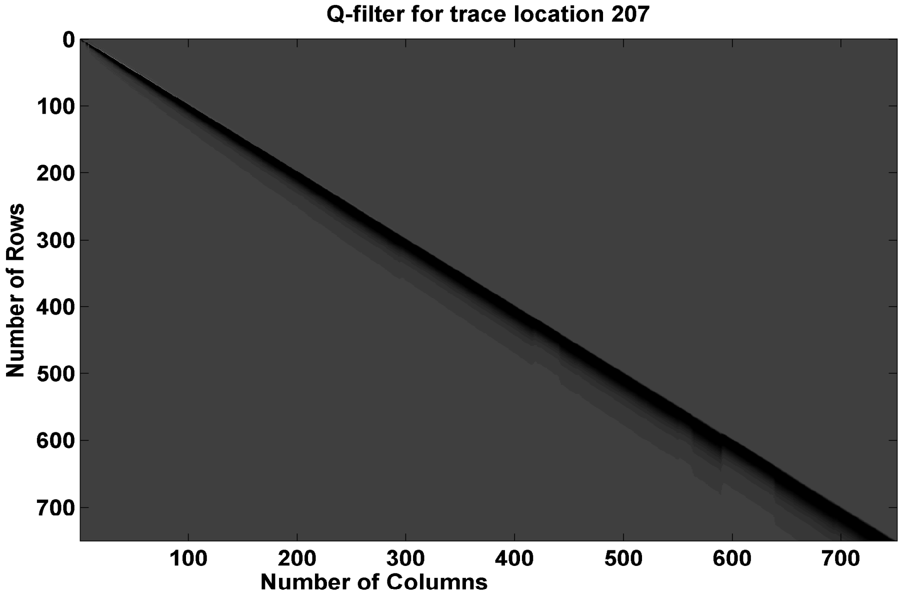

Figure 3.1: The Q-filter generated for trace location 207 in Q-model.

The Q-filter generated for one particular trace of Q-model is shown in Figure (3.1). It is clearly visible that, the Q-filter is very sharp at the starting point of the diagonal and as it moves down the diagonal it spreads and incorporates the absorption w.r.t. Q values. The size of Q-filter is 751 × 751 this is generated for every trace in the Q-model and each trace in the acoustic shot is multiplied with Q-filter pertaining to that particular trace in order to obtain visco-acoustic traces.

This is continued for all the traces by generating Q-filter's from each Q-model trace and then multiplying with the acoustic shot trace till we generate all the visco-acoustic shot records. That is:

$$(visco - acoustic\ trace) = (Q - filter) * (acoustic\ trace)\,. \tag{3.16}$$

In Marmousi model, the model is (see Figure 3.2) is not defined with absorption so a easily reproducible Q-model is obtained, which is responsible for absorption as suggested in [29]:

- Whenever the velocity value exceed 1500 m/s, we consider the square root of this value as the Q factor value.
- And for water layer, i.e., when the velocity is below 1500 m/s we consider Q factor as infinity.

The obtained Q-model using the above mentioned approach is as shown in Figure 3.3.

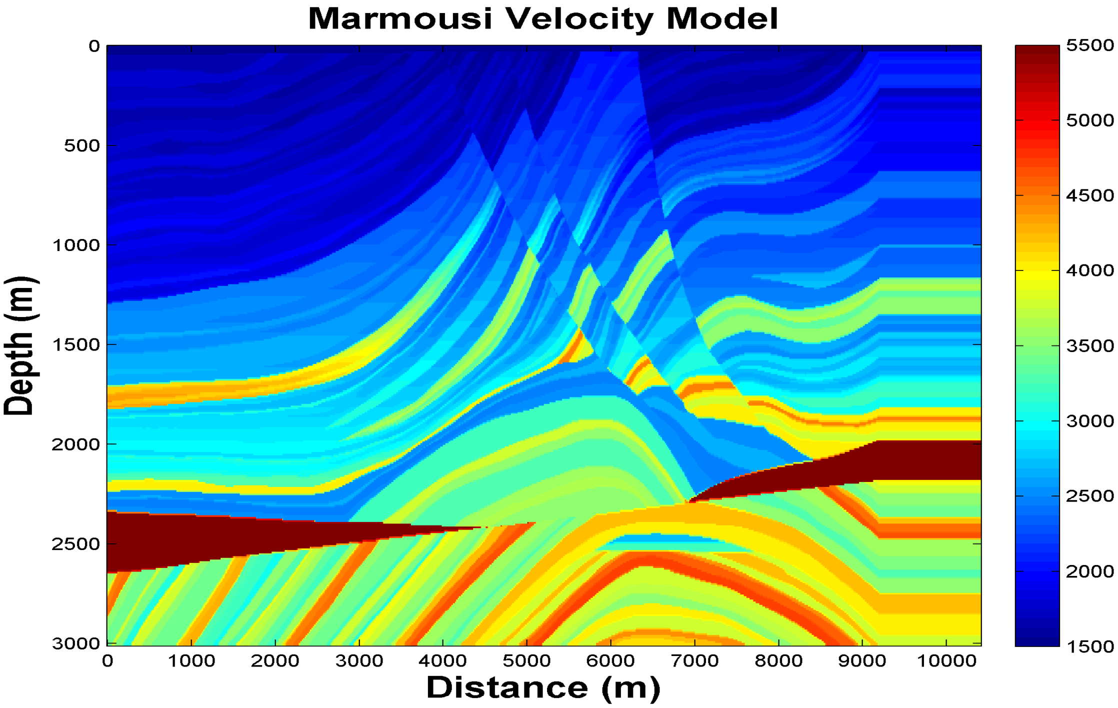

Figure 3.2: The Marmousi Model with receiver spacing of 8.333 meters in x direction.

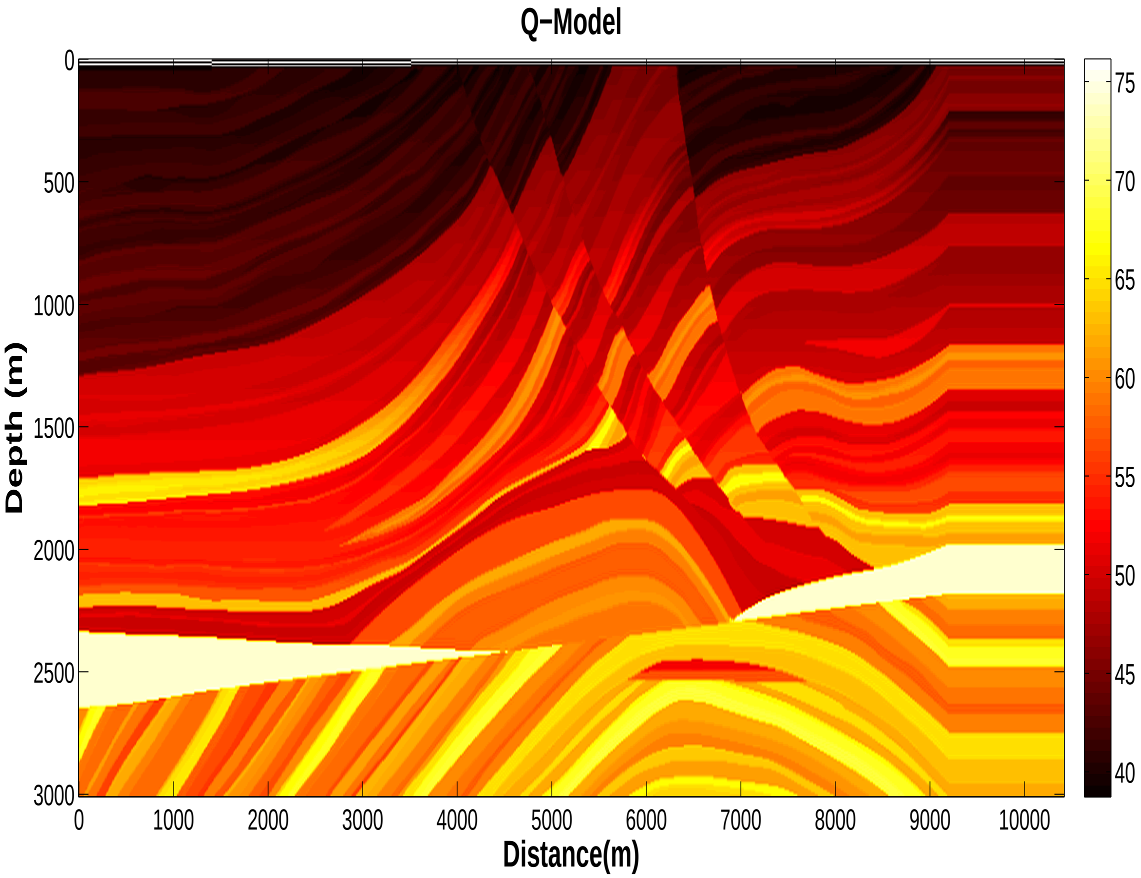

Figure 3.3: The Q-model of the Marmousi model shown in Figure 3.2

In this way, all the shot records in visco-acoustic medium are generated trace by trace. Now, if we compare the acoustic shots and the visco-acoustic shot that are generated with the help of Q-model (see Figure 3.5 - 3.10), one can clearly realize the amplitude losses and change in frequency content. The amplitude loss is visible with the smoothening effect in the traces and the frequency change is visible by the thickening of the traces, when compared to the acoustic shots.

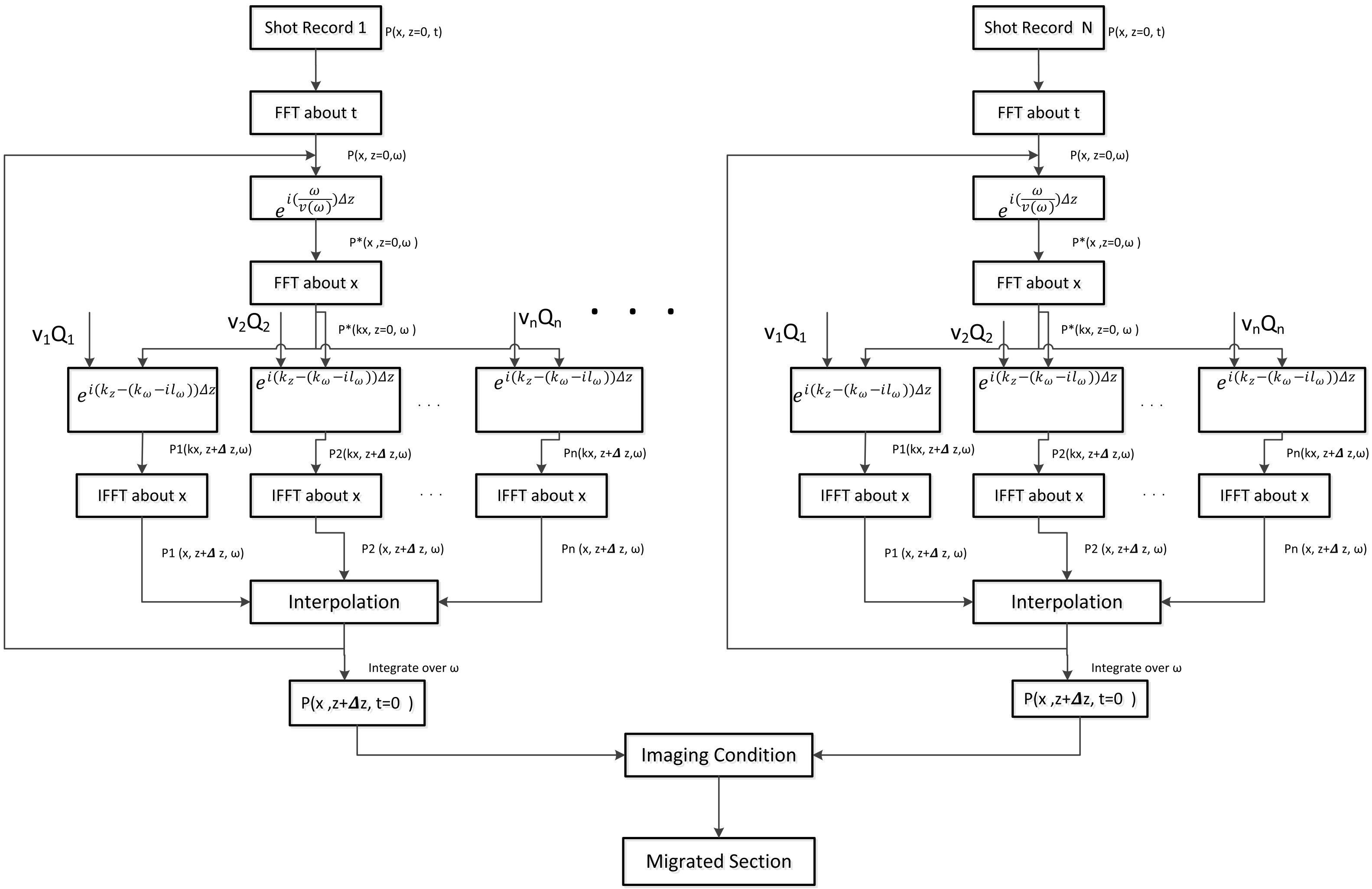

Figure 3.4: Visco-acoustic PSPI algorithm for N seismic records.

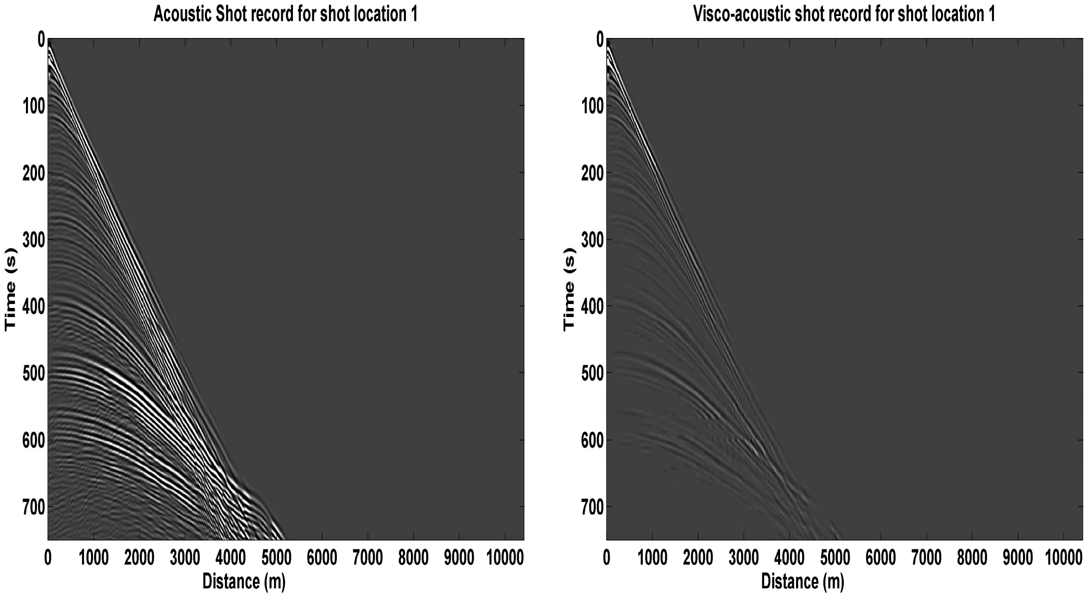

(a) (b)

Figure 3.5: (a) The acoustic shot record generated at shot location 1. (b) The visco-acoustic shot record generated at shot location 1.

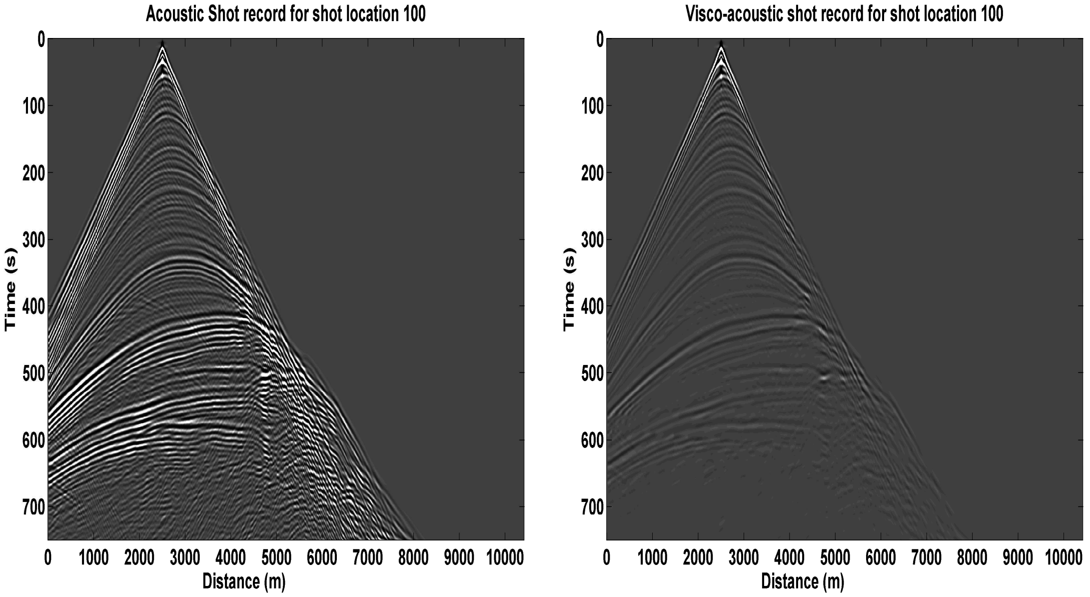

(a) (b)

Figure 3.6: (a) The acoustic shot record generated at shot location 100. (b) The visco-acoustic shot record generated at shot location 100.

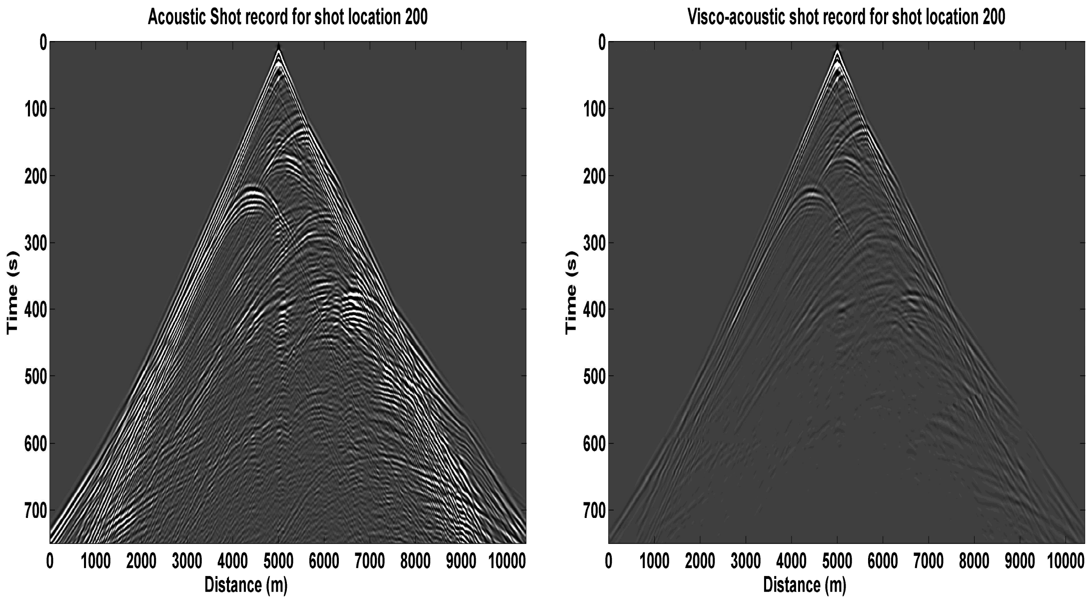
Acoustic Shot record for shot location 200

Visco-acoustic shot record for shot location 200

(a) (b)

Figure 3.7: (a) The acoustic shot record generated at shot location 200. (b) The visco-acoustic shot record generated at shot location 200.

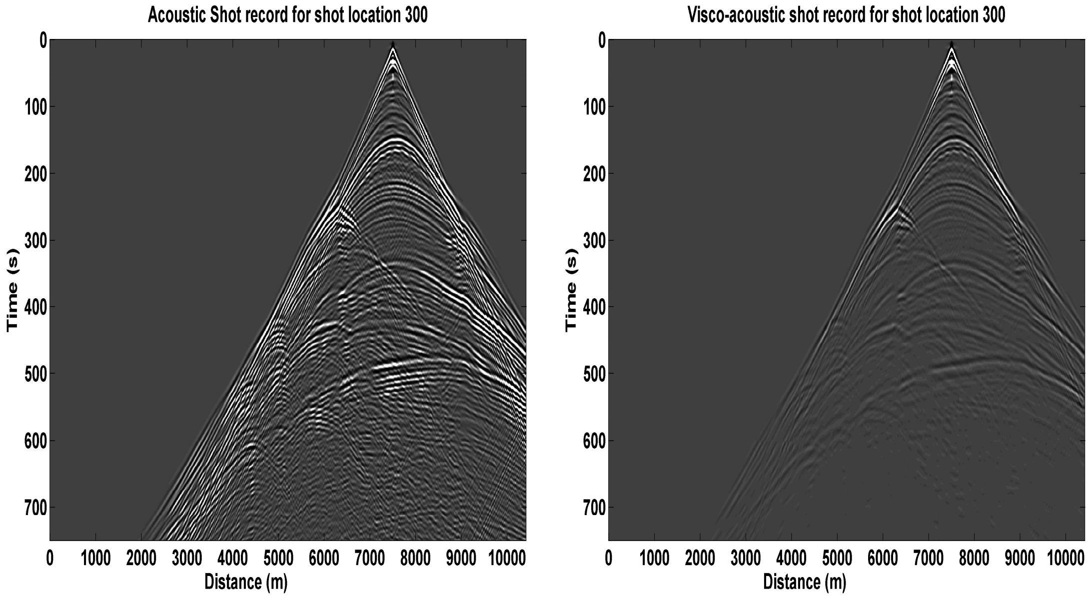
Acoustic Shot record for shot location 300

Visco-acoustic shot record for shot location 300

(a) (b)

Figure 3.8: (a) The acoustic shot record generated at shot location 300. (b) The visco-acoustic shot record generated at shot location 300.

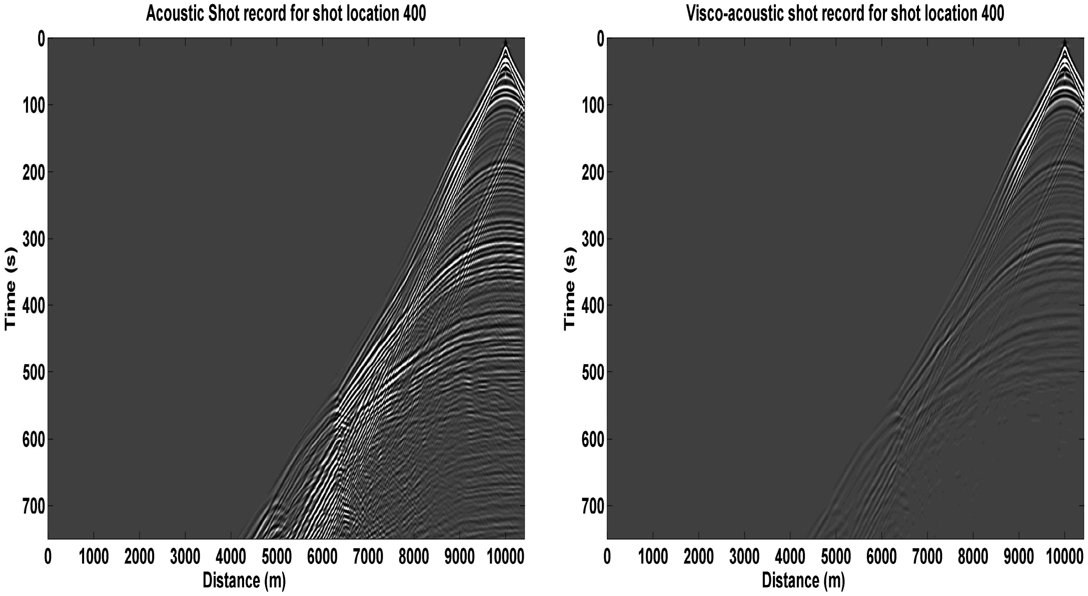

(a) (b)

Figure 3.9: (a) The acoustic shot record generated at shot location 400. (b) The visco-acoustic shot record generated at shot location 400.

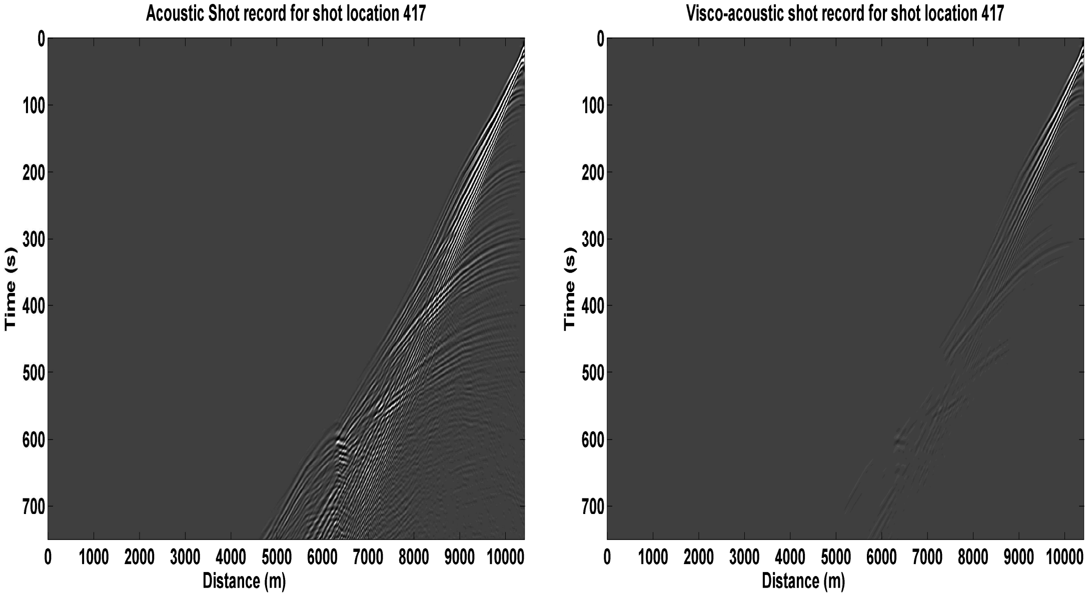

(a) (b)

Figure 3.10: (a) The acoustic shot record generated at shot location 417. (b) The visco-acoustic shot record generated at shot location 417.

3.4 Simulation Results

The simulation is performed using MATLAB software which utilizes Intel(R) core(TM) i5-3210M CPU at 2.50 GHz and 4 GB RAM. The result of prestack imaging using acoustic PSPI for visco-acoustic shot records can be seen in Figure 3.11. Clearly, the seismic image is smoothened as compared to Figure 2.18.

The visco-acoustic PSPI algorithm shown in Figure 3.4 is repeated for all the 417 shot records that are taken at every 25 meters distance on the velocity model. The cut-off of the extrapolator operators that are different from the PSPI that is used in acoustic case and this change is responsible for compensation for absorption. The result of this technique is then stacked using deconvolution method and, hence, the final image is obtained.

The result of prestack imaging using visco-acoustic PSPI for visco-acoustic shot records can be seen in Figure 3.12. It is clear that taking into account the losses, imaging has greatly enhanced the imaging results, when compared to Figure 3.11.

The comparison of computational cost required to migrate a depth slice of a single shot record using 2048 FFT points and an average of six reference velocities, i.e., n_{ref}=6 using acoustic and visco-acoustic PSPI is as shown in Table 3.1.

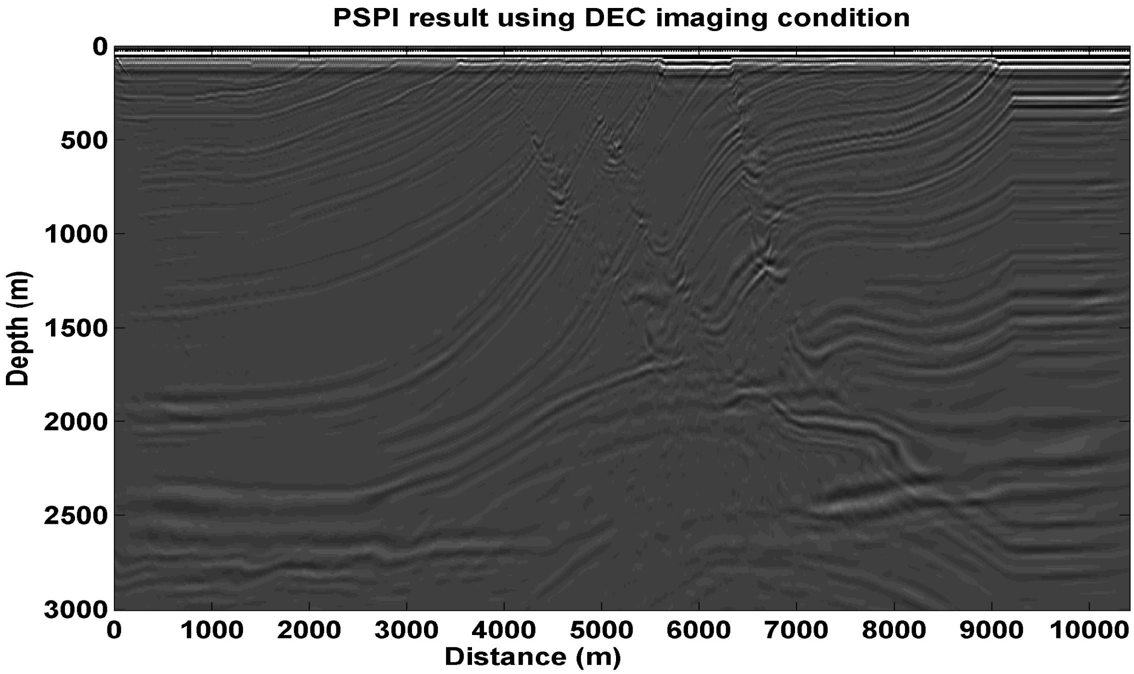

Figure 3.11: Prestack migrated image using acoustic PSPI and visco-acoustic shot records.

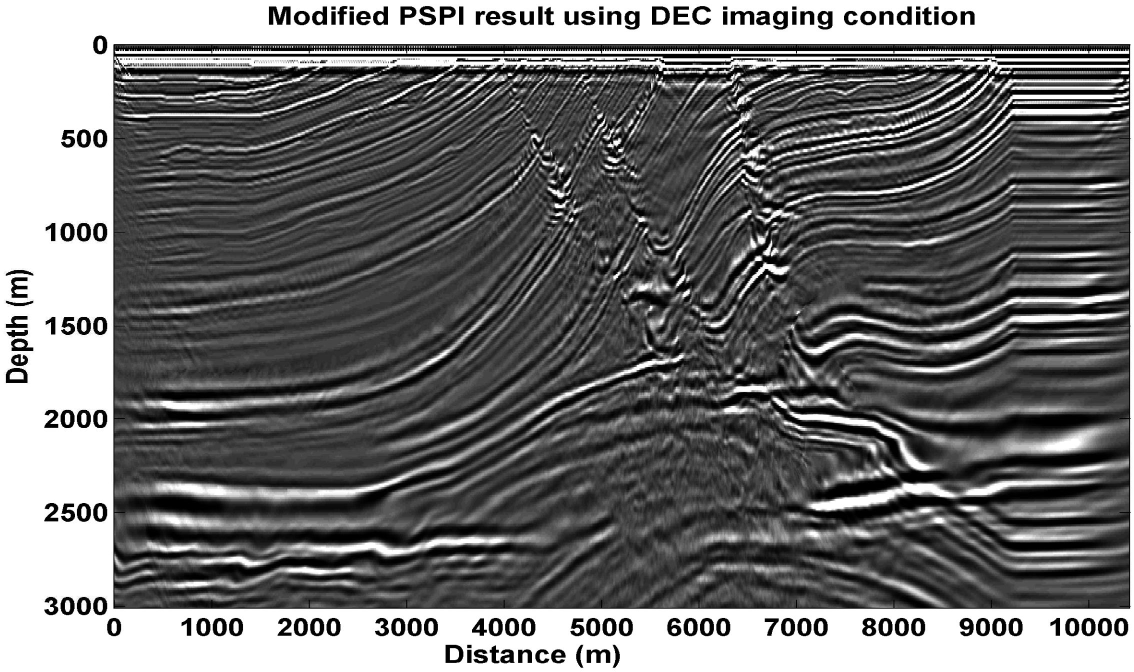

Figure 3.12: Prestack migrated image using visco-acoustic PSPI and visco-acoustic shot records.

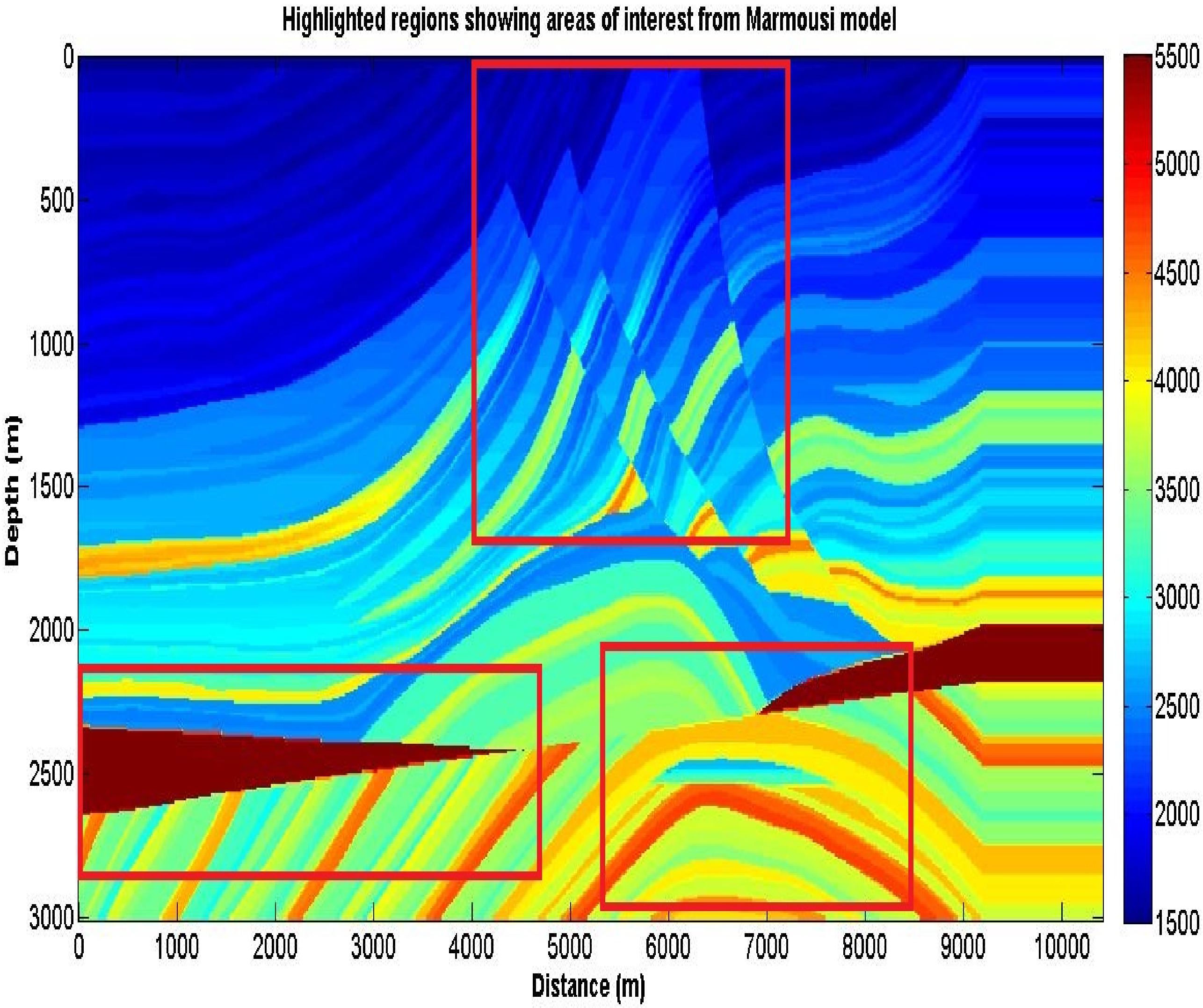

Figure 3.13: Highlighted regions showing areas of interest in Marmousi model.

We compare the obtained results by zooming into areas of interest, Figure 3.13, shows the areas of interest from the Marmousi velocity model. In the Figure 3.14, the formation of the triangle on the bottom left (pinch out) in the velocity model is more likely visible in the visco-acoustic PSPI algorithm when compared to the acoustic PSPI. The three layers which are called faults in seismology are not so sharp in acoustic PSPI method, whereas in visco-acoustic PSPI the layers are very sharp and crisp. At the location x= 6500 and y= 2500 in the model there is a small variation which could possibly be a trap for the hydrocarbon is clearly visible in visco-acoustic PSPI.

Computational Complexity

It is observed that the computational complexity in case of visco-acoustic PSPI is more when compared to acoustic PSPI. The visco-acoustic PSPI has additional real-complex multiplications which make it more complex when compared to acoustic PSPI. Even though the algorithm is complex it is quite feasible for the quality of results we obtain at the end. Table 3.1 demonstrates the number of incurred multiplication flops (the number of addition flops are the same for both cases which is equal to 360448). Clearly there exists an additional 6.25% in terms of number of flops to generate visco-acoustic images via the visco-acoustic PSPI as compared to the case of acoustic PSPI.

Technique	×s Flops	%
Acoustic PSPI	668,128	-
Visco-acoustic PSPI	712,692	6.25

Table 3.1: Comparison of number of flops (for the complex multiplications, real-complex multiplications and complex additions) at a depth slice of single shot record for migrating the 2D Marmousi model, using acoustic and visco-acoustic PSPI methods (with six reference velocities and 2048 FFT points).

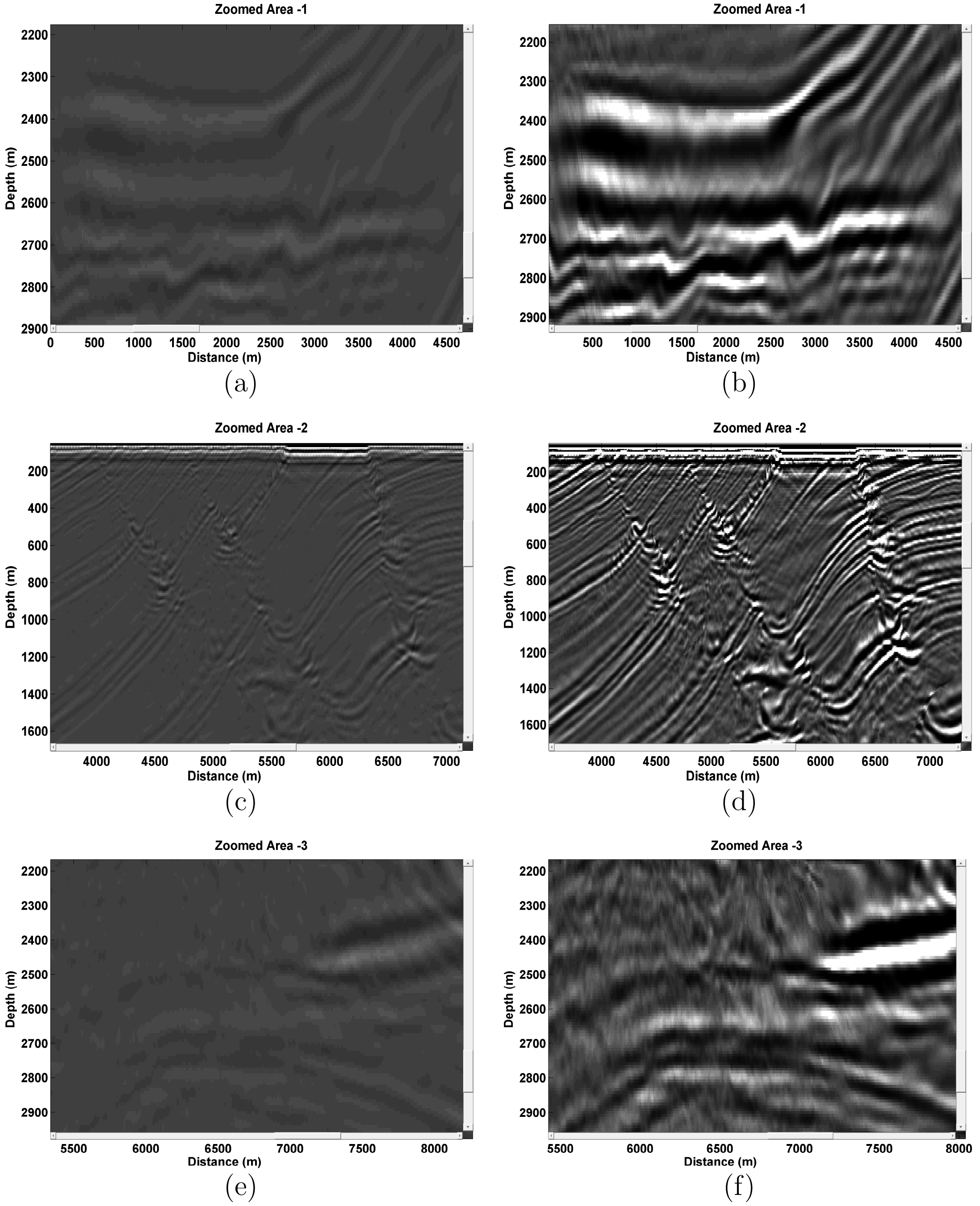

Figure 3.14: (a) The zoomed area-1 from the acoustic PSPI with visco-acoustic shots. (b) The zoomed area-1 from the visco-acoustic PSPI and visco-acoustic shots. (c) The zoomed area-2 from the acoustic PSPI with visco-acoustic shots. (d) The zoomed area-2 from the visco-acoustic PSPI and visco-acoustic shots. (e) The zoomed area-3 from the acoustic PSPI with visco-acoustic shots. and (f)The zoomed area-3 from the visco-acoustic PSPI and visco-acoustic shots.

3.5 Summary

In this chapter, the PSPI algorithm has been modified in order to compensate for the absorption. For comparison, we obtained results for both, visco-acoustic data using acoustic PSPI algorithm and visco-acoustic data with visco-acoustic PSPI algorithm. It is clearly evident from the images that the change in the extrapolator term in the PSPI algorithm using the Q-model, compensates for the absorption effect. The highlighted areas are well imaged in the visco-acoustic PSPI case as compared to acoustic PSPI case while dealing with visco-acoustic shot records. Therefore, we can conclude that the image obtained by visco-acoustic PSPI using visco-acoustic shot records has better resolution when it comes to seismic imaging.

CHAPTER 4

SEISMIC IMAGE QUALITY ASSESSMENT

4.1 Introduction

Over the years, there exists hundreds, if not more, seismic imaging techniques [6, 25, 26, 39, 50, 51, 35] in time and frequency domain. Some of the techniques image accurately compared to others and some of them do not, depending upon many factors such as the complexity of the geology, the accuracy of the velocity model, etc. The quality of the seismic images is determined subjectively by the geophysicists' naked eyes. The distortion in seismic images that are developed using seismic imaging techniques mostly occur while acquisition and processing. This distortion affects the ability of humans to exact the information from the seismic images.

In seismic imaging, we usually are looking for an image with less noise and of high spatial resolution in order for geophysicists to perform better seismic interpretation. This work is an attempt to provide an objective measure on the seismic images quality. The idea of developing objective methods for quality of images has been used extensively in the area of image processing [11, 16, 52, 53]. It is known as Image Quality Assessment (IQA). IQA can be classified into three categories: (1) full-reference based method (2) reduced-reference based method and (3) non-reference based method. There has been a few proposed non-reference based IQA in recent years, which are for general purpose and are based on training and testing methods [11, 16, 52, 53]. Here, we propose to assess the quality of a seismic image based on non-reference IQA techniques, since in seismic images we do not have a reference, i.e., most of the time we deal with imaging data of new explored areas.

Many IQA techniques that are available from the literature compute different kinds of distortion effects [19, 20]. These methods obviously are limited by the fact that, we need to know the type of distortion available in the images. Thus, a general purpose algorithm, which trains and learns by itself from the details of the images provided, is an emerging research direction. In seismic IQA, we are looking for a similar type of algorithm that is, firstly, independent of the distortion type and secondly, it should be for a general purpose use. In the literature, a couple of similar type of algorithms were proposed for natural scene images, which does IQA based on spectral and spatial entropies (SSEQ) and curvelet features, respectively, and are independent of distortion type [19, 20]. We will investigate such techniques that are reported in the literature for the application of seismic images by considering only two important indicators, namely, noise and spatial resolution (or how much smooth) the seismic images are.

4.2 Non-reference Quality Assessment based on Spatial and Spectral Entropies (SSEQ)

Image spatial entropy, as the name indicates, is the amount of information contained within the image when computed over a multi-scales reveals the statistical entropy of the scale space [19]. The local entropy of the image is affected by the types and degree of distortions. The global image entropy calculates the global information of images but do not discriminate the spatial distribution of information. Thus images might have the same global entropy values yet they might appear different.

In this method, entropies are computed and utilized from the local seismic image blocks, in both block spatial scale and block spectral scale. Spatial entropy is a function of the probability distribution of the local seismic amplitude values, while spectral entropy is a function of the probability distribution of the local discrete cosine transform (DCT) coefficient values. This entropy based method analyzes the joint distribution of seismic image sample values within a local patch.

This reflects that the statistical characteristics of the local regions rather than seismic image sample values, which will contribute to describe the images local structural information.

Figure 4.1 shows a block diagram of how feature vector is extracted in SSEQ method:

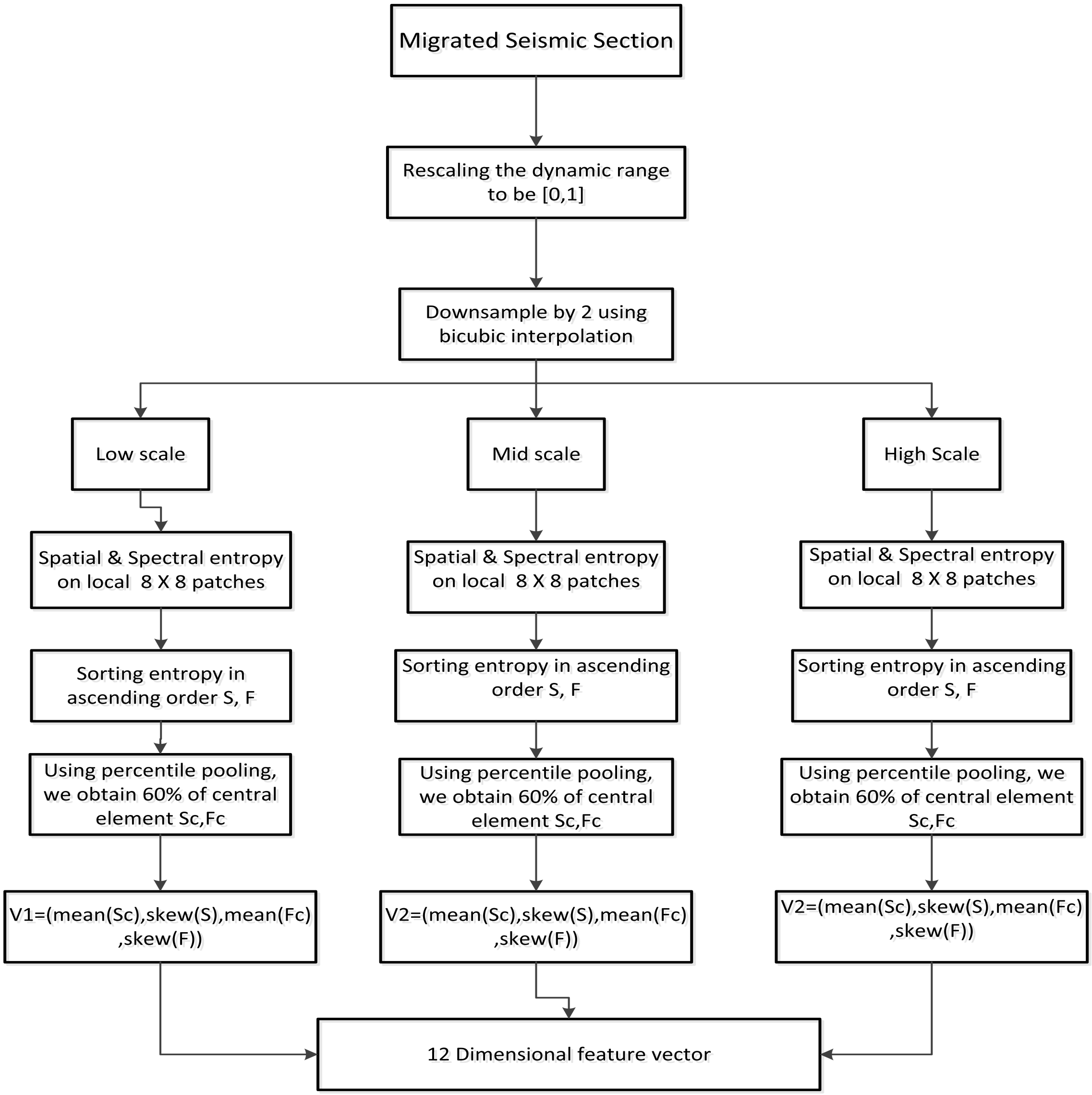

Figure 4.1: Block diagram showing feature extraction using spatial and spectral entropies.

The basic hypothesis is that the local entropy of undistorted seismic images have certain statistical properties. These statistical properties are because of the dependence between adjacent seismic amplitude values. Hence, with the introduction of distortion, will create disturbance in the local entropy.

Below is the description on how local entropy is evaluated and the relationship between the local entropy and seismic image quality.

4.2.1 Spatial Entropy

The spatial entropy is calculated by the formula [19] :

$$E_s = -\sum_{x} p\left(x\right) \log_2 p\left(x\right), \tag{4.1}$$

where x is the sample amplitude values with in the block, with empirical probability density $p(x)$. To illustrate the behavior of local spatial entropy values against distortion, a series of entropy plots are plotted for various seismic images. It has been noticed that, the undistorted image (in our case image with better resolution) is left-skewed. The left-skewed means that there is less data on the left of the mean value than right, yielding to a longer left tail. However, introduction of distortion changes mean and skew the histogram to the right. We have performed this on 4 migrated sections - see Figure 4.2.

Figure 4.3 shows the histograms of spatial entropy values of the images in Figure 4.2. It can be seen that the behavior of Taylor [54] is completely different from that of other three plots, i.e., the POCS [35], PSPI [6] and Lemke25 [55]. We

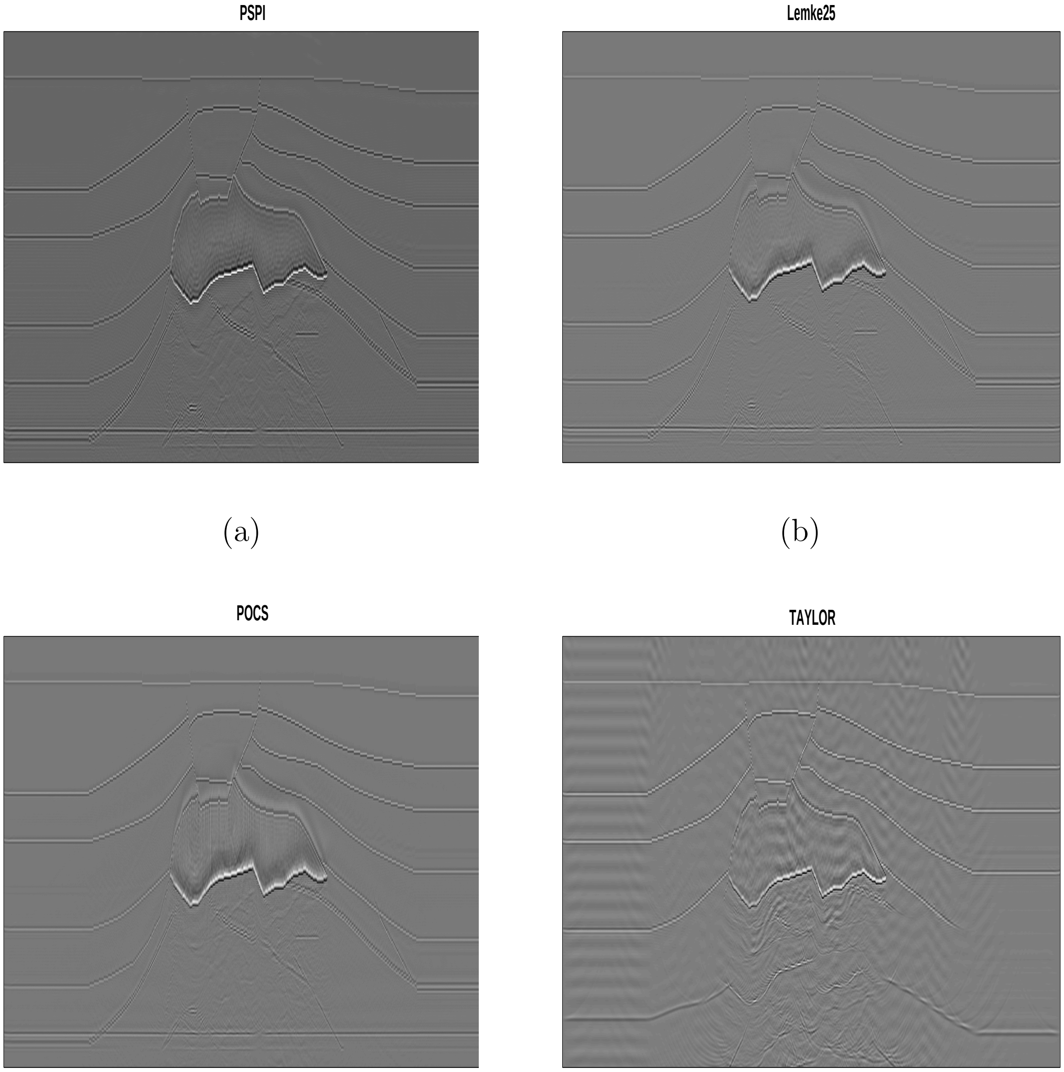

(a) (b)

(c) (d)

Figure 4.2: (a) The poststack PSPI image scaled between 0-1. (b) The poststack Lemke image with 25 coefficients scaled between 0-1. (c) The poststack POCS image scaled between 0-1. (d) The poststack Taylor image scaled between 0-1.

note these changes in the behavior of the spatial entropy and utilize the mean and skew as the quality features that describe the histogram. From 4.3 it is clearly visible that the graph of Taylor is completely different when compared with the rest of the techniques.

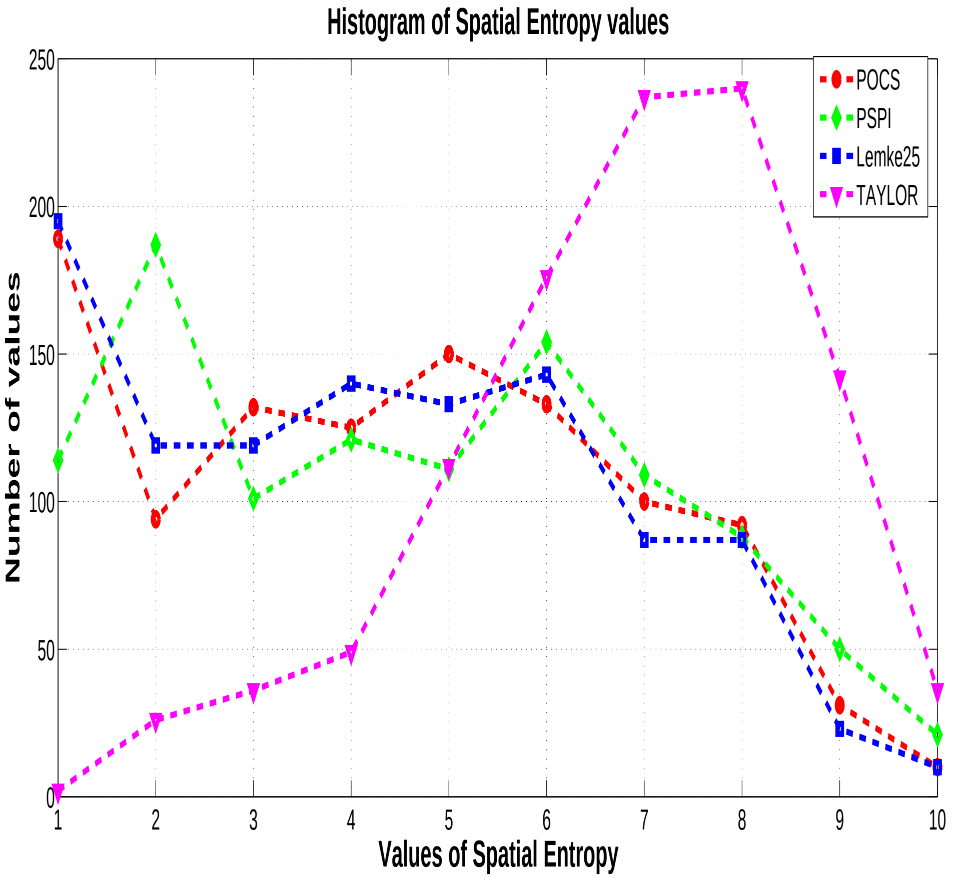

Figure 4.3: Histograms of spectral entropy values.

4.2.2 Spectral Entropy

As explained earlier, that there exists a strong relationship between spatial entropy values and the seismic image sample values. In spectral entropy, there exists a strong relationship between spectral entropy values and the degree of distortion, the block DCT coefficient matrix is computed on 8 × 8 blocks [19]. Use of DCT rather than Discrete Fourier transform (DFT) reduces the block edge energy in the transform coefficients [19].

The local spectral entropy is defined as:

$$E_f = -\sum_i \sum_j P\left(i,j\right) \log_2 P\left(i,j\right). \tag{4.2}$$

Note that i, j here stands for the sample amplitude values of seismic images.

Like the case of spatial entropy, a series of experiments were conducted on spectral entropy and their histograms were plotted for different images. Figure 4.4 shows the plot of histogram of spectral entropy values. Clearly, it can be observed that the undistorted seismic image (in our case, the seismic image with better resolution) has a spectral entropy histogram typically left skewed. However, introduction of noise changes its mean and skew to the right. The spectral entropy features are strongly indicative of the distortions, compared with the spatial entropy histogram. The spectral entropy histogram more clearly distinguishes the undistorted image from those affected by distortions. The spectral entropy defined here is an accurate descriptor of images energy spectrum and emphasizes the main frequency and main orientations within a local patch. So one can be able to distinguish noise and smoothness effect more clearly. Further, spectral entropy can capture texture variations more effectively, to which human perception is very sensitive.

4.2.3 Two-stage framework for blind image quality assessment

The non-reference IQA method proposed here uses the two-stage framework to map feature vectors to predicted quality scores. Thus, a probabilistic classifier

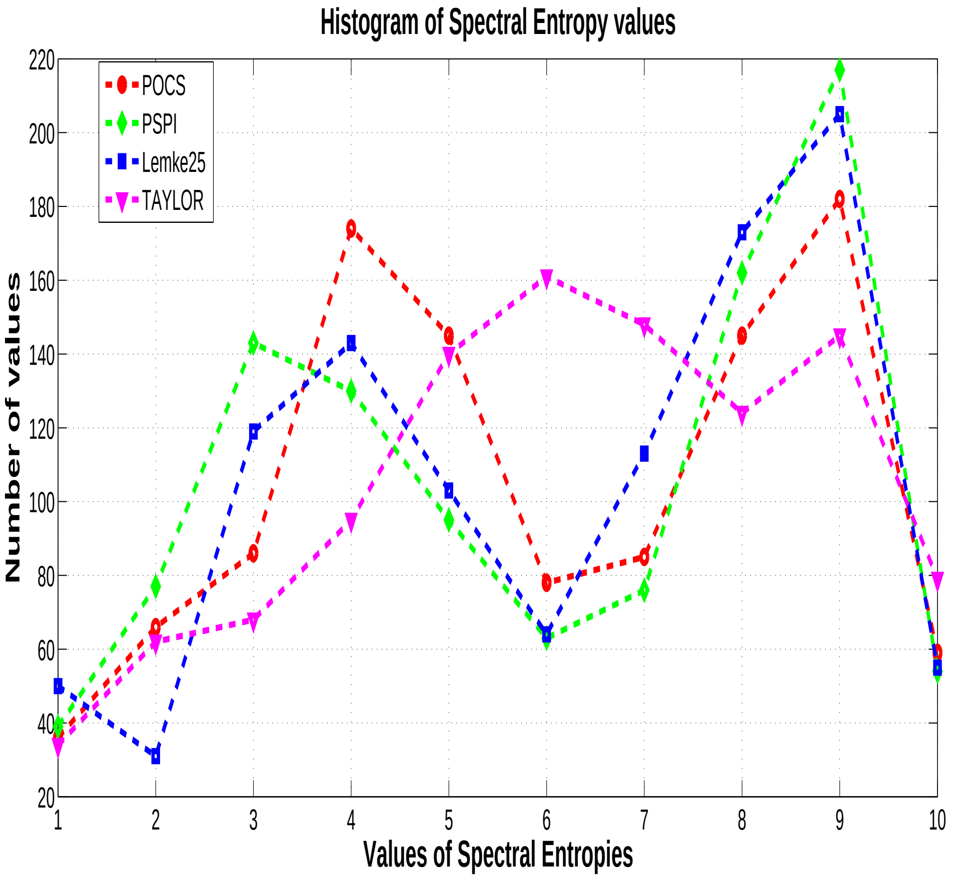

Figure 4.4: Plot showing histogram of spectral entropy values.

is trained to compute the probability of occurrence of each distortion in an image, i.e., the smoothness of seismic image and the noise they contain and then regression functions that are trained on each distortion type against human scores that are available from LIBSVM package[1] are used [56]. This yields two vectors: the distortion probability vector and the distortion-specific quality vector. A final predicted quality score is obtained by computing the dot product of these 2 vectors. Machine learning has been applied in the field of IQA for a long time, such as support vector regression (SVR) [57] and neural network [56].We use support vector machines (SVM) for classification to obtain distortion probability vector and SVR for regression [58, 59], which provides the distortion-specific quality vector. We used the LIBSVM package [57] to implement the SVM and SVR, both implemented using the radial basis function (RBF) kernel. Figure 4.5 shows the flow chart for obtaining the quality score. There are three important functions used from the LIBSVM tool, the first one is the SVMtrain, which is used to train the training dataset, next we have used the svmpredict function which predicts the probability of noise and smoothness contained in an seismic image. Finally, we used the SVR model from LIBSVM, which consists of quality score of distorted images based on human scores. Once we obtain the probability and the quality score based on human scores we obtain the quality metric using :

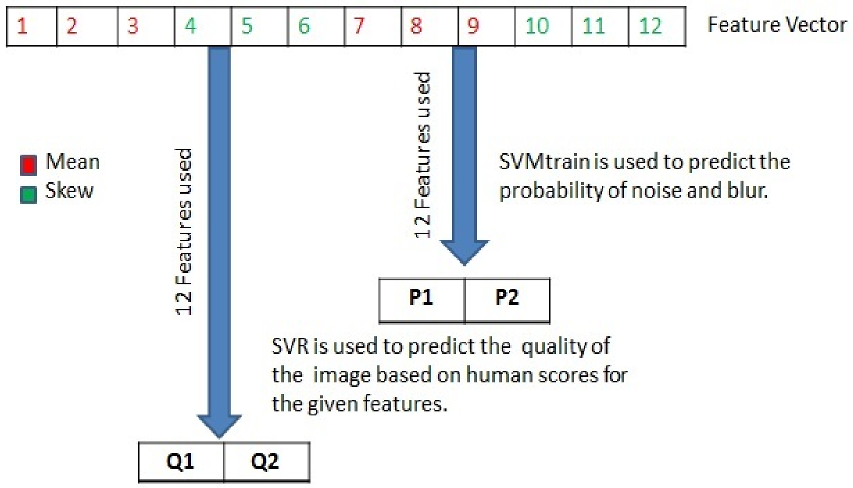

Figure 4.5: Block diagram showing quality score obtained from spatial and spectral features.

$$Quality\ \ metric = \sum_{i=1}^{2} P_i Q_i. \tag{4.3}$$

The most crucial task in seismic IQA is to obtain images in order to create the dataset for training and testing. The SEG/EAGE standard velocity model and the zero-offset section is used to obtain images from various techniques. Using various poststack imaging techniques 20 sample images were obtained (see Table 4.1) out of which 16 were used for training and 4 were used for testing. The images that are obtained from various techniques are shown in the Appendix (See appendix after chapter 5).

	Sample Seismic Image	Technique	Classification Subjectively
Training	1	F-X [23]	Good
	2	SPLITSTEP [10]	Not Good
	3	Non-sparse L1 25-coeffecients[39]	Not Good
	4	Non-sparse L1 35-coeffecients [39]	Good
	5	Sparse L1 25-coeffecients [39]	Not Good
	6	Sparse L1 35-coeffecients [39]	Good
	7	Sparse POCS [35]	Good
	8	Fisher 25-coefficients [55]	Good
	9	Fisher 35-coefficients [55]	Not Good
	10	Lemke 35-coeffecients [55]	Good
	11	L1-weighted 35-coefficients [55]	Good
	12	L1-weighted 25-coefficients [55]	Not Good
	13	L1-nonweighted 25-coefficients	Not Good
	14	L1-nonweighted 35-coefficients	Good
	15	Gazdag [6]	Not Good
	16	Generalised screen [34]	Good
Testing	17	PSPI [6]	Good
	18	Lemke 25-coefficients [55]	Good
	19	POCS [35]	Good
	20	TAYLOR [54]	Not Good

Table 4.1: Subjective classification of various poststack images.

4.2.4 Quality metric for various imaging techniques using SSEQ

The range of the quality metric is between 0-100, where 0 represents good quality of an image and 100 represents the bad quality of image. Figure 4.6 shows the quality score obtained for various seismic images based on spatial and spectral entropy (SSEQ) features. Obviously, the PSPI comes out to with the lowest IQA value, which is reflecting the subjective assessment, as PSPI image is considered to be the most accurate image.

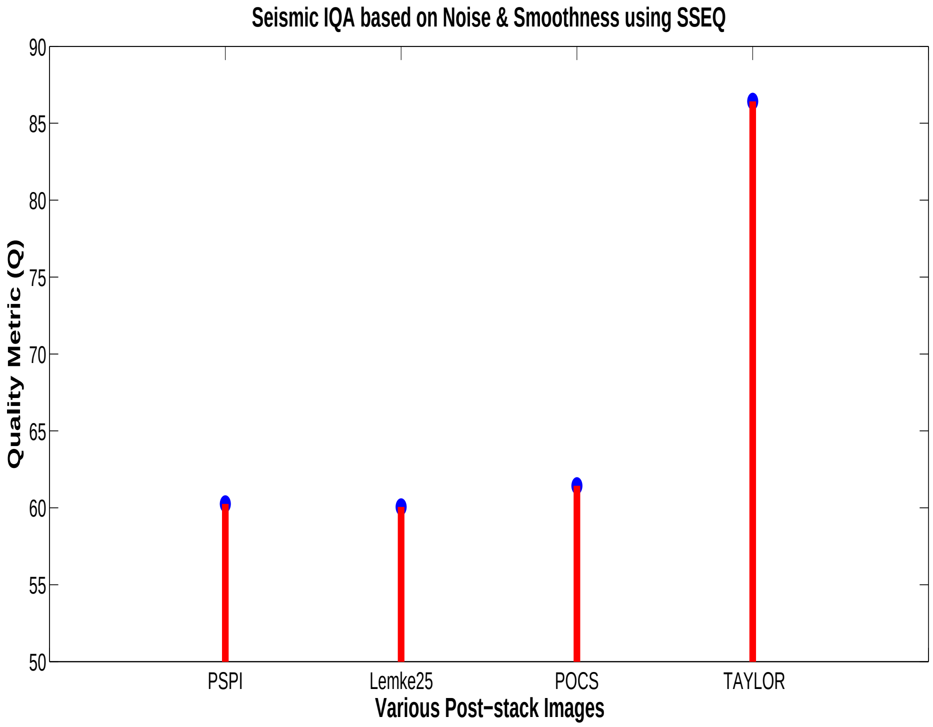

Figure 4.6: Quality Metric from various poststack images using spatial and spectral features.

4.3 Non-reference Quality Assessment based on Curvelets

Instead of using spatial and spectral features to assess the quality of seismic images, we tested it with the curvelet features. The curvelet transform is basically multidimensional [20]. Each curvelet has an approximately elliptical support, and is smooth along the major axis and oscillatory along the major axis [20]. A seismic image curvelet coefficient may be interpreted as the result of convolution of the associated curvelet with the seismic image. If a curvelet of given scale, angle, and location is approximately aligned along some curve in the image, its curvelet coefficient will be large. Otherwise, it will tend to be small. The discrete curvelet transform of a 2-D discrete $f(x_1, x_2)$ is given as follows [20]:

$$\theta\left(j,k,l\right) = \sum_{0 \leq x_1, x_2 < n} f\left[x_1, x_2\right] \overline{\varphi_{j,k,l}\left[x_1, x_2\right]}, \tag{4.4}$$

where $\varphi_{j,k,l}$ is a curvelet of scale j at position index k with index angle l,x_1, x_2 denotes coordinates in spatial domain.

Using the curvelet transform scalar division principle [nscales $= log_2(n) - 3$ where n is the size of input seismic image], each 256×256 block may be transformed into 5 layers of curvelet coefficients over 5 different scales. Image distortions often affect the high frequency components of an image, e.g., smoothness attenuates the high frequencies while noise may increase them. Usually, low frequency components are less affected. So we only consider the curvelet coefficients at finer scales in our model. In order to capture the distribution characters of coefficients with larger amplitude more effectively, we calculate the empirical probability distribution function (PDF) of the logarithm (base 10) of the magnitude of the curvelet coefficients at scale j:

$$h_j\left(x\right) = pdf\left(\log_{10}\left(\left|\theta_j\right|\right)\right), \tag{4.5}$$

where θ_j is set of curvelet coefficients at scale j.

Figure 4.7 shows the block diagram of how the curvelet feature vector is extracted.

Figure 4.7: Block diagram showing feature extraction using curvelet features.

4.3.1 The curvelet features

We use asymmetric generalized Gaussian distribution (AGGD) to fitting the curve obtain from h_j. We use the curve fitting parameters amplitude (a) mean (μ) and standard deviations (σ_l, σ_r) as the first four features of our feature vector.

The curvelet transform is a rich source of orientation information on images and their distortions. The seismic image distortion process can modify the orientation energy distribution in an unnatural manner. Therefore, we study the oriental energy distribution (OED) of input image by calculation the mean of the curvelet coefficients:

$$E_l = E\left(|\theta_l|\right), \tag{4.6}$$

where $E(x)$ is the sample mean of x and θ_l is a set of coefficients of the orientation matrix with orientation index l. The cardinal peaks of the OED has significant impact on the image. These are very badly effected in case of distortion. In order to capture this, we use kurtosis and take the mean between different layers also the image distortion process affects the anisotropy therefore we consider the coefficient of variation in order to capture this effect. These two features mean kurtosis and coefficient of variation are taken as two samples in our feature vector to capture the effect of orientation energy distribution due to distorted images.

The coefficient of variation is calculated as follows:

$$Cv = \sigma_{so}/\mu_{so}, \tag{4.7}$$

where μ_{so} and σ_{so} are the sample mean and standard deviation of the non-cardinal orientation energies. Here, Cv is used to capture the degree of anisotropy of the image, and is used as a quality feature.

After taking into consideration OED we move to the scalar energy distribution which modify the energy spectrum of the image in a very unnatural manner. In order to take this effect into consideration we calculate the energy differences between the adjacent layers and interval layers:

$$e_j = E\left(\log_{10}\left(|\theta_j|\right)\right), \qquad j = 1, 2.., 5 \tag{4.8}$$

where θ_j is the set of coefficients of the scale matrix set where scale index is j.

We obtain six features $d_1 = e_5 - e_4, d_2 = e_4 - e_3, d_3 = e_3 - e_2, d_4 = e_2 - e_1, d_5 = e_5 - e_3, d_6 = e_4 - e_2$, from Eq. (4.8), thereby, making our feature vector 12 dimensional. Figure(4.8) shows the flow chart to obtaining the quality score using curvelet features.

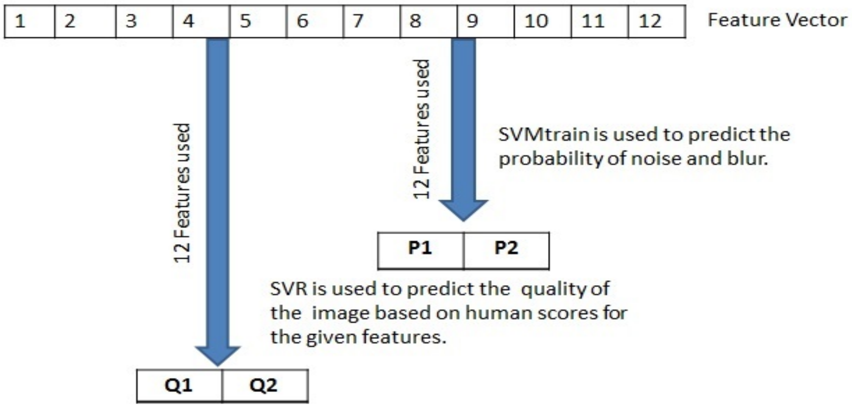

Figure 4.8: Block diagram showing quality score obtained using curvelet features.

The 12 dimensional feature vector that is obtained from each image is then divided into two classes and then into training and testing data sets. We utilize the same LIBSVM package used earlier in SSEQ to train and test the same data set mentioned in section 4.2.1.

4.3.2 Quality metric for various imaging techniques using curvelet features

The range of the quality metric is between 0-100, where 0 represents good quality of an image and 100 represents the bad quality of image. Figure 4.6 shows the quality score obtained for various seismic images based on curvelet features.

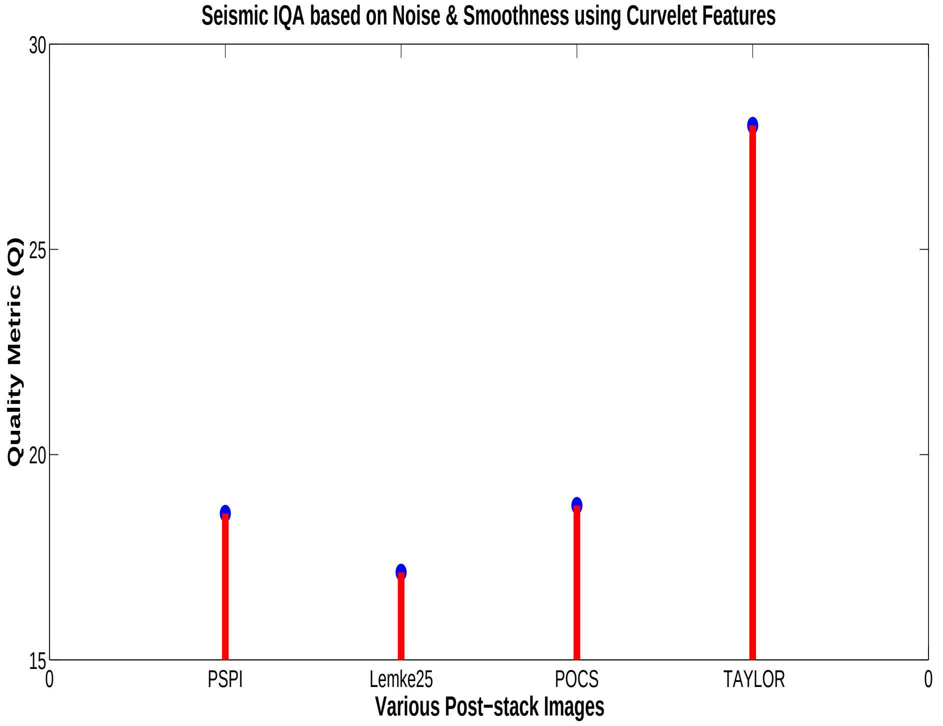

Figure 4.9: Quality Metric from various poststack images using curvelet features.

4.4 Summary

An attempt was made to utilize the general-purpose non-reference image quality assessment (IQA) methods in the field of seismic imaging which utilizes spatial and spectral features and curvelet features to determine the quality of an image. We found that SSEQ and curvelet delivers quality prediction performance that correlates with the human vision system. From 4.6 and Figure 4.9 it can be noted that, the average of the first three quality metric in case of SSEQ is 29.901 % less when compared to the last sample and in case of curvelet this relative percentage is around 35.2126 %. Hence, from this we might conclude that the curvelet features may be better candidates for IQA of seismic images.

CHAPTER 5

CONCLUSIONS

In this research work, the problem of absorption in seismic wave propagation is considered and solved using a technique called Phase Shift plus Interpolation (PSPI). The PSPI technique was first applied on the benchmark 2D SEG/EAGE dataset and the results were shown to be very crisp and accurate. Later, we performed prestack migration using another standard dataset known as Marmousi data. This algorithm was then tested for the case of absorption. The results obtained, in this case, were of low resolution. In order to avoid such a problem, the PSPI algorithm was modified to compensate for the effect of absorption by introducing a parameter called the Q-factor in the extrapolator term. This would compensate for the propagating wave in both directions, i.e., upwards and downwards, when the wave looses its amplitude and changes its frequency contents.

Once the imaging was done, another important aspect of seismic imaging, i.e., the quality of the images that are obtained was taken into consideration and general purpose non-reference based algorithms were applied on the various poststack seismic images obtained. The algorithms that were used to perform this quality assessment were spatial and spectral entropy quality (SSEQ) metric and assessment based on curvelet features. The quality score obtained in both the techniques matches very closely with the human perception by taking into consideration the noise and blur (smoothness) in an image.

5.1 Future work and Suggestions

This work can be extended for a 3-D model without any limitations. The wavefield extrapolation for the absorption case has cut-offs which are different from the acoustic case. These extrapolators can be modified in the filtering process in acoustic medium and can be used to compensate while doing migration by filters in visco-acoustic medium. Furthermore, the visco-acoustic PSPI technique can be applied on visco-elastic or elastic medium by considering the elastic parameters.

As the computational complexity and time required for PSPI technique is very high in case of prestack imaging. It is possible that it can be reduced with few modification such as changing multiplications in the loops to additions while depth imaging. Hence, reducing the time required to computation. Moreover in seismic IQA, if one can attain the features considering sharpness in an image then this quality assessment can be performed based on sharpness rather than on smoothness(blur).

APPENDIX

The following are the images that were used for training using the support vector machine.

F-X

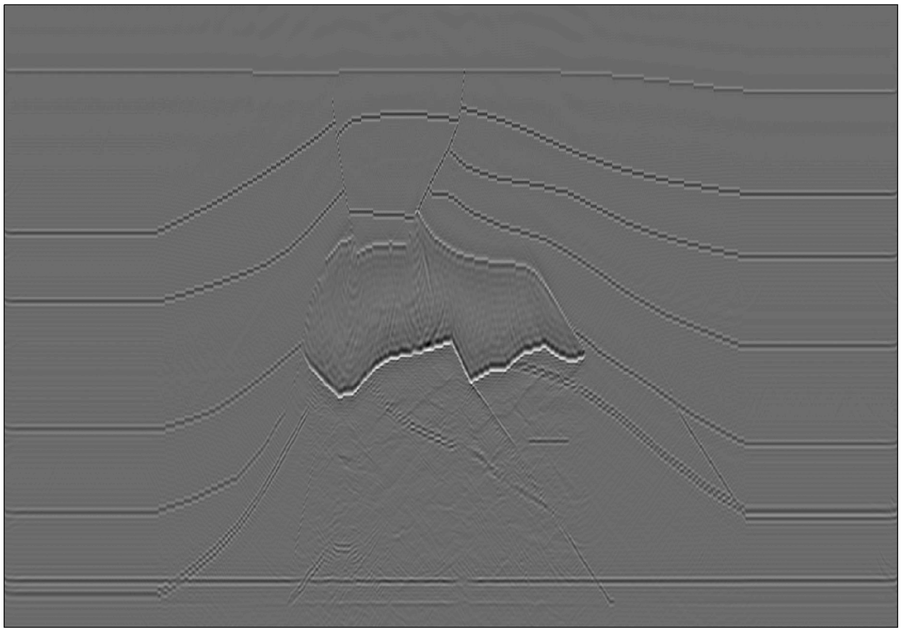

Post-stack result obtained using F-X imaging technique.

SPLITSTEP

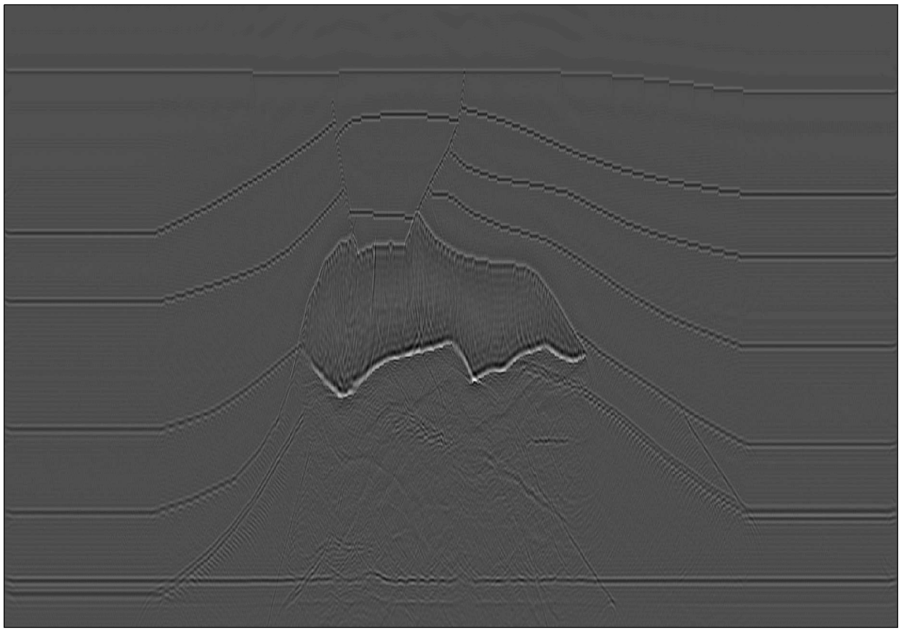

Post-stack result obtained using SPLIT-STEP imaging technique.

Nonsparse L1-25 coefficients

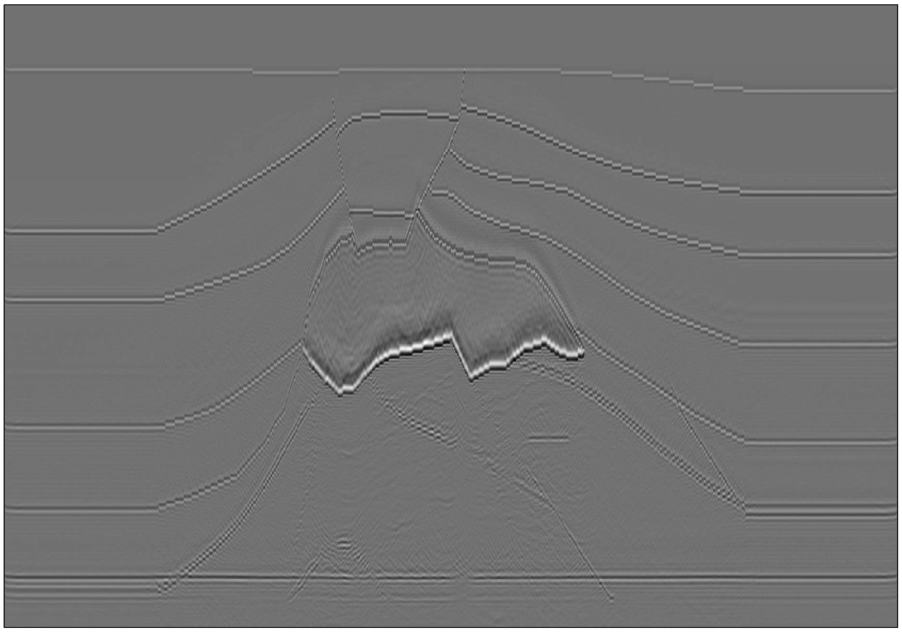

Post-stack result obtained using Non-sparse L1 norm (25 coefficients) imaging technique.

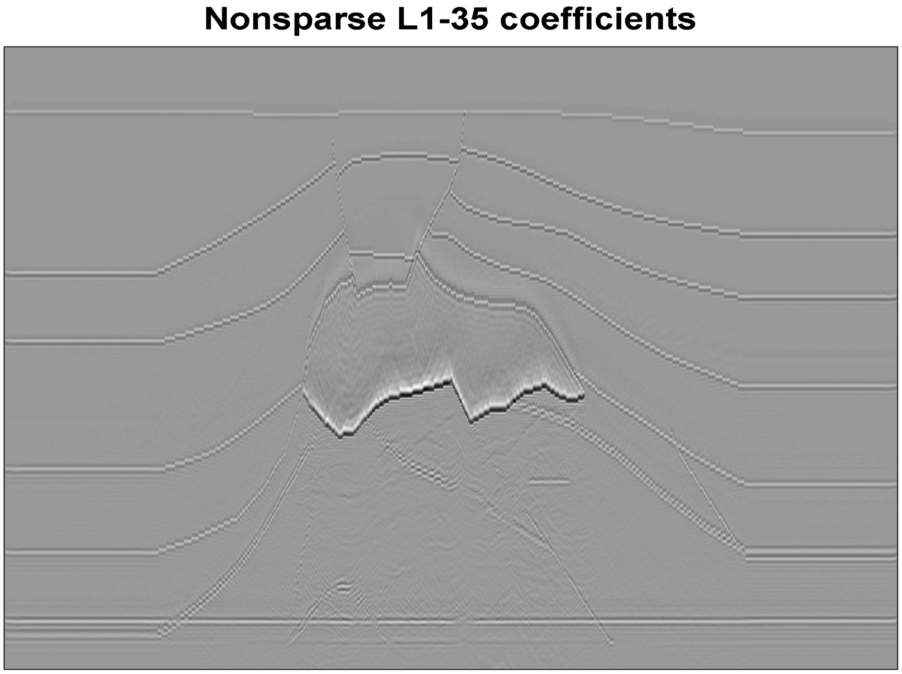

Nonsparse L1-35 coefficients

Post-stack result obtained using Non-sparse L1 norm (35 coefficients) imaging technique.

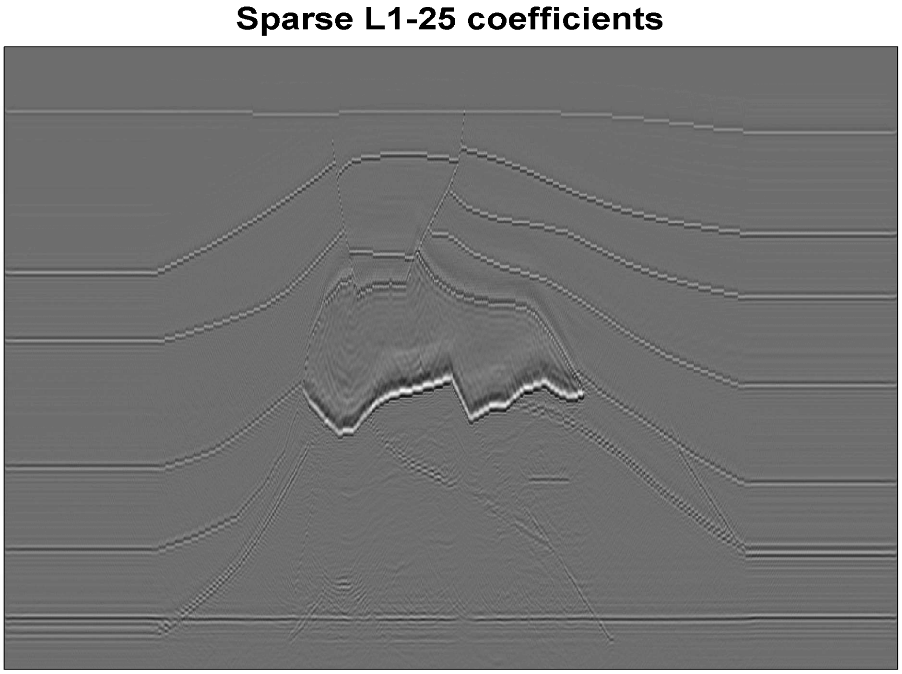

Sparse L1-25 coefficients

Post-stack result obtained using Sparse L1 norm (25 coefficients) imaging technique.

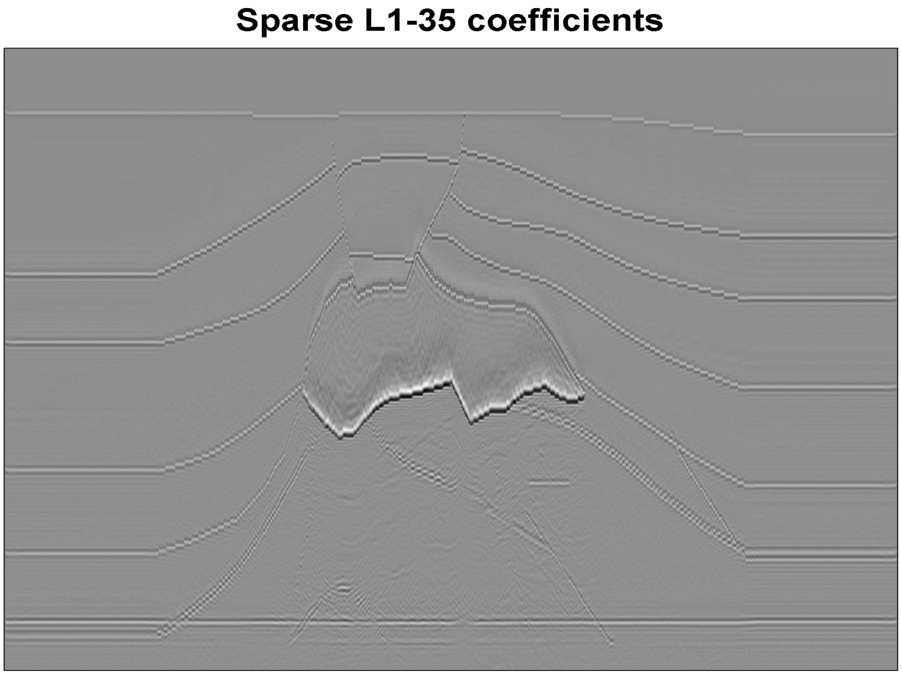

Sparse L1-35 coefficients

Post-stack result obtained using Sparse L1 norm (35 coefficients) imaging technique.

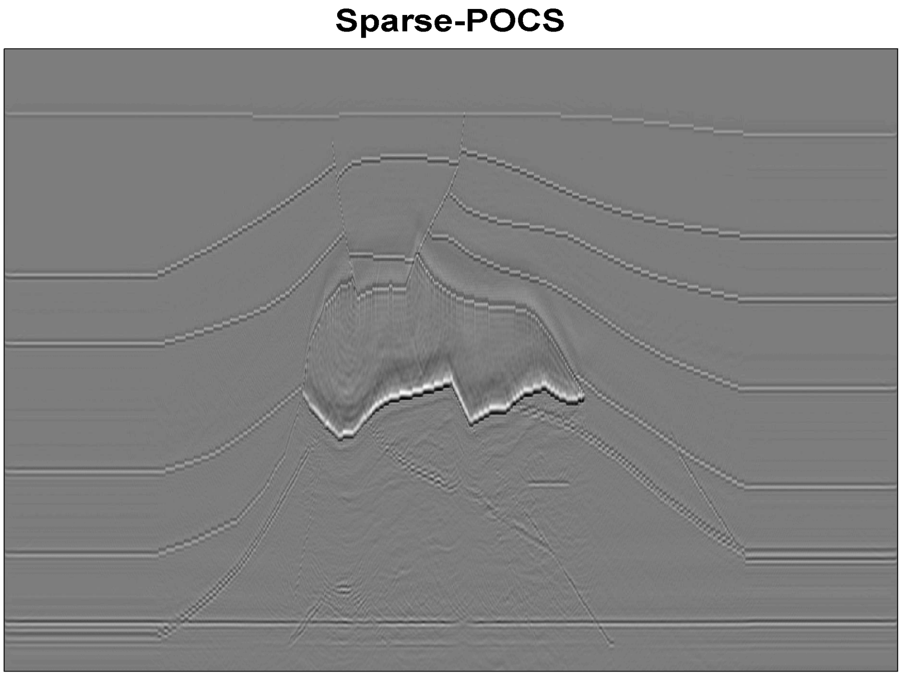

Sparse-POCS

Post-stack result obtained using Sparse-POCS imaging technique.

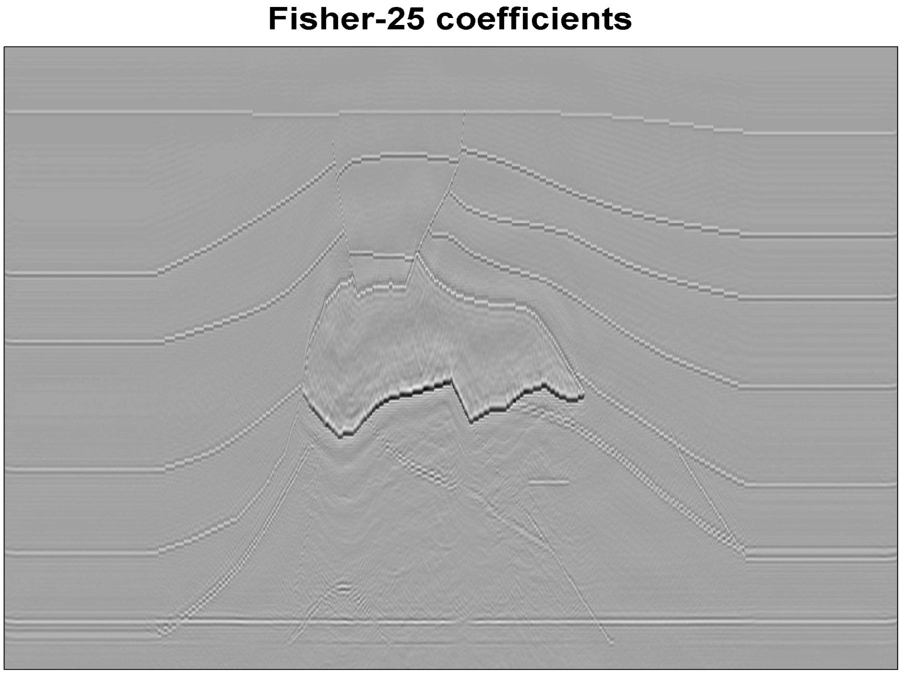

Fisher-25 coefficients

Post-stack result obtained using Fisher (25 coefficients) imaging technique.

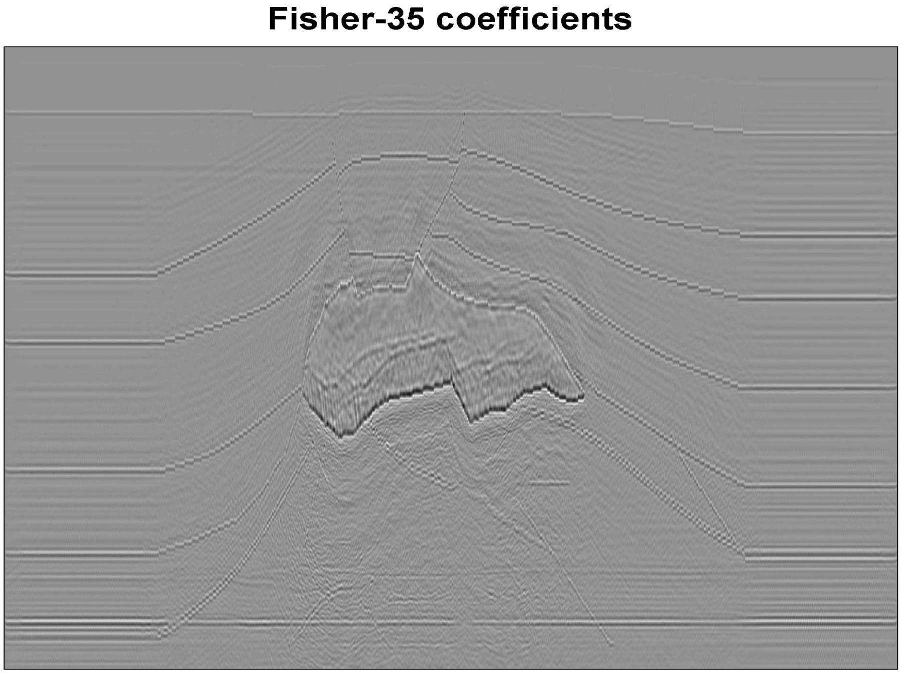

Fisher-35 coefficients

Post-stack result obtained using Fisher (35 coefficients) imaging technique.

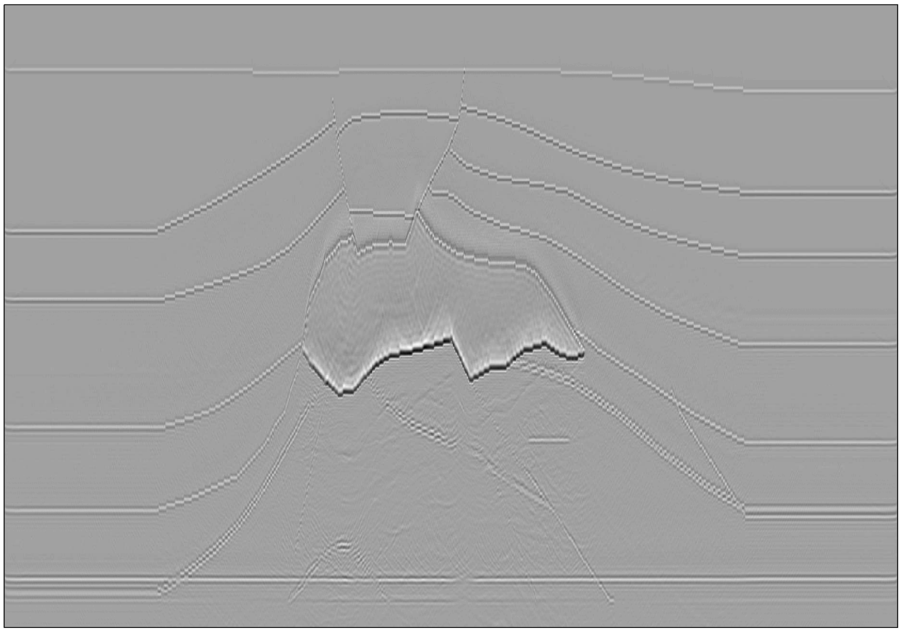

Lemke-35 coefficients

Post-stack result obtained using Lemke(25 coefficients) imaging technique.

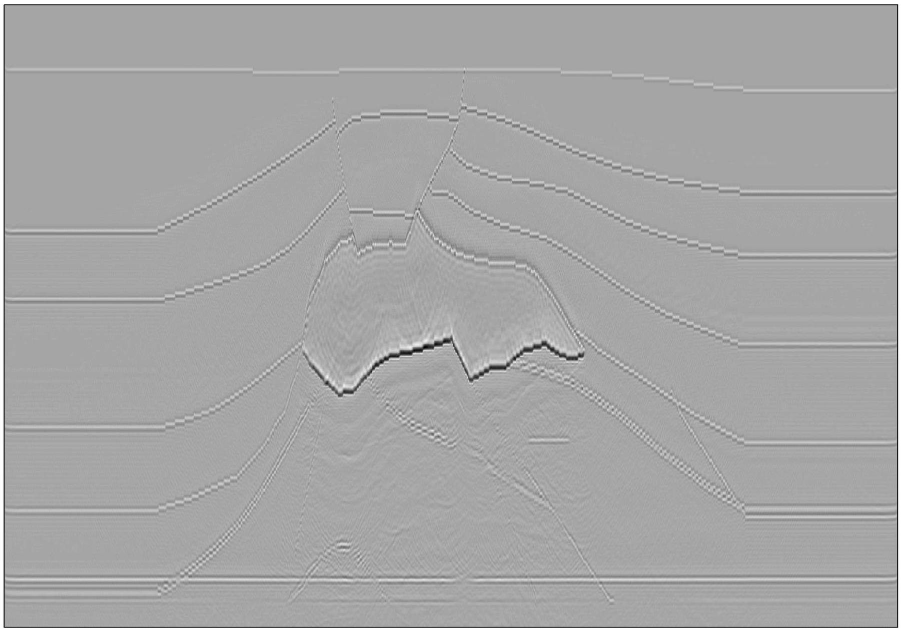

L1 Weighted-25 coefficients

Post-stack result obtained using L1-weighted (25 coefficients) imaging technique.

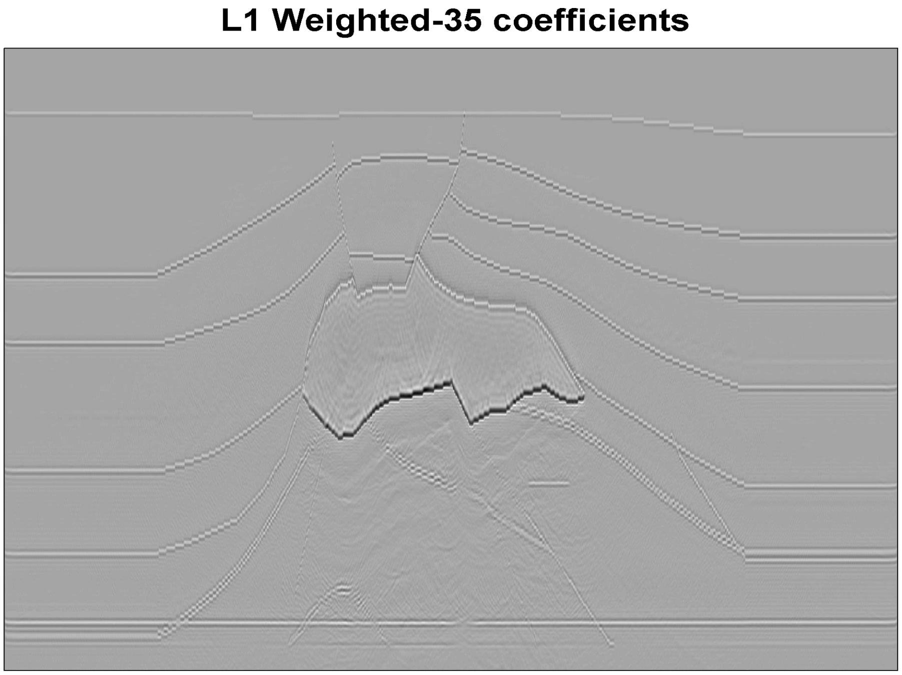

Post-stack result obtained using L1-weighted (35 coefficients) imaging technique.

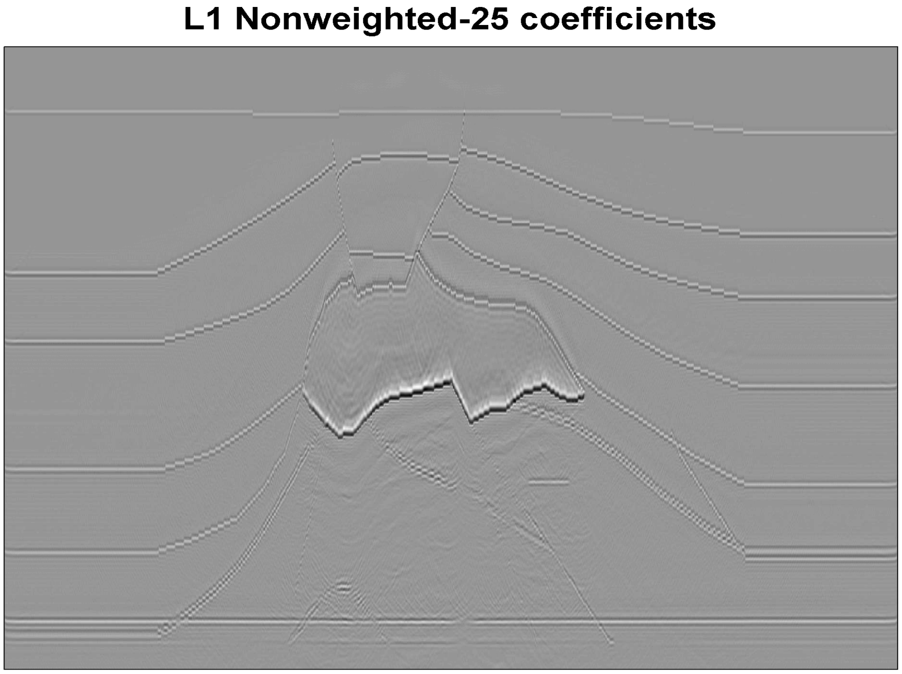

Post-stack result obtained using L1-non-weighted (25 coefficients) imaging technique.

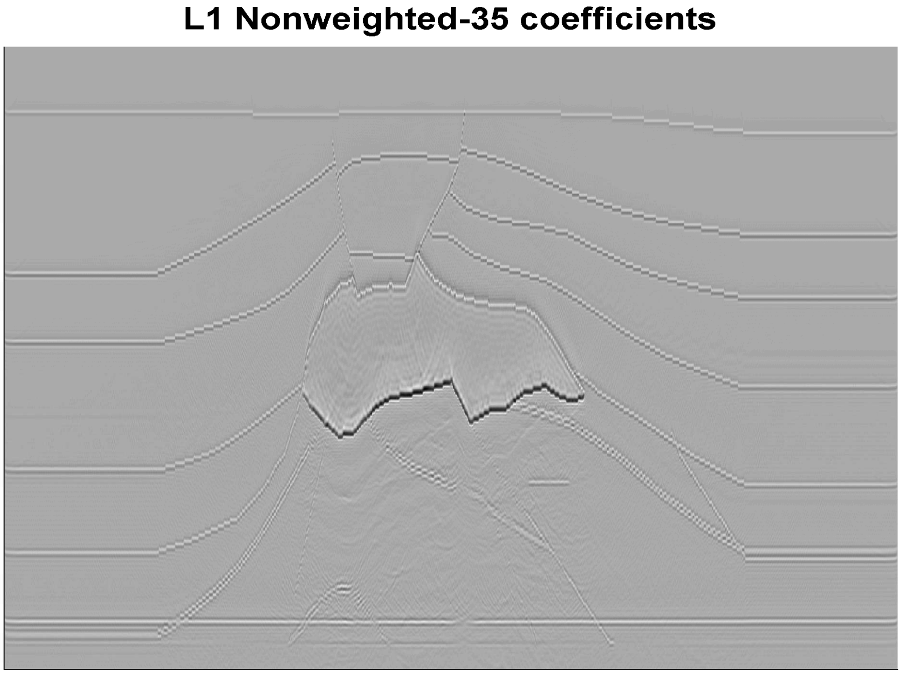

L1 Nonweighted-35 coefficients

Post-stack result obtained using L1-nonweighted (35 coefficients) imaging technique.

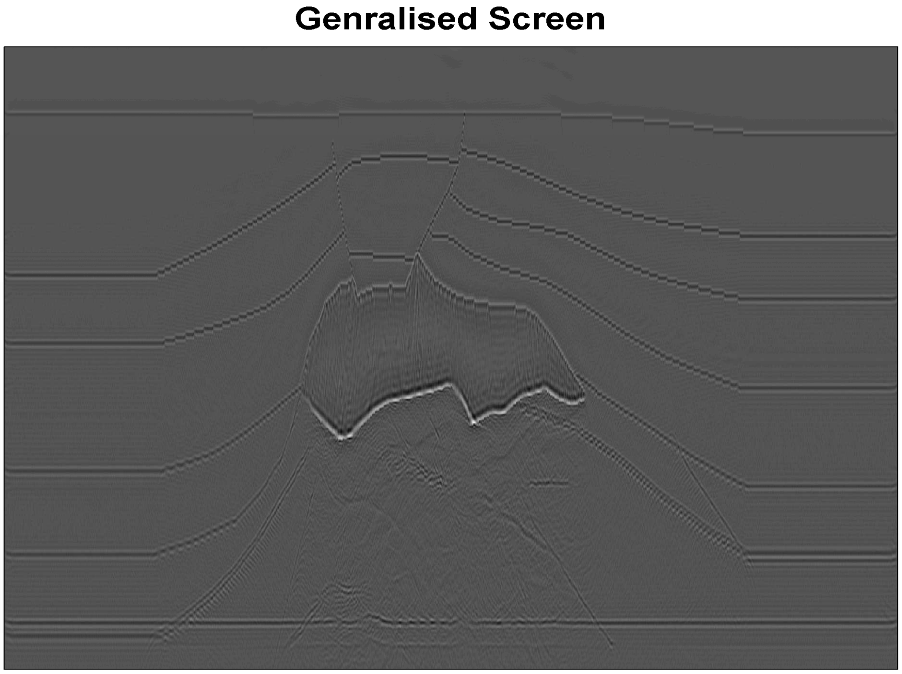

Genralised Screen

Post-stack result obtained using Generalised Screen imaging technique.

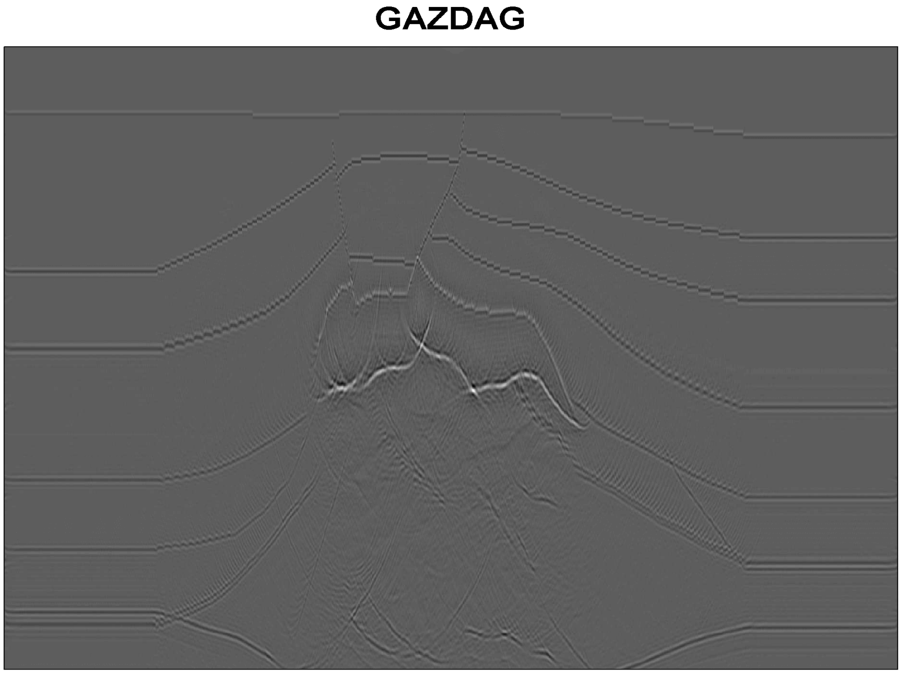

Post-stack result obtained using GAZDAG imaging technique.

REFERENCES

[1] J. Bee Bednar, “Modeling, Migration and Velocity Analysis in Simple and Complex Structure,” p. 392, 2009. [Online]. Available: http://www.panoramatech.com

[2] P. Reddy, “Historical Development of Seismic Imaging TechniqueAn Overview,” *J. Ind. Geophys. Union*, vol. 16, no. 3, pp. 71–86, 2012. [Online]. Available: http://www.igu.in/16-3/review paper.pdf

[3] G. Schuster, “Basics of Seismic Imaging,” no. Isbn 9780521871242, 2010. [Online]. Available: http://csim.kaust.edu.sa/files/short.courses/seismicimage.pdf

[4] J. C. Bancroft, “Review of seismic imaging : Prestack,” *CSEG National Convention*, vol. 13, no. November, pp. 551–571, 2001.

[5] R. Ferguson and G. Margrave, “Planned seismic imaging using explicit one-way operators,” *Geophysics*, vol. 70, no. 5, pp. 101–109, 2005. [Online]. Available: http://library.seg.org/doi/abs/10.1190/1.2073885

[6] J. Gazdag and P. Sguazzero, “Migration of seismic data by phase shift plus interpolation k :,” *Geophysics*, vol. 49, no. 2, pp. 124–131, 1984.

[7] A. Popovici, “Prestack migration by split-step DSR,” *Geophysics*, vol. 61, no. 5, pp. 1412–1416, 1996. [Online]. Available: http://library.seg.org/doi/abs/10.1190/1.1444065

[8] P. Sava and S. Hill, “Overview and classification of wavefield seismic imaging methods,” *The Leading Edge*, pp. 1–9, 2009. [Online]. Available: http://library.seg.org/doi/abs/10.1190/1.3086052

[9] ProMax, “Stolt or Phase Shift 3D Migration,” pp. 727–742.

[10] A. J. Berkhout, “Wave field extrapolation techniques in seismic migration, a tutorial,” Feb. 2012. [Online]. Available: http://library.seg.org/doi/abs/10.1190/1.1441172

[11] H. Wang, “Seismic wave imaging in visco-acoustic media,” *Science in China Series A*, vol. 47, no. 7, p. 146, 2004. [Online]. Available: http://www.scichina.com/2004/yk/ya/yazk/yazk0146.stm

[12] N. Dai and G. F. West, “Inverse Q migration,” *SEG Technical Program Expanded Abstracts 2009*, no. 4, pp. 1418–1421, 1979.

[13] S. Jang and Y.-w. Kim, “Prestack depth migration by 3D PSPI,” *Proceedings of the 10th SEGJ International . . .*, no. 1, pp. 35–38, 2011. [Online]. Available: http://library.seg.org/doi/abs/10.1190/segj102011-001.9

[14] S. H. Gray and J. Etgen, *Seismic migration problems and solutions.*

[15] M. Reshef and D. Kosloff, "Migration of commonshot gathers," *Geophysics*, vol. 51, no. 2, pp. 324–331, Feb. 1986. [Online]. Available: http://library.seg.org/doi/abs/10.1190/1.1442091

[16] H. Sheikh, M. Sabir, and A. Bovik, "A statistical evaluation of recent full reference image quality assessment algorithms," *Image Processing, IEEE*, vol. 15, no. 11, pp. 3441–3452, 2006. [Online]. Available: http://ieeexplore.ieee.org/xpls/abs_all.jsp?arnumber=1709988

[17] Z. Wang and A. Bovik, "Image quality assessment: from error visibility to structural similarity," *. . . , IEEE Transactions on*, vol. 13, no. 4, pp. 600–612, 2004. [Online]. Available: http://ieeexplore.ieee.org/xpls/abs_all.jsp?arnumber=1284395

[18] Z. Wang, E. Simoncelli, and A. Bovik, "Multiscale structural similarity for image quality assessment," *Signals, Systems and . . .* , vol. 2, no. Ki L, pp. 1398–1402, 2003. [Online]. Available: http://ieeexplore.ieee.org/xpls/abs_all.jsp?arnumber=1292216

[19] L. Liu, B. Liu, H. Huang, and A. C. Bovik, "No-reference image quality assessment based on spatial and spectral entropies," *Signal Processing: Image Communication*, vol. 29, no. 8, pp. 856–863, Sep. 2014. [Online]. Available: http://linkinghub.elsevier.com/retrieve/pii/S0923596514000927

[20] L. Liu, H. Dong, H. Huang, and A. C. Bovik, "No-reference image quality assessment in curvelet domain," *Signal Processing: Image Communication*, vol. 29, no. 4, pp. 494–505, Apr. 2014. [Online]. Available: http://linkinghub.elsevier.com/retrieve/pii/S0923596514000496

[21] J. Attanayake, "Seismic Migration," no. November, 2006.

[22] J. Etgen, "T., 1984, Stability of explicit depth extrapolation through laterally-varying media: 64th Ann," *Internat. Mtg, Soc. Expl. Geophys., Expanded Abstracts*, vol. 2.

[23] R. J. Ferguson and G. F. Margrave, "Explicit Fourier wavefield operators," *Geophysical Journal International*, vol. 165, no. 1, pp. 259–271, Apr. 2006. [Online]. Available: http://gji.oxfordjournals.org/cgi/doi/10.1111/j.1365-246X.2006.02888.x

[24] A. Koduru and P. Mohanty, "Comparison of wave equation migration techniques over complex geological structures," *J. Ind. Geophys. Union (July 2013)*, vol. 17, no. 3, pp. 281–288, 2013. [Online]. Available: http://www.igu.in/17-3/paper-5.pdf

[25] S. Phadke, D. Bhardwaj, and S. Yerneni, "Wave equation based migration and modelling algorithms on parallel computers," *Proc. of SPG (Society of Petroleum Geophysics*, p. 5, 1998. [Online]. Available: http://196.1.113.24/html/pdf/spg_1.pdf

[26] F. Liu, S. A. Morton, J. P. Leveille, and G. Zhang, "Reverse-time Migration Using One-way Wavefield Imaging Condition," *2007 SEG Annual Meeting*, Jan. 2007. [Online]. Available: https://www.onepetro.org/conference-paper/SEG-2007-2170

[27] C. Youzwishen and G. Margrave, "Finite difference modeling of acoustic waves in Matlab," *the 11th Annual Research Report of the ...*, vol. 11, 1999. [Online]. Available: https://crewes.org/ForOurSponsors/ResearchReports/1999/1999-06.pdf

[28] S. H. Gray, J. Etgen, J. Dellinger, and D. Whitmore, "Y2K Review Article Seismic migration problems and solutions," *Geophysics*, vol. 66, no. 5, pp. 1622–1640, 2001.

[29] R. Mittet, "A simple design procedure for depth extrapolation operators that compensate for absorption and dispersion," *Geophysics*, vol. 72, no. 2, 2007. [Online]. Available: http://library.seg.org/doi/abs/10.1190/1.2431637

[30] R. A. Bale, S. H. Gray, and M. G. K. Grech, "TTI wave equation migration by phase-shift plus interpolation," *CSPG CSEG Convention*, pp. 1–5, 2007.

[31] J. Pan and D. Negut, "A phase shift plus interpolation algorithm for prestack time migration," *SEG Technical Program Expanded Abstracts 2008*, pp. 2407–2411, Jan. 2008. [Online]. Available: http://library.seg.org/doi/abs/10.1190/1.3059362

[32] O. Yilmaz, “8. Earth Imaging in Depth,” *library.seg.org*. [Online]. Available: http://library.seg.org/doi/full/10.1190/1.9781560801580.ch8

[33] J.-B. Chen and S.-Y. Du, “Kinematic characteristics and the influence of reference velocities of phase-shift-plus-interpolation and extended-split-step-Fourier migration methods,” *Geophysical Prospecting*, vol. 58, no. 3, pp. 429–439, May 2010. [Online]. Available: http://doi.wiley.com/10.1111/j.1365-2478.2009.00845.x

[34] H. Geiger and G. Margrave, “Automatic selection of reference velocities for recursive depth migration by peak search method,” *2005 SEG Annual Meeting*, vol. 1, pp. 4–7, 2005. [Online]. Available: http://library.seg.org/doi/pdf/10.1190/1.2148115

[35] Mousa, “The design of stable, sparse wavefield extrapolators using projections onto convex sets,” *Geophysics*, vol. 78, no. 1, 2012. [Online]. Available: http://library.seg.org/doi/abs/10.1190/geo2012-0130.1

[36] L. Dan, Y. Xiao, P. Cheng, G. Wu, and S. Li, “A low-complexity multiple signal representation scheme in downlink OFDM-CDMA,” *Science in China Series F: Information Sciences*, vol. 52, no. 12, pp. 2433–2444, Dec. 2009. [Online]. Available: http://link.springer.com/10.1007/s11432-009-0211-9

[37] B. Qiao and J. Bancroft, “Choosing reference velocities for PSPI migration,” *crewes.org*, vol. 21, no. 3, pp. 1–8, 2009. [Online]. Available: https://www.crewes.org/ForOurSponsors/ResearchReports/2009/CRR200962.pdf

[38] R. J. Ferguson and G. F. Margrave, “Depth imaging in anisotropic media by symmetric non-stationary phase shift,” *Geophysical Prospecting*, no. 1984, pp. 281–288, 2002.

[39] W. Mousa, “Seismic Migration: A Digital Filtering Process Reducing Oil Exploration Risks,” *Signal Processing Magazine, IEEE*, no. May, pp. 117–123, 2012. [Online]. Available: http://ieeexplore.ieee.org/xpls/abs_all.jsp?arnumber=6179826

[40] A. Flor and E. Ligia, “Condition effect on shot profile,” *CT&F - Ciencia, Tecnología y FuturoCT&F - Ciencia, Tecnología y Futuro*, vol. 5, pp. 5–17, 2012.

[41] H. Lim, S. Kim, and J. Douglas, “Numerical methods for viscous and nonviscous wave equations,” *Applied Numerical Mathematics*, vol. 57, no. 2, pp. 194–212, Feb. 2007. [Online]. Available: http://linkinghub.elsevier.com/retrieve/pii/S0168927406000262

[42] S. Operto, J. Virieux, P. Amestoy, J.-Y. LExcellent, L. Giraud, and H. B. H. Ali, “3D finite-difference frequency-domain modeling of visco-acoustic wave propagation using a massively parallel direct solver: A feasibility study,” *Geophysics*, vol. 72, no. 5, pp. SM195–SM211, Sep. 2007. [Online]. Available: http://library.seg.org/doi/abs/10.1190/1.2759835

[43] A. a. Valenciano and B. Biondi, “2D deconvolution imaging condition for shotprofile migration,” *SEG Technical Program Expanded*

Abstracts 2003, pp. 1059–1062, Jan. 2003. [Online]. Available: http://library.seg.org/doi/abs/10.1190/1.1817454

[44] J. F. Claerbout, "TOWARD A UNIFIED THEORY OF REFLECTOR MAPPING," *GEOPHYSICS*, vol. 36, no. 3, pp. 467–481, Jun. 1971. [Online]. Available: http://library.seg.org/doi/abs/10.1190/1.1440185

[45] H. Zhou, H. Lin, S.-B. Sheng, H.-M. Chen, and Y. Wang, "High angle prestack depth migration with absorption compensation," *Applied Geophysics*, vol. 9, no. 3, pp. 293–300, Oct. 2012. [Online]. Available: http://link.springer.com/10.1007/s11770-012-0339-z

[46] J. Cui, W. Xie, R. Stewart, and G. Margrave, "Migration with compensation in a viscoacoustic medium," *CSEG National Convention*, vol. 2, no. 1, pp. 1–4, 2004.

[47] J. Carcione, D. Kosloff, and R. Kosloff, "Viscoacoustic wave propagation simulation in the earth," *Geophysics*, vol. 53, no. 1988, pp. 769–777, 1988. [Online]. Available: http://library.seg.org/doi/abs/10.1190/1.1442512

[48] J. Cui and J. He, "2D seismic migration with compensation: a preliminary study," *Journal of Geophysics and Engineering*, vol. 1, no. 4, pp. 263–267, Dec. 2004. [Online]. Available: http://stacks.iop.org/1742-2140/1/i=4/a=004?key=crossref.d56aacd757b2e8aa2b7165d262354f27

[49] J. Thorbecke, “2D Finite-Difference Wavefield Modelling,” *Book*, pp. 1–47, 2013. [Online]. Available: http://janth.home.xs4all.nl/Software/fdelmodcManual.pdf

[50] E. Bonomi, L. Brieger, C. Nardone, E. Pieroni, G. Area, and M. Apr, “Phase shift plus interpolation: A scheme for high performance echo-reconstruction imaging exploding refector model,” *CRS4 Appeared in Computers in physics*, vol. 12, no. 2, 1998.

[51] H. Kühl, M. Sacchi, and J. Fertig, “The Hartley transform in seismic imaging,” *Geophysics*, vol. 66, no. 4, pp. 1251–1257, 2001. [Online]. Available: http://library.seg.org/doi/abs/10.1190/1.1487072

[52] A. Mittal, A. Moorthy, and A. Bovik, “No-reference image quality assessment in the spatial domain,” *Image Processing, IEEE*, vol. 21, no. 12, pp. 4695–4708, 2012. [Online]. Available: http://ieeexplore.ieee.org/xpls/abs_all.jsp?arnumber=6272356

[53] Z. Wang, H. Sheikh, and A. Bovik, “No-reference perceptual quality assessment of JPEG compressed images,” *Image Processing. 2002.*, pp. 477–480, 2002. [Online]. Available: http://ieeexplore.ieee.org/xpls/abs_all.jsp?arnumber=1038064

[54] D. Hale, “Stable explicit depth extrapolation of seismic wavefields,” *Geophysics*, vol. 56, no. I, pp. 1770–1777, 1991. [Online]. Available: http://library.seg.org/doi/abs/10.1190/1.1442989

[55] M. M. Naseer and W. A. Mousa, “Linear complementarity problem : A novel approach to design finite-impulse response wavefield extrapolation filters,” *Geophysics*, vol. 80, no. 2, pp. 1–9, 2015.

[56] C. Chang and C. Lin, “LIBSVM: a library for support vector machines,” *ACM Transactions on Intelligent Systems*, pp. 1–39, 2011. [Online]. Available: http://dl.acm.org/citation.cfm?id=1961199

[57] A. Moorthy and A. Bovik, “A two-step framework for constructing blind image quality indices,” *Signal Processing Letters, IEEE*, vol. 17, no. 5, pp. 513–516, 2010. [Online]. Available: http://ieeexplore.ieee.org/xpls/abs_all.jsp?arnumber=5432998

[58] D. Basak, S. Pal, and D. Patranabis, “Support vector regression,” *Neural Information Processing*, 2007.

[59] B. Schölkopf, A. Smola, R. Williamson, and P. Bartlett, “New support vector algorithms,” *Neural computation*, vol. 1245, pp. 1207–1245, 2000. [Online]. Available: http://www.mitpressjournals.org/doi/abs/10.1162/089976600300015565

Vitae

- Name: Mohammed Yahiya Naveed
- Nationality: Indian
- Date of Birth: 08-Apr-1990
- Email: *yahiyanaveed5@gmail.com*
- Permenant Address: 1-4-304/5/1, Bholakpur, Musheerabad, Hyderabad, Telangana, India
- Bachelor's Degree: Osmania University, Hyderabad, India.
- Work Experience: Worked as a System Engineer at Infosys Limited, India from July 2011 to Sept 2012.